

OCEAN

ENGINEERING

GROUP

Prediction of Performance of Podded Propulsors  
via Coupling of a Vortex–Lattice Method  
with an Euler or a RANS Solver

Bikash Mishra

August 2005

Report No. 05–1

**ENVIRONMENTAL AND WATER RESOURCES ENGINEERING**  
**DEPARTMENT OF CIVIL, ARCHITECTURAL**  
**and ENVIRONMENTAL ENGINEERING**  
**THE UNIVERSITY OF TEXAS AT AUSTIN**  
Austin, TX 78712

Copyright  
by  
Bikash Mishra  
2005

**Prediction of Performance of Podded Propulsors via Coupling of  
a Vortex-Lattice Method with an Euler or a RANS solver**

**by**

**Bikash Mishra, B.Tech.**

**Thesis**

Presented to the Faculty of the Graduate School  
of The University of Texas at Austin  
in Partial Fulfillment  
of the Requirements  
for the Degree of

**Master of Science in Engineering**

The University of Texas at Austin

August 2005

**Prediction of Performance of Podded Propulsors via Coupling of  
a Vortex-Lattice Method with an Euler or a RANS solver**

APPROVED BY  
SUPERVISING COMMITTEE:

Supervisor: \_\_\_\_\_  
**Spyros A. Kinnas**

Reader: \_\_\_\_\_  
**Loukas Kallivokas**

To my parents, brother and friends

## Acknowledgements

I would like to take this opportunity to thank several people whose support, guidance and encouragement egged me on during my research work and helped me complete my Masters thesis.

First and foremost, I would like to thank my supervisor, Dr. Spyros A. Kinnas with greatest appreciation and gratefulness. His guidance and insights were of immense help during the course of my studies and research.

I would also like to thank Dr. Loukas F. Kallivokas for taking his time out of his busy schedule and reading this thesis, and providing me with invaluable comments, assistance and encouragement.

I would like to thank my parents, my brother Bivas and my friends, especially Piyush, Sanketh and Aswin who stood by me throughout this process and picked me up with their encouraging words every time I faltered.

I would like to thank the members of the Computational Hydrodynamics Laboratory, Dr. Hanseong Lee, Mr. Hua Gu, Mr. Bharani Kacham, Mr. Apurva Gupta, Mr. Yi-Hsiang Yu, Ms. Hong Sun, Mr. Vimal Vinayan, Mr. Yumin Deng, Mr. Fahad Mohammad and Mr. Lei He for their unending support and suggestions. I would also like to thank Dr. Rhee of FLUENT Inc. for the invaluable suggestions he provided regarding FLUENT.

Support for this research was provided by Phase III, and IV of the “Con-

sortium on Cavitation Performance of High Speed Propulsors” with the following members: AB Volvo Penta, American Bureau of Shipping, Daewoo Shipbuilding and Marine Engineering Co. Ltd., El Pardo Model Basin, Hyundai Maritime Research Institute, Kawasaki Heavy Industries, Naval Surface Warfare Center Carderock Division through the Office of Naval Research (Contracts N00014-01-1-0225 and N00014-04-1-0287), Rolls-Royce marine AB, Rolls-Royce Marine AS, VA Tech Escher Wyss GMBH, Wärtsilä Propulsion Netherlands B.V., and Wärtsilä Propulsion Norway AS. Partial support of this work was also provided by the Office of Naval Research under the National Naval Responsibility for Naval Engineering (NNR-NE) program, through Florida Atlantic University (Subagreement TRD67).

Finally I would like to thank the faculty of the College of Engineering at the University of Texas at Austin for the excellent education they provided.

**Prediction of Performance of Podded Propulsors via Coupling of a  
Vortex-Lattice Method with an Euler or a RANS solver**

by

Bikash Mishra, M.S.E.

The University of Texas at Austin, 2005

**SUPERVISOR: Spyros A. Kinnas**

Podded propulsor units are one of the latest innovations in the field of propulsion, and are used in many commercial or naval vessels. The major advantage of these units over conventional propeller based systems is their ability to provide thrust in all directions, giving high maneuverability and good seakeeping characteristics.

In this work podded propulsors are modeled using axi-symmetric (assuming an axisymmetric pod and ignoring the presence of strut) or 3-D solvers. At first, a Vortex Lattice Method (MPUF-3A) is coupled with an Euler solver (GBFLOW-3X/3D). MPUF-3A is used to solve for the potential flow around each propeller, obtain the pressure distribution on the blades and predict the thrust and torque for each propeller. The pressure distributions are then converted into body forces which represent the propeller in GBFLOW. GBFLOW solves for the flow around the pod

(and strut) and the effective wake to each propeller is calculated. Iterations are carried out between the two methods till convergence is obtained, and the complete interaction among each one of the propellers (in the case of a twin propeller system) and the pod (and strut) is captured.

The same procedure is then applied by coupling the commercial code FLUENT with MPUF-3A. This coupling is used to predict the effects of viscosity on the flow field and on the overall podded propeller performance.

The objective of this research is to predict the forces on the podded unit in inviscid and viscous flow field and to compare the results from the two approaches with each other and with measurements from experiments.

# Table of Contents

<b>Acknowledgements</b>	<b>v</b>
<b>Abstract</b>	<b>vii</b>
<b>List of Tables</b>	<b>iv</b>
<b>List of Figures</b>	<b>vi</b>
<b>Nomenclature</b>	<b>xiii</b>
<b>Chapter 1. Introduction</b>	<b>1</b>
1.1 Background . . . . .	1
1.2 Motivation . . . . .	5
1.3 Objectives . . . . .	7
1.4 Overview . . . . .	8
<b>Chapter 2. Literature Review</b>	<b>10</b>
2.1 Vortex Lattice Method . . . . .	10
2.2 Effective Wake Prediction . . . . .	11
2.2.1 Multi-Component Propulsors . . . . .	12
2.2.2 Podded Propulsors . . . . .	14
<b>Chapter 3. Formulation and Numerical Implementation</b>	<b>17</b>
3.1 Continuity and Euler Equations . . . . .	17
3.2 Steady Euler Solver . . . . .	18
3.2.1 Axisymmetric Steady Euler Solver . . . . .	19
3.2.2 Three-dimensional Steady Euler-Solver . . . . .	20
3.2.3 Boundary Conditions . . . . .	22
3.3 Vortex Lattice Method . . . . .	29
3.4 Boundary Element Method . . . . .	30

3.4.1	Formulation of Potential Flow around a Pod and Strut . . . . .	31
3.4.2	Kinematic Boundary Condition on the Body . . . . .	32
3.4.3	Kutta Condition . . . . .	32
3.4.4	Hull Effects . . . . .	33
3.5	FLUENT . . . . .	33
3.6	Coupling to determine pod and propeller interaction . . . . .	35
3.6.1	GBFLOW or FLUENT/MPUF-3A coupling . . . . .	35
3.6.2	Coupling of Non-dimensional Forces from FVM and VLM . . . . .	37
3.6.3	BEM/MPUF3A coupling . . . . .	39
<b>Chapter 4. Validation and Comparisons with Other Methods - Axisymmetric Pod</b>		<b>42</b>
4.1	Axisymmetric Euler Solver . . . . .	42
4.1.1	Grid and Boundary Conditions . . . . .	43
4.1.2	Results . . . . .	45
4.2	FLUENT . . . . .	47
4.2.1	Grid and Boundary Conditions . . . . .	48
4.2.2	Results . . . . .	52
4.2.3	Viscous effects . . . . .	54
4.2.4	Study of different models . . . . .	63
4.3	BEM . . . . .	65
4.3.1	Results . . . . .	66
4.4	Comparisons among different methods . . . . .	69
<b>Chapter 5. Axisymmetric Pod and Propeller Interaction</b>		<b>72</b>
5.1	Experiment . . . . .	72
5.1.1	Experimental Setup . . . . .	73
5.2	Propeller Configurations . . . . .	74
5.3	Pull Type . . . . .	75
5.3.1	Coupling with GBFLOW-3X . . . . .	75
5.3.2	Coupling with FLUENT . . . . .	81
5.4	Push Type . . . . .	97
5.4.1	Coupling with GBFLOW-3X . . . . .	97
5.4.2	Coupling with FLUENT . . . . .	101

5.5	Twin type . . . . .	113
5.5.1	Coupling of GBFLOW-3X . . . . .	113
5.5.2	Coupling with FLUENT . . . . .	117
<b>Chapter 6.</b>	<b>Pod with strut</b>	<b>126</b>
6.1	3-D Euler Solver (GBFLOW-3D) . . . . .	126
6.1.1	Grid Generation . . . . .	127
6.1.2	Boundary Conditions . . . . .	129
6.1.3	Results . . . . .	129
6.2	FLUENT-3D . . . . .	133
6.2.1	Grid and boundary conditions . . . . .	135
6.2.2	Inviscid Results . . . . .	138
6.2.3	Viscous Results . . . . .	138
6.3	Comparison among different methods . . . . .	142
<b>Chapter 7.</b>	<b>Conclusions and Recommendations</b>	<b>147</b>
7.1	Conclusions . . . . .	147
7.2	Recommendations . . . . .	148
<b>Appendix A</b>		<b>149</b>
<b>Bibliography</b>		<b>159</b>
<b>Vita</b>		<b>169</b>

## List of Tables

4.1	Total force on the pod from Euler solver for axisymmetric runs for different grid densities. Forces made non-dimensional as given by equation 3.5 . . . . .	46
4.2	Run parameters for the 2-D axisymmetric inviscid version of FLUENT	51
4.3	Total force on the pod and the computed surface area from FLUENT for axisymmetric runs for different grid densities. . . . .	56
4.4	Run parameters for 2-D axisymmetric viscous FLUENT . . . . .	56
4.5	Reynolds number, $k$ and $\epsilon$ for which runs are carried out using viscous FLUENT . . . . .	61
4.6	Comparison of mean empirical frictional force coefficient $C_f$ with that from $k - \epsilon$ model . . . . .	63
4.7	Total force on the pod from BEM for axisymmetric runs for different paneling. . . . .	68
5.1	Break-up of forces from MPUF-3A and GBFLOW-3X for pulling propeller for various advance ratios . . . . .	81
5.2	Break-up of forces from MPUF-3A and FLUENT for pulling propeller for various advance ratios . . . . .	85
5.3	Break-up of forces from MPUF-3A and viscous FLUENT for pulling propeller for various advance ratios . . . . .	90
5.4	Break-up of forces from MPUF-3A and GBFLOW-3X for pushing propeller for various advance ratios . . . . .	100
5.5	Break-up of forces from MPUF-3A and inviscid FLUENT for pushing propeller for various advance ratios . . . . .	103
5.6	Break-up of forces from MPUF-3A and viscous FLUENT for pushing propeller for various advance ratios . . . . .	109
5.7	Break-up of forces from MPUF-3A and GBFLOW-3X for twin propeller unit for various advance ratios . . . . .	115
5.8	Break-up of forces from MPUF-3A and FLUENT (RSM) for twin propeller unit for various advance ratios . . . . .	119
6.1	Run parameters for 3-D viscous FLUENT . . . . .	139

1	The pod geometry used by [Szantyr 2001a] . . . . .	151
2	The parabolic section strut used for GBFLOW-3D runs with leading edge at the location $X=-0.6$ on the pod, and trailing edge at $X=+0.6$ .	152
3	The strut used by [Szantyr 2001a] for the experimental measurements. It is a NACA066 section, and has the leading edge at the location $X=-0.6$ on the pod, and trailing edge at $X=+0.6$ . . . . .	153
4	Front propeller geometry. The front propeller placed at the location -1.1899 on the pod . . . . .	154
5	The specific stations along the chord where the propeller blade thickness and camber distributions are specified, at the given radii locations.	155
6	The camber distribution specified at the nine radii locations specified in the geometry file and at specific stations along the chord. . . . .	156
7	The thickness distribution specified at the nine radii locations specified in the geometry file and at specific stations along the chord. . .	157
8	Geometry of the aft propeller. The aft propeller placed at the location 1.1899 on the pod. The thickness and camber distributions are the same as for the fore propeller. . . . .	158

## List of Figures

1.1	Figure showing a pull type podded unit. . . . .	2
1.2	Figure showing a push type podded unit. . . . .	3
1.3	Figure showing a twin type podded unit. . . . .	4
3.1	Ship-fixed Cartesian coordinate system (taken from [Choi 2000]) . .	19
3.2	2-D grid showing the boundary conditions used for the axisymmetric Euler solver . . . . .	22
3.3	Boundary conditions for the Euler solver which evaluates the flow around the pod and strut in the presence of the propeller, (taken from [Gupta 2004]). . . . .	25
3.4	Boundary conditions on the domain at an axial location showing pod and strut (no repeat boundary), (taken from [Gupta 2004]) . . . . .	26
3.5	Boundary conditions on the domain at an axial location showing the repeat boundary ( $k = 1, N_k$ ), (taken from [Gupta 2004]) . . . . .	27
3.6	Pictorial representation of the coupling of the Finite Volume Method and the Vortex Lattice Method (from [Kinnas, Gu, Gupta and Lee 2004]). . . . .	36
3.7	Pictorial representation of the coupling of the Boundary Element Method and the Vortex Lattice Method. . . . .	41
4.1	2-D grid showing the boundaries for the axisymmetric Euler solver .	44
4.2	Closeup of the leading and trailing edge showing the uniform expansion ratio. . . . .	44
4.3	Close-up of different grids (near the leading edge) used for convergence studies in GBFLOW-3X without propeller . . . . .	46
4.4	Convergence of axial velocities on body with different grids in GBFLOW-3X (number of nodes in axial direction is varied) . . . . .	47
4.5	Convergence of pressure on body with different grids in GBFLOW-3X (number of nodes in axial direction is varied) . . . . .	48
4.6	Axial velocity contour around the body from GBFLOW-3X . . . . .	49
4.7	Pressure contour around the body from GBFLOW-3X . . . . .	50
4.8	Unstructured grid used in inviscid FLUENT showing the inflow and outflow boundaries. . . . .	51

4.9	Unstructured grid used in viscous FLUENT showing the inflow and outflow boundaries. . . . .	52
4.10	A closeup view of the grid near the pod, showing the boundary layer used and the triangular grid at the leading edge of the pod. . . . .	53
4.11	Structured grid used in FLUENT and exported from GBFLOW-3X .	53
4.12	Convergence of axial velocities on body with different unstructured grids using FLUENT (inviscid) . . . . .	54
4.13	Convergence of pressure on body with different unstructured grids using FLUENT (inviscid) . . . . .	55
4.14	Axial velocity contour and streamlines from inviscid FLUENT . . .	57
4.15	Pressure contour from inviscid FLUENT . . . . .	58
4.16	Axial velocities on body with unstructured and structured grids (FLUENT inviscid) as shown in Figures 4.8 and 4.11 . . . . .	59
4.17	Pressure on body with unstructured and structured grids (FLUENT inviscid) as shown in Figures 4.8 and 4.11 . . . . .	59
4.18	Axial velocities near leading edge with unstructured and structured grids at location shown in Figure 4.19 . . . . .	60
4.19	Locations where inviscid FLUENT and GBFLOW-3X axial velocities are compared . . . . .	60
4.20	Comparison of axial velocities for inviscid FLUENT and GBFLOW-3X at given location . . . . .	61
4.21	Comparison of pressure for inviscid FLUENT and GBFLOW-3X at given location . . . . .	62
4.22	$Y^+$ on the pod for viscous FLUENT run, $Re=4.5 \times 10^5$ . . . . .	62
4.23	Locations for comparison of inviscid and viscous axial velocities . .	64
4.24	Axial velocities for different $Re$ at $X_f=-0.415$ location as shown in Figure 4.23. . . . .	64
4.25	Axial velocities from different methods at $X_a=1.93$ location as shown in Figure 4.23, $Re = 6.26 \times 10^5$ . . . . .	65
4.26	Grid used for the axisymmetric BEM solver . . . . .	66
4.27	Convergence of axial velocities with different grids using BEM . . .	67
4.28	Convergence of pressure with different grids using BEM . . . . .	67
4.29	Convergence of forces with number of cells from all methods . . . .	68
4.30	Non-dimensional axial velocity on the pod from axisymmetric inviscid FLUENT and BEM compared with GBFLOW-3X. . . . .	70
4.31	Non dimensional pressure on the pod from axisymmetric inviscid FLUENT and BEM compared with GBFLOW-3X. . . . .	71

5.1	Axial body force contours in GBFLOW-3X domain obtained by integration of pressures on the propeller, for a pull type podded propulsor, $J_s = 0.5$ .	76
5.2	Close-up of axial body force contours in GBFLOW-3X for a pull type podded propulsor, $J_s = 0.5$ .	76
5.3	Axial velocity contour in GBFLOW-3X for pull type podded propulsor, $J_s = 0.5$ .	77
5.4	Pressure contour in GBFLOW-3X for pull type podded propulsor, $J_s = 0.5$ .	77
5.5	Convergence of circulation distribution with iterations for GBFLOW-3X coupled with MPUF-3A, for pull type podded propulsor, $J_s = 0.5$ .	78
5.6	Pictorial representation of the direction of forces from MPUF-3A and GBFLOW/FLUENT, for $0^\circ$ yaw angle.	79
5.7	Comparison of axial force for a pulling propeller from the present method compared with the measurements of [Szantyr 2001a].	80
5.8	Axial body force distribution in FLUENT for an unstructured grid, $J_s = 0.5$ .	82
5.9	Axial body force distribution in FLUENT for a structured grid, $J_s = 0.5$ .	82
5.10	Convergence of axial body force distribution in FLUENT for varying grid sizes, $J_s = 0.5$ .	83
5.11	Axial body force distribution in FLUENT over a very fine structured grid, $J_s = 0.5$ .	84
5.12	Axial velocity contour from inviscid FLUENT for pull type podded propulsor, $J_s = 0.5$ .	85
5.13	Pressure contour from inviscid FLUENT for pull type podded propulsor, $J_s = 0.5$ .	86
5.14	Comparison of converged circulation distributions predicted from GBFLOW-3X and FLUENT(inviscid) coupled with MPUF-3A, for pull type podded propulsor, $J_s = 0.5$ .	87
5.15	Comparison of axial force for a pulling propeller from FLUENT(inviscid) and GBFLOW-3X coupled with MPUF-3A.	88
5.16	Axial velocity contour in viscous FLUENT for pull type podded propulsor, $J_s = 0.5$ , $Re = 6.26 \times 10^5$ .	89
5.17	Pressure contour in viscous FLUENT for pull type podded propulsor, $J_s = 0.5$ , $Re = 6.26 \times 10^5$ .	90
5.18	Total axial velocity at effective wake location for viscous and inviscid FLUENT coupled with MPUF-3A, for pull type podded propulsor, $J_s = 0.5$ , $Re = 6.26 \times 10^5$ .	91

5.19	Converged circulation distributions predicted from FLUENT (viscous) and FLUENT(inviscid) coupled with MPUF-3A, for pull type podded propulsor, $J_s = 0.5, Re = 6.26 \times 10^5$ . . . . .	92
5.20	Converged pressure distributions predicted from GBFLOW-3X, FLUENT (viscous) and FLUENT(inviscid) coupled with MPUF-3A, for pull type podded propulsor, $J_s = 0.5, Re = 6.26 \times 10^5$ . . . . .	93
5.21	Comparison of axial force for a pulling propeller from FLUENT(inviscid & viscous) and GBFLOW coupled with MPUF-3A. . . . .	94
5.22	Comparison of axial velocity at aft effective wake location from inviscid, $k - \epsilon$ and RSM models, $J_s = 0.5, Re = 6.26 \times 10^5$ . . . . .	95
5.23	Comparison of swirl velocity at aft effective wake location from inviscid, $k - \epsilon$ and RSM models, $J_s = 0.5, Re = 6.26 \times 10^5$ . . . . .	96
5.24	Body force contours in GBFLOW-3X domain obtained by integration of pressures on the propeller, for a push type podded propulsor, $J_s = 0.5$ . . . . .	97
5.25	Axial velocity contour in GBFLOW-3X for push type podded propulsor, $J_s = 0.5$ . . . . .	98
5.26	Pressure contour in GBFLOW-3X for push type podded propulsor, $J_s = 0.5$ . . . . .	99
5.27	Convergence of circulation distribution with iterations for GBFLOW-3X for push type podded propulsor, $J_s = 0.5$ . . . . .	99
5.28	Body force distribution in FLUENT on the grid for inviscid case, $J_s = 0.5$ . . . . .	101
5.29	Body force distribution in FLUENT on the grid for viscous case, $J_s = 0.5, Re = 6.26 \times 10^5$ . . . . .	102
5.30	Axial velocity contour in inviscid FLUENT for push type podded propulsor, $J_s = 0.5$ . . . . .	103
5.31	Comparison of effective axial velocity between GBFLOW-3X and FLUENT (inviscid) coupled with MPUF-3A, for a push type unit, $J_s = 0.5$ . . . . .	104
5.32	Converged circulation distributions predicted from GBFLOW-3X and FLUENT(inviscid) coupled with MPUF-3A, for push type podded propulsor, $J_s = 0.5$ . . . . .	105
5.33	Axial force for a pushing propeller predicted from FLUENT (inviscid) and GBFLOW-3X coupled with MPUF-3A. . . . .	106
5.34	Axial velocity contours predicted by viscous FLUENT for push type podded propulsor, $J_s = 0.5, Re = 6.26 \times 10^5$ . . . . .	107
5.35	Comparison of total axial velocity at effective wake plane location from inviscid and viscous FLUENT coupled with MPUF-3A, $J_s = 0.5, Re = 6.26 \times 10^5$ . . . . .	108

5.36	Comparison of effective velocity at effective wake plane location from inviscid and viscous FLUENT coupled with MPUF-3A, $J_s = 0.5$ , $Re = 6.26 \times 10^5$ . . . . .	109
5.37	Comparison of converged circulation from inviscid and viscous FLUENT coupled with MPUF-3A, $J_s = 0.5$ , $Re = 6.26 \times 10^5$ . . . . .	110
5.38	Comparison of pressure distributions along the body for a pushing propeller from FLUENT(inviscid & viscous) and GBFLOW-3X coupled with MPUF-3A. . . . .	111
5.39	Comparison of axial force for a pushing propeller from FLUENT(inviscid & viscous) and GBFLOW-3X coupled with MPUF-3A. . . . .	112
5.40	Axial velocity contour in GBFLOW-3X for twin type podded propulsor, $J_s = 0.5$ . . . . .	114
5.41	Pressure contour in GBFLOW-3X for twin type podded propulsor, $J_s = 0.5$ . . . . .	114
5.42	Convergence of circulation distribution with iterations for fore propeller from GBFLOW-3X for twin type podded propulsor, $J_s = 0.5$ . . . . .	115
5.43	Convergence of circulation distribution with iterations for aft propeller from GBFLOW-3X for twin type podded propulsor, $J_s = 0.5$ . . . . .	116
5.44	Comparison of axial force for a twin type propeller unit from present method compared with experiments of [Szantyr 2001a]. . . . .	116
5.45	Axial velocity contour from viscous FLUENT for twin type podded propulsor, $J_s = 0.5$ , $Re = 6.26 \times 10^5$ . . . . .	117
5.46	Pressure contour from viscous FLUENT for twin type podded propulsor, $J_s = 0.5$ , $Re = 6.26 \times 10^5$ . . . . .	118
5.47	Comparison of effective velocity for fore propeller between GBFLOW-3X and FLUENT (viscous) coupled with MPUF-3A, for a twin type unit, $J_s = 0.5$ , $Re = 6.26 \times 10^5$ . . . . .	119
5.48	Comparison of effective axial velocity for aft propeller predicted from GBFLOW-3X and FLUENT (viscous) coupled with MPUF-3A, for a twin type unit, $J_s = 0.5$ , $Re = 6.26 \times 10^5$ . . . . .	120
5.49	Comparison of effective swirl velocity for aft propeller predicted from GBFLOW-3X and FLUENT (viscous) coupled with MPUF-3A, for a twin type unit, $J_s = 0.5$ , $Re = 6.26 \times 10^5$ . . . . .	121
5.50	Comparison of circulation distributions for fore propeller predicted from GBFLOW-3X and FLUENT (viscous) coupled with MPUF-3A, for a twin type unit, $J_s = 0.5$ , $Re = 6.26 \times 10^5$ . . . . .	122
5.51	Comparison of circulation distributions for aft propeller predicted from GBFLOW-3X and FLUENT (viscous) coupled with MPUF-3A, for a twin type unit, $J_s = 0.5$ , $Re = 6.26 \times 10^5$ . . . . .	123

5.52	Comparison of pressure distributions along the body for a twin propeller from FLUENT(viscous) and GBFLOW-3X coupled with MPUF-3A. . . . .	124
5.53	Comparison of axial force for a twin type propeller unit from GBFLOW-3X and viscous FLUENT coupled with MPUF-3A. . . . .	125
6.1	Cross-sectional view of the domain in axial direction showing the type of grid cells distribution at different locations (taken from [Gupta 2004]). . . . .	127
6.2	Cross-sectional view of the domain showing the grid cells near the strut and the pod. Circumferential cells are uniformly distributed. . .	128
6.3	Cross-sectional view of the domain showing the grid cells near the strut and the pod. Circumferential cells are clustered near the strut. .	129
6.4	Location on strut where velocity and pressure comparisons are carried out. . . . .	130
6.5	Convergence of axial velocity with varying number of nodes in axial direction in GBFLOW-3D. . . . .	131
6.6	Convergence of pressure with varying number of nodes in axial direction in GBFLOW-3D. . . . .	131
6.7	Comparison of axial velocity between the two different types of grids used in $k$ direction in GBFLOW-3D, $k = 121$ . . . . .	132
6.8	Comparison of pressure between the two different types of grids used in $k$ direction in GBFLOW-3D, $k = 121$ . . . . .	132
6.9	Different grids for which convergence with varying number of nodes along the circumferential direction in GBFLOW-3D . . . . .	133
6.10	Convergence of axial velocity with varying number of nodes along the circumferential direction in GBFLOW-3D . . . . .	134
6.11	Convergence of pressure with varying number of nodes along the circumferential direction in GBFLOW-3D . . . . .	134
6.12	The domain used in 3D FLUENT, showing the projection in $x$ - $y$ plane.	136
6.13	The domain used in 3D FLUENT, showing the projection in $y$ - $z$ plane.	136
6.14	Close up of the grid used in 3D FLUENT near the pod and strut in the $x$ - $y$ plane. . . . .	137
6.15	Close up of the grid used in 3D FLUENT near the pod and strut in the $y$ - $z$ plane. . . . .	137
6.16	Convergence of axial velocity with varying number of nodes on the pod using FLUENT-3D (inviscid). . . . .	138
6.17	Convergence of pressure with varying number of nodes on the pod using FLUENT-3D (inviscid). . . . .	139

6.18	$y^+$ distribution over the 3D pod and strut. . . . .	140
6.19	Locations behind the strut where the velocity and pressure comparisons are carried out for viscous 3D FLUENT. . . . .	141
6.20	Convergence of axial velocity with varying number of nodes on the pod using FLUENT-3D (viscous), $Re = 4.52 \times 10^6$ . . . . .	141
6.21	Convergence of pressure with varying number of nodes on the pod using FLUENT-3D (viscous), $Re = 4.52 \times 10^6$ . . . . .	142
6.22	Comparison of axial velocity on the pod among the different methods.	143
6.23	Comparison of pressure on the pod among the different methods. . .	143
6.24	Comparison of axial velocity among inviscid and viscous 3D FLUENT at the line on the $x$ - $z$ plane, $Re = 4.52 \times 10^6$ . . . . .	144
6.25	Comparison of pressure among inviscid and viscous 3D FLUENT at the line on the $x$ - $z$ plane, $Re = 4.52 \times 10^6$ . . . . .	145
6.26	Comparison of axial velocity among inviscid and viscous 3D FLUENT at the line on the $x$ - $y$ plane, $Re = 4.52 \times 10^6$ . . . . .	145
6.27	Comparison of pressure among inviscid and viscous 3D FLUENT at the line on the $x$ - $y$ plane, $Re = 4.52 \times 10^6$ . . . . .	146

# Nomenclature

## Latin Symbols

$A_{ij}$	dipole influence coefficients
$A_x, A_y, A_z$	projections of the area of each face in x,y,z directions
$AR$	Aspect Ratio
$B_{ij}$	source influence coefficients
$c$	speed of sound
$C_f$	friction coefficient
$C_p$	pressure coefficient, $C_p = (P - P_o)/(0.5\rho n^2 D^2)$ for propeller $C_p = (P - P_o)/(0.5\rho V_s^2)$ otherwise
$C_Q$	torque coefficient based on $V_s$ , $C_Q = \frac{Q}{0.5\rho V_s^2 \pi R^3}$
$C_T$	thrust coefficient based on $V_s$ , $C_T = \frac{T}{0.5\rho V_s^2 \pi R^2}$
$D$	propeller diameter, $D = 2R$
$F_n$	Froude number based on $n$ , $F_n = n^2 D/g$
$\vec{f}$	body force per unit mass, $f = (f_x, f_y, f_z)$ ,
<b>F</b>	column matrix for the $x$ derivative terms
$F_1, F_2$	methods to compare force from the experiment with GBFLOW-3D
$F_{FR}$	dimensional frictional force on the surface of the body
$F_{FRND}$	non-dimensional frictional force on the surface of the body, $F_{FRND} = \frac{F_{FR}}{\rho U^2 R^2}$

$F$	Dimensional force from GBFLOW-3D
$F_{GB}$	non-dimensional force from GBFLOW-3D, $F_{GB} = \frac{F}{\rho U^2 R^2}$
$F_{NP}$	no propeller or tear force
$F_{prop}$	non-dimensional propeller force force, $F_{prop} = \frac{F}{\rho n^2 D^4}$
$F_{Total}$	total force from propeller and pod interaction
$F_x, F_y$	non-dimensionalized total $x$ and $y$ direction force
$G$	Green's function
<b>G</b>	column matrix for the $y$ or $r$ derivative terms
<b>H</b>	column matrix for the $z$ or $\theta$ derivative terms
$J_s$	advance ratio based on $V_s$ , $J_s = V_s/nD$
$K_Q$	torque coefficient, $K_Q = Q/\rho n^2 D^5$
$K_T$	thrust coefficient, $K_T = T/\rho n^2 D^4$
$K_x(SZ)$	axial force from the experiment
$K_y(SZ)$	transverse force from the experiment
$L$	reference length used in non-dimensionalization
$M$	artificial Mach number
$n$	propeller rotational frequency (rev/s), or
$\hat{n}$	normal direction vector
$N_k$	maximum number of cells in the circumferential direction
$P$	pressure, or pitch of the propeller
$P_{atm}$	atmospheric pressure
$P_c$	cavitating pressure
$P_o$	far upstream pressure, at the propeller axis

$P_v$	vapor pressure of water
$p, q$	field point and variable point
$\vec{q}$	total velocity
$\vec{q}_n$	local normal velocity
$\vec{q}_t$	local tangential velocity
$Q$	Propeller torque, or mass flow rate
<b>Q</b>	column matrix containing source terms
$Q_m$	residual of the continuity equation
$R$	propeller radius, or distance between the field and variable points
$R_{ij}$	residual term for each cell
$Re$	Reynolds number based on reference length $L$ , $Re = \frac{\rho U_\infty L}{\mu}$
$s, v, n$	non-orthogonal coordinates on local panel
$s, w, n$	orthogonal coordinates on local panel
$S_{ij}$	area of cell in two-dimensional formulation
$S_C$	area of one cell
$t$	non-dimensional time
$t^*$	pseudo time step
$T$	propeller thrust, or time period of motion
<b>U</b>	column matrix for time derivative terms

$U_\infty, U_{in}$	flow velocity at infinity
$u, v, w$	$x, y$ and $z$ -direction velocities
$U, U_x, u_r, u_\theta$	axial, radial and circumferencial velocities
$V$	Velocity in $y$ direction
$\vec{v}$	total velocity vector, $\vec{x} = (u, v, w)$ or $(u_x, u_r, u_\theta)$
$V_s$	ship speed
$\hat{V}_c$	computational cell volume
$\vec{x}$	location vector on the ship fixed, $\vec{x} = (x, y, z)$ or $(x, r, \theta)$ coordinate system
$(x, r, \theta)$	downstream, radial and circumferencial coordinates respectively
$(x, y, z)$	downstream, upward and port side coordinates respectively
$X_e$	axial location where effective velocity is determined
$X_p$	axial location of propeller plane

## Greek Symbols

$\beta$	artificial compressibility factor
$\gamma$	vorticity
$\Gamma$	propeller blade circulation
$\delta t, \Delta t$	time step size
$\Delta p$	pressure difference
$(\Delta x, \Delta y)$	cell size in $x$ and $y$ direction
$\theta$	yaw angle of attack
$\kappa$	turbulence kinetic energy
$\epsilon$	turbulence dissipation rate
$\mu$	dynamic viscosity of water
$\nu$	kinematic viscosity of water
$\phi$	perturbation potential
$\Phi$	total potential
$\psi$	angle between $\vec{s}$ and $\vec{v}$
$\rho$	fluid density
$\tilde{\rho}$	artificial fluid density
$\sigma$	cavitation number based on $U_\infty$ , $\sigma = (P_o - P_c)/(0.5\rho U_\infty^2)$
$\sigma_n$	cavitation number based on $n$ , $\sigma_n = (P_o - P_c)/(0.5\rho n^2 D^2)$
$\sigma_2, \sigma_4$	artificial dissipation constants
$\omega$	propeller angular velocity

## Subscripts

$1, 2, 3, 4, \dots$	node numbers
$A, B, C, D, \dots$	cell indices
$(i, j, k)$	node or cell indices in each direction; $i$ is axial, $j$ is radial, and $k$ is circumferential.
$N, W, S, E, T, B$	face (in three-dimension) or edge (in axisymmetric) indices at north, west, south, east, top, and bottom of a cell
$T, I, E$	total, propeller induced, and effective wake velocities (in some figures)

## Superscripts

*	intermediate velocity or pressure
$n, n + 1$	time step indices

## **Acronyms**

BEM	Boundary Element Method
CFD	Computational Fluid Dynamics
CPU	Central Processing Unit (time)
DBC	Dynamic Boundary Condition
FPSO	Floating, Production, Storage and Offloading (vessels)
FVM	Finite Volume Method
KBC	Kinematic Boundary Condition
MIT	Massachusetts Institute of Technology
NACA	National Advisory Committee for Aeronautics
RANS	Reynolds Averaged Navier-Stokes(equations)
RSM	Reynolds Stress Model
TE	Trailing Edge
VLM	Vortex Lattice Method

## **Computer Program Names**

DTNS3D	NSWC-CD's RANS code
GBFLOW-3X	axisymmetric steady Euler solver
GBFLOW-3D	three-dimensional steady Euler solver
MPUF-3A	cavitating propeller potential flow solver based on VLM
FLUENT	commercial CFD software
PBD-10	MIT's propeller blade geometry design program
PROPCAV	cavitating propeller potential flow solver based on BEM

# Chapter 1

## Introduction

### 1.1 Background

For many years, steerable thrusters have been used for main propulsion as well as for maneuvering. Such units were initially attractive for small and medium sized vessels but have been extended to larger vessels specially because of their station keeping capabilities, which are often needed in the offshore marine industry. Such devices which combine propulsion and maneuvering together are known as azimuthal thrusters. The synergy of azimuthing thruster propulsion and maneuvering, diesel electric propulsion along with hydrodynamic aspects, automation systems etc., gave birth to the idea of including an electric motor inside the thruster hub driving the propeller directly, which is now commonly known as podded propulsion.

Podded propulsors are often electric drive propulsion units, azimuthing through 360 degrees around their vertical axis. Propellers are mounted on either pulling or pushing position depending on the objective of the ship's performance, the speed and crew comfort. Various propulsion options are available ranging from one to multiple pods with single, twin or even contra-rotating propeller possibilities as shown in Figures 1.1, 1.2 and 1.3 respectively.

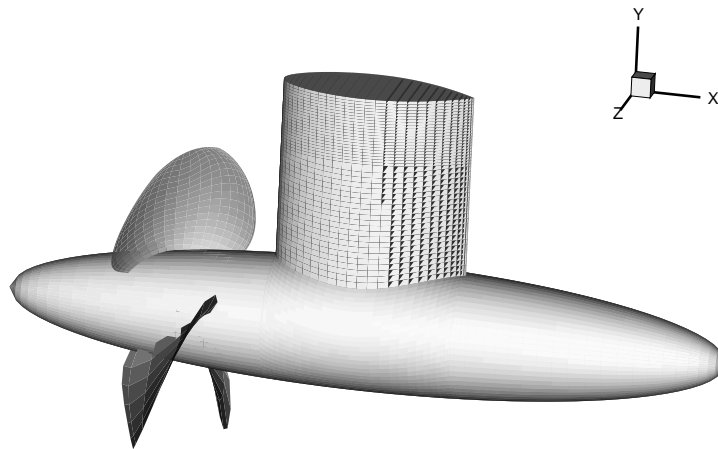


Figure 1.1: Figure showing a pull type podded unit.

The podded propulsion has a number of benefits when compared to a conventional propeller drive:

- Much higher side thrust making it ideal in Dynamic Positioning mode.
- Operation flexibility which allows for lower fuel consumption, reduced maintenance costs, and fewer exhaust emissions.
- Better maneuverability and shorter docking time, providing excellent dynamic performance, steering and control capabilities of the ship.
- Provide relatively uniform wake field to the propeller, and thus reduce unsteady forces and eliminate or minimize blade cavitation
- Result into propeller induced pressure pulses which are smaller, meaning greater comfort and lighter steel construction.

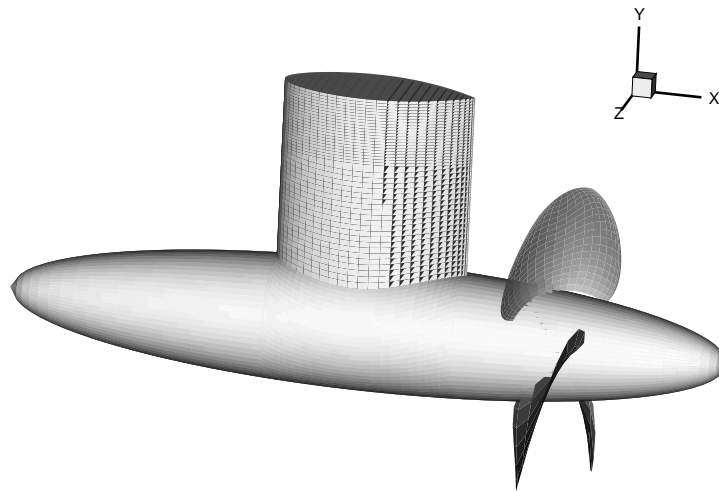


Figure 1.2: Figure showing a push type podded unit.

- Produce less noise and vibrations due to the absence of reduction gears, long shaft lines, and because of the location of propulsion motor outside machinery spaces (in the case of electric drives).
- Podded propulsion designs are quite flexible and they can be built for pushing or pulling operation, low or high speeds, and can also operate in ice conditions.
- Flexible machinery arrangement resulting in increased cargo space.

Though podded propulsors have a lot of advantages, they also have a few disadvantages. Due to a different hull form with podded propulsion, the ship's lateral area is decreased. This results in less straight line stability i.e. inability to maintain the hull's tendency to carry on along a straight line path after it is disturbed from its original path. Also due to increased steering forces and reduced lateral area, large rolling

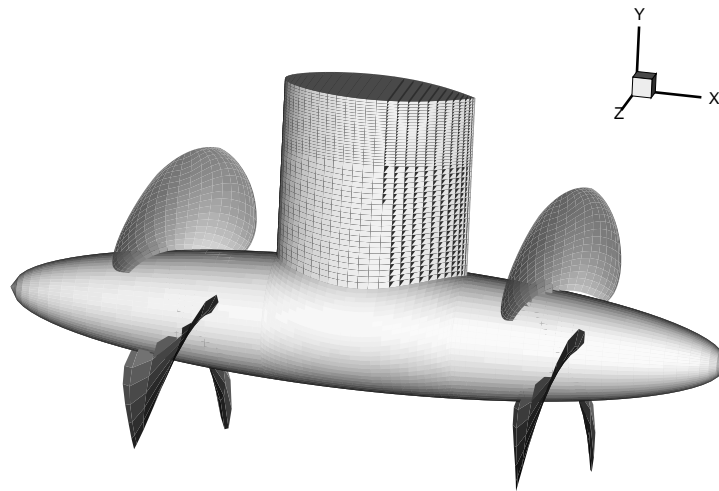


Figure 1.3: Figure showing a twin type podded unit.

motions might be induced, thus de-stabilizing the ship in turning maneuvers. A skeg (usually located at the bottom of the pod) in such cases can increase the lateral area and compensate for this problem.

The cost of a podded propulsion system compared with conventional propulsion systems is no doubt higher. This is due to the relative newness of this kind of system. But the initial higher cost is also offset by more space utilization, better maneuvering characteristics and better overall performance of the drive.

Long term integrity and reliability of these new systems has yet to be proven. Extensive CFD (Computational Fluid Dynamics) analysis and towing tank tests are required to develop a pod shape for higher performance and improved maneuverability. Though extensive experimental studies on podded propulsors have been done, only few measurements can be found in the open literature. CFD analysis and test-

ing can also verify the improvements in propulsive efficiency claimed by existing or proposed podded propeller designs. An optimal pod shape can be developed by minimizing the total forces on the podded system. A strut can also improve efficiency. More information is required on the design loads and design specifications of the podded propulsors in service, as they differ significantly from conventional propellers.

## 1.2 Motivation

The study of the flow around the propeller and the pod and strut unit is of increasing importance due to the extensive use of podded propulsors. In this context, the evaluation of the overall forces acting on the pod and strut unit, along with those on the propeller(s) becomes important.

The inflow at the propeller plane, observed in the absence of the propeller, is referred to as the *nominal wake*. This flow field contains strong vorticity components upstream of the hull due to the presence of boundary layer. Potential flow solvers to model the flow around the rotating propellers neglect this vorticity. The inflow to the propeller must thus be “corrected” to include the interaction between the propeller and the vorticity in the flow. This adjusted inflow is referred to as the *effective wake*.

The presence of a multi-component propulsor increases the complexity of the problem. Each component can be treated as a separate blade row and solved for separately. The effective wake *seen* by each of the component is affected by the presence of the other components. Thus the solver has to model the interaction between the inflow and the multiple components of the propulsion system. This can

be done by coupling a Vortex Lattice Method (VLM) based potential solver [Kinnas et al. 1998a] with an axisymmetric or a three-dimensional Euler solver [Choi 2000; Choi and Kinnas 2003, 2001, 2000c] based on a Finite Volume Method (FVM) or a Reynolds Averaged Navier Stokes (RANS) solver (e.g. FLUENT). Iterations are performed between these two methods, with VLM solving for each of the components individually, and the FVM solving for the appendages, namely pod and strut. This process is continued till a converged solution is obtained. The propellers are represented as body forces in the Euler or RANS solver. The integration of pressures and frictional stresses on the surface of the pod and strut provides the force which must be added to that produced by the propeller(s).

An optimum design can be chosen to minimize the flow separation and the associated drag [Vartdal et al. 1999], and can thus lead to better efficiency of the podded propulsor.

When an Euler solver or a potential flow solver is used, the effects of viscosity are not captured. The viscous force on the unit is still calculated by using a friction coefficient provided for example by the ITTC formula [Lewis 1988] . But the changes that might occur on the flow field due to the effects of viscosity, i.e. the pressure distribution along the pod, as well as the effective wake to each propeller, are lost. This has an effect on the predicted propeller performance. To take into account the viscous effects, the VLM is coupled with the commercial code FLUENT (visit <http://www.fluent.com> for details), which is a viscous flow RANS solver.

### 1.3 Objectives

The objectives of this research are to:

- 1) Develop and validate a method to predict the performance of podded propellers and the flow field around the unit.
- 2) Estimate the effects of viscosity on the propeller performance and the total force on the system.

Preliminary results of the method were presented by [Kakar 2002], and validation studies as well as improvements were carried out by [Gupta 2004].

To obtain the objectives the following have been done,

- The flow domain around the pod and strut is discretized in 3-D.
- A Finite Volume Method (FVM) based Euler solver and a potential flow solver are used to predict the flow around the pod and strut. The latter will be used to verify the results of the former.
- The flow field around the propellers and the forces on the propeller blades are determined using a Vortex Lattice Method (VLM) [Kinnas et al. 1998a].
- Coupling of the FVM and the VLM is done in an iterative manner to incorporate the effect of the pod on the propeller(s), and vice versa.
- Coupling of FLUENT and the VLM is carried out to predict the effects of viscosity.

- Comparisons are carried out between the results of the two methods and with measurements from experiments.

## **1.4 Overview**

This thesis can be summarized into eight main chapters.

- Chapter 1 presents the Introduction, Motivation, Objectives and Overview of the whole thesis.
- Chapter 2 presents the literature review of the previous work done in the field of flow past podded propulsors.
- Chapter 3 presents the detailed numerical formulation of the axisymmetric and three-dimensional Finite Volume Method (FVM) based Euler Solver and the corresponding boundary conditions. This chapter also presents the detailed formulation of the Boundary Element Method (BEM) used for the validation and comparison with the FVM. For completeness, a brief overview of the Vortex Lattice Method (VLM) based potential solver, used to solve the flow around the propeller, is also provided. The details of the implementation of coupling between the various methods is also covered.
- Chapter 4 presents results from various methods for axisymmetric pods in the absence of propellers. Several grid dependence studies are performed.
- Chapter 5 presents the results of axi-symmetric pod and propeller interaction (i.e. ignoring the effects of the strut) and looks into the effects of viscosity.

- Chapter 6 presents results of various methods in the case of a strut and pod, in the absence of propellers. Grid dependence studies are also performed.
- Chapter 7 presents the summary and conclusions of the thesis. Recommendations for future work are also provided.

## Chapter 2

### Literature Review

This chapter discusses previous work related to the prediction of the performance of open, multi-component and podded propulsors

#### 2.1 Vortex Lattice Method

A vortex lattice method was introduced for the analysis of fully wetted unsteady performance of marine propellers subject to non-uniform inflow by [Kerwin and Lee 1978]. The method was later extended to treat unsteady cavitating flows by [Lee 1979] and [Breslin et al. 1982] using the linearized cavity theory. The linear theory cannot capture the correct effect of blade thickness on cavity, and [Kerwin et al. 1986] and [Kinnas 1991] implemented the leading edge correction to take into account the non-linear blade thickness effect and the defect of linear cavity solution near a round leading edge. The code developed was named PUF-3A. The method was later extended to predict unsteady partial cavitation with the prescribed mid-chord cavity detachment location by [Kinnas and Fine 1989], and the steady supercavitation by [Kudo and Kinnas 1995]. The search algorithm for cavity detachment in the case of back mid-chord cavitation was added by [Kinnas et al. 1998b] and

[Griffin 1998], and the code was re-named MPUF-3A.

In MPUF-3A, the discrete vortices and sources are placed on the mean camber surface of the blade. A robust arrangement of the singularities and the control point locations is employed to produce more accurate results [Kinnas and Fine 1989]. The unknown strengths of the singularities are determined so that the kinematic and dynamic boundary conditions are satisfied at the control points on the mean camber surface. The kinematic boundary condition requires the flow to be tangent to the mean camber surface. The dynamic boundary condition requires the pressure on the cavity to be equal to the vapor pressure, and is applied only at the control points in the cavitating part of the blade.

The latest version of MPUF-3A also includes wake alignment in the circumferentially averaged inflow [Greeley and Kerwin 1982], non-linear thickness-loading coupling [Kinnas 1992] and [Kosal 1999], the effect of hub and duct [Kinnas, Lee, Gu and Gupta 2004], and wake alignment in the case of inclined shaft [Kinnas and Pyo 1999], and variable thickness hub (pod) [Natarajan 2003].

## **2.2 Effective Wake Prediction**

Effective wake is the “corrected” inflow to the propeller which is evaluated by subtracting the velocities induced by the propeller (determined by MPUF-3A) from the total inflow (determined by the 3-D Euler or RANS solver). Accurate *effective* wake prediction is important in determining the unsteady loadings and the cavity extent and volume on the propeller blades, as well as the magnitude of the predicted pressure fluctuations on the hull induced by the propeller.

Experimental investigations and theoretical studies using steady axisymmetric Euler equations were first presented by [Huang et al. 1976; Huang and Cox 1977] and [Huang and Groves 1980; Shih 1988], respectively. Later, effective wake prediction methods using Reynolds Averaged Navier-Stokes (RANS) equations were developed for axisymmetric flow applications. [Stern et al. 1988*a,b*; Kerwin et al. 1994, 1997*a*] and [Stern et al. 1994] applied the RANS equations to non-axisymmetric applications. In both methods, the propeller was represented by body force terms in the RANS equations.

In [Choi and Kinnas 1998, 2001], [Kinnas et al. 2000], a steady 3-D Euler solver based on a finite volume approach and the artificial compressibility method, was developed for the prediction of the 3-D effective wake of single propellers in unbounded flow or in the presence of a circular section tunnel.

In [Choi and Kinnas 2003, 2000*b,a*] and [Choi 2000], a fully three-dimensional unsteady Euler solver, based on a finite volume approach and the pressure correction method, was developed and applied to the prediction of the unsteady effective wake for propellers subject to non-axisymmetric inflows. It was found that the 3-D Euler solver predicted a 3-D effective wake which was very close to the time average of the fully unsteady wake inflow. In the present work the 3-D steady Euler solver which was extended to include the effects of the presence of multiple-blade rows [Kakar 2002], is applied to the podded propulsor case.

### **2.2.1 Multi-Component Propulsors**

Multi-component propulsors can offer higher efficiencies due to the cancellation of the flow swirl downstream of the propulsor. Since each component carries only a

fraction of the required thrust, the blade loading and the overall amount of blade cavitation decreases. Types of multi-component propulsors include contra-rotating propellers, pre or post swirl propulsors, and they can be open, ducted, podded, integrated (with the hull), or internal (such as the impeller system of a waterjet).

There have been several efforts to design or predict the mean performance of two stage propulsors using a lifting line model for each one of the components. The steady or unsteady performance of two-stage propulsors has also been predicted using a lifting-surface model for each one of the components [Tsakonas et al. 1983; Kerwin et al. 1988; Maskew 1990; Hughes and Kinnas 1993, 1991; Yang et al. 1992; Hughes 1993]. [Achkinadze et al. 2003] evaluated the interaction between the blade rows using the mutually induced velocities by a method of velocity field iterations. [Kinnas et al. 2002] and [Gu and Kinnas 2003] coupled an Euler solver with a vortex lattice method to predict the performance of multi-component propulsors and their interaction with the hull.

The vortex lattice method (applied to each one of the components) has been coupled with RANS solvers in order to predict the performance of multi-component propulsors, including their interaction with the hull flow by [Dai et al. 1991; Kerwin et al. 1994], and more recently in [Warren et al. 2000].

In the present work, a vortex lattice method (MPUF3A) is applied to each one of the components (propellers), and is coupled with an Euler solver (GBFLOW-3X/-3D) and a viscous solver FLUENT, based on a finite volume method, to predict the three-way interaction among the inflow, the pod and strut, and the propellers.

### 2.2.2 Podded Propulsors

Podded propulsor units are becoming increasingly popular in modern day commercial marine vessels. A podded propulsor is defined as a *steerable pod housing an electric motor which drives an external propeller* (definition taken from [www.sew-lexicon.com](http://www.sew-lexicon.com)).

A podded propulsor can be a push type (post-swirl, the propeller is downstream of the strut), pull type (pre-swirl, the propeller is upstream of the strut), contra-rotating (two propellers, one in front of the strut, one aft of the strut, rotating in opposite directions) or twin rotating (two propellers, one in front of strut, one aft of strut, both rotating in the same direction). At high speeds, the efficiency of the push-type propulsor decreases due to the propeller operating in the wake peak of the vertical strut [Vartdal and Bloch 2001]. In contrast, the pull-type propeller provides various advantages in terms of efficiency, controllability, comfort and vessel layout [Blenkey 1997]. Twin and contra-rotating propellers are also advantageous, mainly in terms of efficiency and less cavitation. The basic idea behind contra-rotating propellers is to recover the slipstream rotational energy of the fore propeller. Also due to divided thrust between the propellers, the individual propeller loading is lower. This is beneficial as the blade area can be lower, increasing the aspect ratio of the blades which can result in higher efficiency. Lower loading also results in decrease of cavitation.

[HYDROCOMP 1999] states that the efficiency of podded propulsors decreases on account of the large hub ( $\geq 30\%$  of propeller radius) and design features, such as variable pitch distribution to *off-load* the tip and root areas, and a forward leading rake to increase the distance from the propeller to the pod structure immediately aft,

are often employed. Even though the propeller itself may be a bit less efficient, the amount of efficiency improvement of the entire system over a conventional propeller is appreciable- in the order of 2% to 4%. This observation highlights the need for accurate design and computational tools in order to develop novel pod geometries which offer a distinct advantage over conventional propellers.

Computational modeling of podded propulsors involves adapting computational grids around complex geometries. With the improvement in computer speeds and grid generation techniques, recently several researchers have applied CFD to podded propulsors. Recently the analysis of fluid flow around podded propulsors was performed based on potential flow method by [Ghassemi and Allievi 1999] and viscous flow method by [Sanchez-Caja et al. 1999]. [Hsin et al. 2002] developed a design tool for pod geometries based on a coupled viscous/potential flow method. Preliminary results of a coupled Euler solver/Potential flow method for podded propulsors were presented in [Kakar 2002], [Gupta 2004] and in [Kinnas, Lee, Gu and Gupta 2004]. Coupled potential lifting surface/RANS algorithms have been used on hulls integrated with propulsors by [Kerwin et al. 1997*b*] and [Warren et al. 2000].

Experiments on the performance characteristics and on the maneuvering forces of different types of pod systems have been performed at the Technical University of Gdansk and published in [Szantyr 2001*b*].

The popularity of podded propulsors has in fact grown so much that a conference was held in Newcastle, UK, exclusively for podded propulsors. The focus of the conference was on design technology, motion responses, maneuvering and modeling of podded propulsors. [Ohashi and Hino 2004] uses a Navier-Stokes solver with an unstructured grid and [Chicherin et al. 2004] uses a RANS code to predict the

performance of the podded propulsors. [Islam et al. 2004] uses a panel method in the time domain to predict the performance of podded propulsors.

## Chapter 3

### Formulation and Numerical Implementation

The detailed numerical formulations of the Finite Volume Method (FVM) and the Vortex Lattice Method (VLM) used is presented in this chapter. Section 3.1 and 3.2 describe the formulation and the solution method of the Euler equations in steady flow. This chapter also provides an overview of the Vortex Lattice Method (VLM) and the formulation of the Boundary Element Method (BEM). The methods are described in detail in [Choi 2000; Choi and Kinnas 2003, 2000c, 2001; Kakar 2002; Gupta 2004], and are summarized in this work.

#### 3.1 Continuity and Euler Equations

The vector form of the continuity and the momentum (Euler) equations for incompressible flows can be written as follows

$$\nabla \cdot \vec{v} = 0 \quad (3.1)$$

$$\hat{\rho} \frac{\partial \vec{v}}{\partial \hat{t}} + \hat{\rho} \vec{v} \cdot \nabla (\vec{v}) = -\nabla \hat{p} + \hat{\rho} \vec{f} \quad (3.2)$$

where  $\vec{v}$  is the total velocity;  $\vec{f}$  is the body force per unit mass;  $\hat{\rho}$  is the density of the fluid;  $\hat{p}$  is the pressure; and  $\hat{t}$  is the time. In the above equations,  $(\hat{\cdot})$  denotes a dimensional variable.

It is more convenient to express the above equations in non-dimensional form. Distances are non-dimensionalised by the propeller radius,  $R$ , and the velocities are made non-dimensional by a reference velocity, which is taken to be the ship speed,  $V_s$ . In equation form the variables can be represented as,

$$(x, y, z) = \frac{(\hat{x}, \hat{y}, \hat{z})}{R} \quad (3.3)$$

$$\vec{v} \equiv (u, v, w) = \frac{(\hat{u}, \hat{v}, \hat{w})}{V_s} \quad (3.4)$$

$$\vec{f} \equiv (f_x, f_y, f_z) = \frac{(\hat{f}_x, \hat{f}_y, \hat{f}_z)}{\hat{\rho} V_s^2 R^2} \quad (3.5)$$

$$t = \frac{\hat{t}}{R/V_s}, \quad p = \frac{\hat{p}}{\hat{\rho} V_s^2} \quad (3.6)$$

With these dimensionless variables, the unsteady incompressible continuity and Euler equations can be rewritten as follows:

$$\nabla \cdot \vec{v} = 0 \quad (3.7)$$

$$\frac{\partial \vec{v}}{\partial t} + \vec{v} \cdot \nabla(\vec{v}) = -\nabla p + \vec{f} \quad (3.8)$$

### 3.2 Steady Euler Solver

The three-dimensional steady Euler solver is used to solve the flow around the pod and strut. The governing equations are discretized using the FVM and the artificial compressibility method [Chorin 1967] is adopted to compute the pressure and velocity fields. A ship fixed coordinate system is used for the 3-D steady Euler formulation as shown in Figure 3.1. The center of the propeller is considered as the origin of the coordinate system. The numerical method is described in detail in [Choi 2000] and [Choi and Kinnas 2001]. They are summarised in the next sections, for completeness.

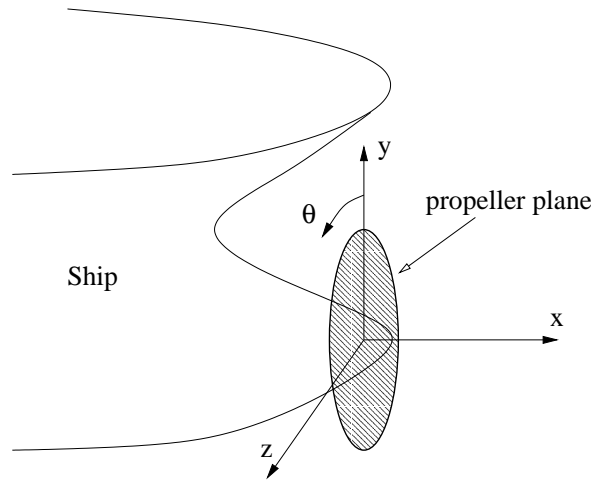


Figure 3.1: Ship-fixed Cartesian coordinate system (taken from [Choi 2000])

A cartesian coordinate system is used for the 3-D formulation, while a cylindrical coordinate system is used for the axisymmetric formulation.

### 3.2.1 Axisymmetric Steady Euler Solver

The axisymmetric Euler solver is used to solve the flow around axisymmetric bodies like the pod without the strut. The artificial compressibility method [Chorin 1967] is used to solve the Euler equations. In this method the incompressible flow equations are given a hyperbolic character (changed from their mixed parabolic-elliptic character) by adding a pseudo time derivative of the pressure. At convergence, the time derivative is zero and the solution satisfies the incompressible flow equations. The addition of pseudo unsteady terms to the Euler equations gives the following form to the governing equation:

$$\frac{\partial \mathbf{U}}{\partial t^*} + \frac{\partial \mathbf{F}}{\partial x} + \frac{\partial \mathbf{G}}{\partial r} = \mathbf{Q} \quad (3.9)$$

with

$$\mathbf{U} = \begin{bmatrix} rp \\ ru_x \\ ru_r \\ ru_\theta \end{bmatrix}, \quad \mathbf{F} = \begin{bmatrix} ru_x/\beta \\ r(u_x^2 + p) \\ ru_xu_r \\ ru_xu_\theta \end{bmatrix}, \quad \mathbf{G} = \begin{bmatrix} ru_r/\beta \\ ru_xu_r \\ r(u_r^2 + p) \\ ru_ru_\theta \end{bmatrix}, \quad (3.10)$$

$$\mathbf{Q} = \begin{bmatrix} 0 \\ rf_x \\ u_\theta^2 + rf_r \\ -u_ru_\theta + rf_\theta \end{bmatrix}$$

The term  $\beta$  is the artificial compressibility parameter which has a constant value. The smaller the  $\beta$ , the more “incompressible” the equations are. The value of  $\beta$  is kept between 0.07 and 0.1 [Choi 2000].

### 3.2.2 Three-dimensional Steady Euler-Solver

The method of artificial compressibility [Chorin 1967] is applied again in the three-dimensional steady Euler solver. The 3-dimensional governing equations are similar to the axisymmetric equations except that there are three components now. The form of the dimensionless governing equation, after the addition of the pseudo time derivative is:

$$\frac{\partial \mathbf{U}}{\partial t^*} + \frac{\partial \mathbf{F}}{\partial x} + \frac{\partial \mathbf{G}}{\partial y} + \frac{\partial \mathbf{H}}{\partial z} = \mathbf{Q} \quad (3.11)$$

The terms  $\mathbf{U}$ ,  $\mathbf{F}$ ,  $\mathbf{G}$ ,  $\mathbf{H}$ , and  $\mathbf{Q}$  are defined as follows.

$$\mathbf{U} = \begin{bmatrix} p \\ u \\ v \\ w \end{bmatrix}, \quad \mathbf{F} = \begin{bmatrix} u/\beta \\ u^2 + p \\ uv \\ uw \end{bmatrix}, \quad \mathbf{G} = \begin{bmatrix} v/\beta \\ uv \\ v^2 + p \\ vw \end{bmatrix}, \quad (3.12)$$

$$\mathbf{H} = \begin{bmatrix} w/\beta \\ uw \\ vw \\ w^2 + p \end{bmatrix}, \quad \mathbf{Q} = \begin{bmatrix} 0 \\ f_x \\ f_y \\ f_z \end{bmatrix}$$

The application of a finite volume scheme leads to the application of the divergence theorem on the Euler equations. The integral form of the equations read as:

$$\frac{\partial}{\partial t} \iiint_V U dV + \iint_S (\mathbf{F}n_x + \mathbf{G}n_y + \mathbf{H}n_z) dS = \iiint_V \mathbf{Q} dV \quad (3.13)$$

The fluid domain is discretized into hexahedral cells. The unit surface normal vector,  $\vec{n}$ , with components  $(n_x, n_y, n_z)$ , points in the outward direction from the cell. The discretisation in space is carried out by applying the equation over each cell. A second order discretisation is used in space. Ni's Lax-Wendroff method [Ni 1982] is applied for the time discretisation. That is, the variable  $\mathbf{U}$  at a particular node and at the next time (pseudo-time) step  $n + 1$ , is approximated by the following second order difference,

$$\mathbf{U}_{(i,j,k)}^{n+1} \simeq \mathbf{U}_{(i,j,k)}^n + \left( \frac{\partial \mathbf{U}}{\partial t} \right)_{(i,j,k)}^n \Delta t + \left( \frac{\partial^2 \mathbf{U}}{\partial t^2} \right)_{(i,j,k)}^n \frac{(\Delta t)^2}{2} \quad (3.14)$$

where,  $\Delta t$  is the time step size, and the superscript  $n$  represents the value at the current time step. Since this is a second order scheme in space, artificial dissipation is added to the solution to stabilise it. A second and fourth order dissipation,  $\mu_2$  and  $\mu_4$ , are scaled by time and added to the discretised formula:

$$\mathbf{U}_{(i,j,k)}^{n+1} \simeq \mathbf{U}_{(i,j,k)}^n + \sum_{cells} \delta \mathbf{U}_{(i,j,k)}^n + \Delta t (\mu_2 - \mu_4) \quad (3.15)$$

The solution around the pod and strut is solved using 3-D Euler solver called GBFLOW-3D, and its latest version can handle hull or tunnel boundaries, contra-rotating propellers, stator-rotor combinations, ducted and podded propulsors [Gu et al. 2003].

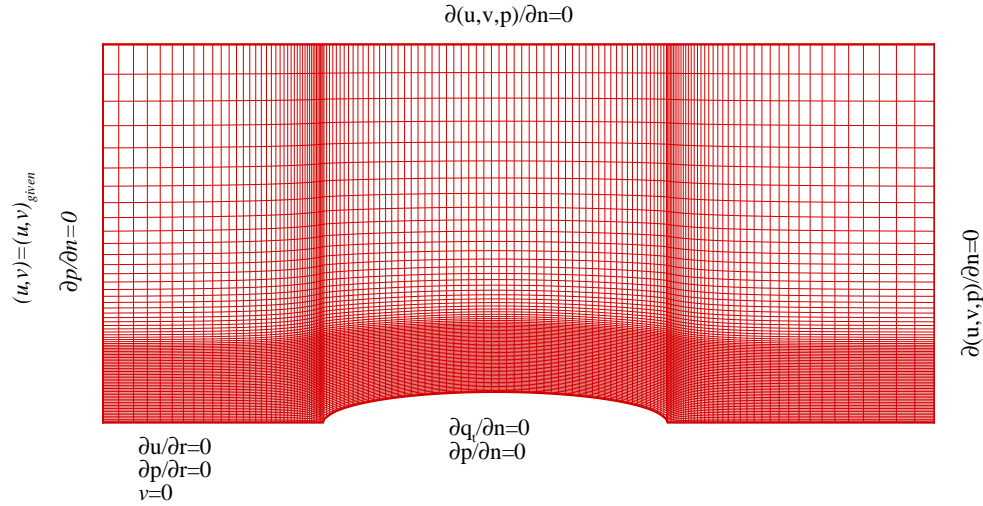


Figure 3.2: 2-D grid showing the boundary conditions used for the axisymmetric Euler solver

### 3.2.3 Boundary Conditions

#### *Axisymmetric solver*

Figure 3.2 shows the boundary conditions used for the axisymmetric run. The boundary conditions are as follows:

- Inflow or upstream boundary

The velocities are set to a given value, and the first derivative of the pressure with respect to the axial direction is taken equal to zero.

$$\begin{aligned} (u, v) &= (u, v)_{given} \\ \frac{\partial p}{\partial n} &= \frac{\partial p}{\partial x} = 0 \end{aligned} \quad (3.16)$$

where,  $(u, v)_{given}$  are the components of the inflow far upstream of the podded propulsor.

- Outflow or downstream boundary:

The derivatives of all the velocity components and the pressure with respect to the axial direction are taken equal to zero.

$$\frac{\partial(u, v, p)}{\partial n} = \frac{\partial(u, v, p)}{\partial x} = 0 \quad (3.17)$$

- Axis of Rotation/Bottom boundary

For the axisymmetric solver, the first derivative of the axial velocity and the pressure along the radial direction are taken equal to zero. The radial velocity is taken equal to zero.

$$\begin{aligned} \frac{\partial u}{\partial r} &= 0 \\ \frac{\partial p}{\partial r} &= 0 \\ v &= 0 \end{aligned} \quad (3.18)$$

- Top/Far-stream boundary

The derivatives of the velocity components and the pressure along the normal direction at the boundary are taken equal to zero.

$$\frac{\partial(u, v, p)}{\partial n} = 0 \quad (3.19)$$

- Hull (or pod) boundary

A free-slip boundary condition is imposed on the pod. The derivatives of the tangential velocity and the pressure along the normal direction at the boundary are taken

equal to zero.

$$\frac{\partial q_t}{\partial n} = 0, \quad \frac{\partial p}{\partial n} = 0 \quad (3.20)$$

The tangential velocity derivative actually should include the effect of curvature which are ignored here but can be found in [Kinnas, Lee, Gu, Yu, Sun, Vinayan, Kacham, Mishra and Deng 2004].

### *3D-solver*

Figure 3.3 shows the boundaries in the three-dimensional Euler solver. Boundary conditions need to be applied on seven boundaries as stated below

- The upstream boundary where the flow enters the domain (Inflow)
- The downstream boundary where the flow leaves the domain (Outflow)
- The hull boundary at the top
- The outer boundary, or the far field (under the pod)
- The centerline boundary (this is the boundary along the axis of the pod, before the pod leading edge and after the pod trailing edge)
- The pod and strut boundary
- The periodic boundary which connects the beginning and the end of the indices along the circumferential direction (this occurs before the strut leading edge and after the strut trailing edge, as shown in Figure 3.5).

The applied boundary conditions are shown in Figure 3.3. The top boundary is treated as a hull, while the side and bottom boundaries are treated as far-stream

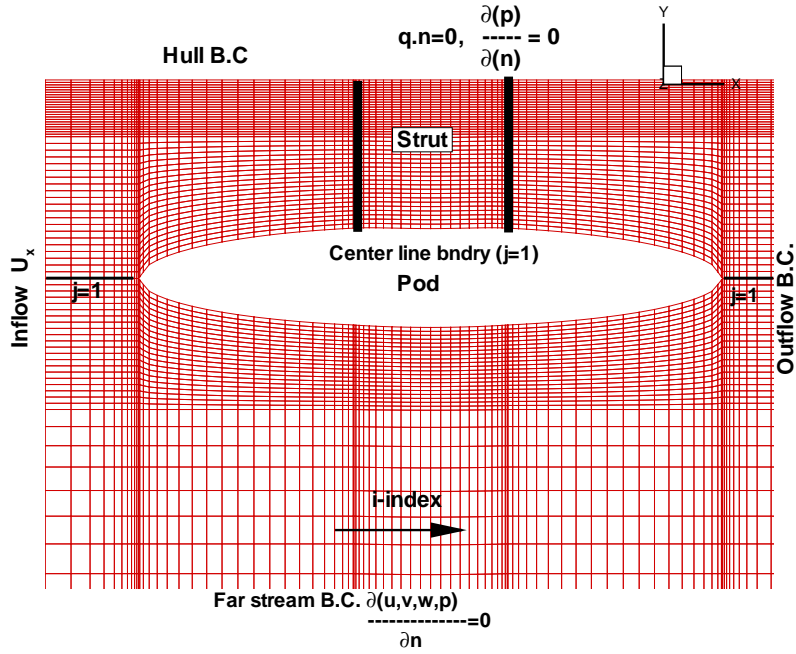


Figure 3.3: Boundary conditions for the Euler solver which evaluates the flow around the pod and strut in the presence of the propeller, (taken from [Gupta 2004]).

boundaries (they should be located sufficiently far from the propeller and pod plane as shown in Figure 3.4).

The boundary conditions applied in the present method are summarized next

- Upstream boundary

Each velocity component is set to a given value, and the first derivative of the pressure with respect to the axial direction is taken equal to zero.

$$(u, v, w) = (u, v, w)_{given} \quad (3.21)$$

$$\frac{\partial p}{\partial n} = \frac{\partial p}{\partial x} = 0 \quad (3.22)$$

where,  $(u, v, w)_{given}$  are the components of the inflow far upstream. A first order differencing scheme is used, i.e. the pressure value at the second  $i$  index (i.e.  $i = 2$ )

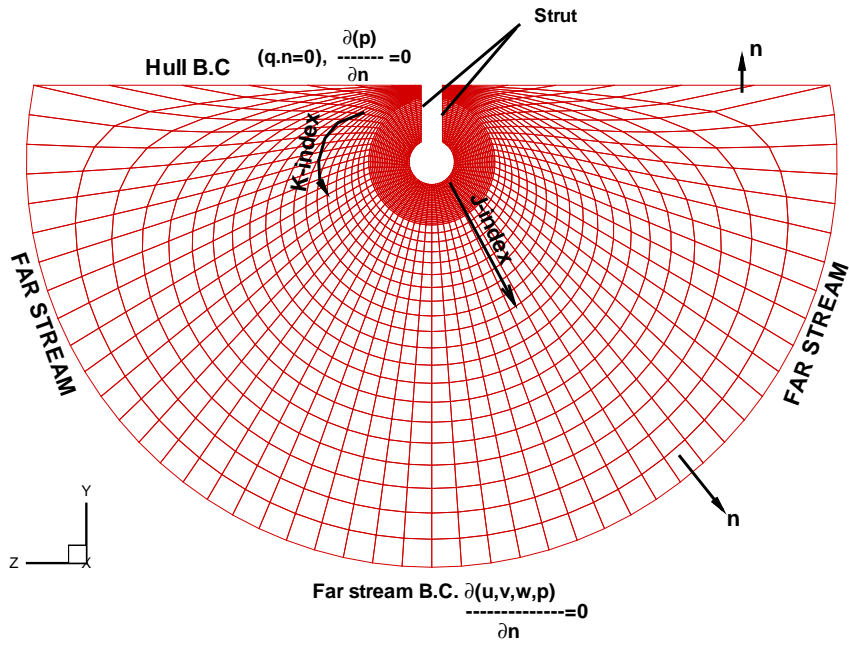


Figure 3.4: Boundary conditions on the domain at an axial location showing pod and strut (no repeat boundary), (taken from [Gupta 2004])

is taken equal to that at the first index (i.e.  $i = 1$ ).

- Downstream boundary:

The derivatives of all the velocity components and the pressure with respect to the axial direction are taken equal to zero.

$$\frac{\partial(u, v, w, p)}{\partial n} = \frac{\partial(u, v, w, p)}{\partial x} = 0 \quad (3.23)$$

Similar to the case of the upstream boundary, the derivatives are evaluated using a first order differencing scheme.

- Center line boundary ( $j=1$  line in the grid):

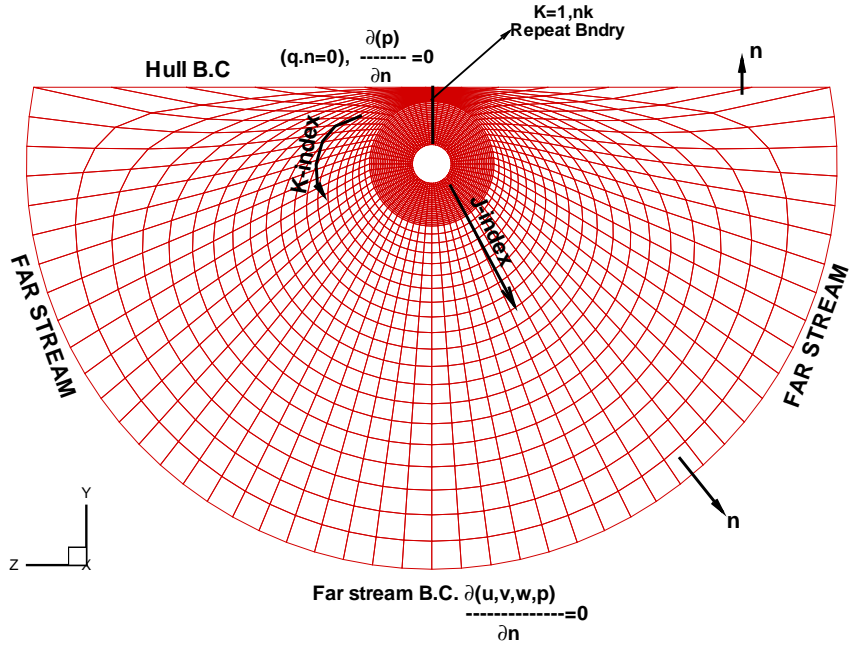


Figure 3.5: Boundary conditions on the domain at an axial location showing the repeat boundary ( $k = 1, N_k$ ), (taken from [Gupta 2004])

In the case of the axisymmetric solver, the first derivatives of the axial velocity and pressure along the radial direction as well as the tangential and radial velocities are taken equal to zero. In the case of the three-dimensional solver, the values of the velocities and pressure at the center boundary ( $j = 1$ ) are taken equal to the average of the values at ( $j = 2$ ), over all ( $k = 1$  to  $N_k$ ), as shown next.

$$(u, v, w, p)_{(i,1,k)} = \frac{1}{N_k} \sum_{k=1, N_k} (u, v, w, p)_{(i,2,k)} \quad (3.24)$$

where,  $N_k$  is the number of nodes in the circumferential direction.

- Far-stream boundary :

The derivatives of the velocity components and the pressure along the normal direction at the boundary are taken equal to zero.

$$\frac{\partial(u, v, w, p)}{\partial n} = 0 \quad (3.25)$$

The derivatives are also implemented via first order differencing.

- Hull boundary ( $j = N_j$ )

Free slip *wall* boundary condition is applied on the hull boundary. The normal component of the velocity is set equal to zero, and the derivatives of the other velocity components and the pressure with respect to the direction normal to the hull are taken equal to zero.

$$\begin{aligned} \frac{\partial p}{\partial n} &= 0 \\ \vec{q} \cdot \vec{n} &= 0 \\ \vec{q} &= \vec{q}_t + \vec{q}_n \\ \frac{\partial(\vec{q}_t)}{\partial n} &= 0 \end{aligned} \quad (3.26)$$

where,  $\vec{q}$  is the total velocity,  $q = (u, v, w)$ ,  $\vec{q}_t$  is the component of the total velocity tangent to the boundary,  $\vec{q}_n$  is the component of the total velocity along the normal direction. To achieve this, first the tangent vector to a cell node on the hull boundary is determined. Then, the velocity is considered at the cell node adjacent to the hull inside the domain [i.e. cell(i,Nj-1,k)] and its component in the calculated tangential direction is evaluated. This velocity component is taken to be equal to that on the cell node on the hull.

- Pod and strut boundary ( $j = 1$  on pod,  $k = 1, N_k$  on strut)

The boundary condition on the pod and strut boundaries shown in Figure 3.4 is similar to the hull boundary condition. The pod and strut is considered as a *wall*, and the flow should not penetrate the *wall*. To achieve this, the normal component of the velocity is set equal to zero, and the derivatives of the other velocity components and the pressure with normal direction to the boundary are put as zero. The equation used is the same as equation 3.26.

- Periodic or Repeat boundary as shown in Figure 3.5 (three-dimensional problem only):

$$(u, v, w, p)_{k=1} = (u, v, w, p)_{k=N_k} \quad (3.27)$$

where  $k$  is the index along the circumferential direction.

### 3.3 Vortex Lattice Method

This section presents an overview of the vortex lattice method based potential flow solver which is used for the analysis of the cavitating propeller flow. The complete formulation of the potential flow solver and the vortex lattice method may be found in chapter 6 by Kinnas in the book of [Ohkusu 1996].

The *vortex lattice method* which solves for the unsteady potential flow field around a cavitating propeller has been used successfully since the method was first developed in [Kerwin and Lee 1978], [Lee 1979] and [Breslin et al. 1982].

In the vortex lattice method, a special arrangement of line vortex and source lattice is placed on the blade mean camber surface and its trailing wake surface. There are three types of singularities:

- (a) the vortex lattice on the blade mean camber surface and the trailing wake surface which represents the blade loading and the trailing vorticity in the wake,
- (b) the source lattice on the blade mean camber surface which represents the blade thickness, and
- (c) the source lattice throughout the predicted sheet cavity domain which represents the cavity thickness.

This method is classified as a lifting surface method because the singularities (vortices and sources) are distributed on the blade mean camber surface, as opposed to the other class of method, the surface panel method, in which the singularities are distributed on the actual blade surface.

The unknown strengths of the singularities are determined so that the kinematic and the dynamic boundary conditions are satisfied at the control points on the blade mean camber surface.

The *Kinematic Boundary Condition* requires that the flow velocity be tangent to the mean camber surface, and is applied at all control points.

The *Dynamic Boundary Condition* requires that the pressure on the cavitating part of the blade mean camber surface be equal to the vapor pressure, and is applied only at the control points that are in the cavitating region.

### **3.4 Boundary Element Method**

The numerical formulation for the Boundary Element Method (BEM) used to solve for the flow around the pod and strut, in the absence of the propeller, subject to inflow

at zero yaw angle was presented in [Gupta 2004]. The method has been summarized in this section for completeness.

### 3.4.1 Formulation of Potential Flow around a Pod and Strut

The fluid flow field around an axisymmetric pod and a 3-D pod and strut unit without the presence of a propeller, with uniform inflow, can be solved using the BEM. The flow around the pod and strut is assumed to be incompressible, inviscid and irrotational. Then, the fluid domain can be represented by using the perturbation potential  $\phi(x, y, z)$ , defined as follows:

$$\vec{q}(x, y, z) = \vec{U}_{in}(x, y, z) + \nabla\phi(x, y, z) \quad (3.28)$$

where  $\vec{q}$  is the total velocity and  $\vec{U}_{in}$  is the inflow velocity to the pod and strut

The perturbation potential has to satisfy Laplace's equation inside the fluid domain, as follows,

$$\nabla^2\phi = 0 \quad (3.29)$$

The effect of wake of the strut is not considered since the inflow is along the pod axis.

The potential on the pod and strut satisfies the equation 3.30, which is obtained from Green's third identity.

$$2\pi\phi_p = \int_{S_B} \left[ \phi_q \frac{\partial G(p; q)}{\partial n} - G(p; q) \frac{\partial \phi_q}{\partial n} \right] dS \quad (3.30)$$

where points  $p$  and  $q$  correspond to the field and variable points respectively on the integration.  $G(p; q) = 1/R$  is the Green's function,  $R(p; q)$  is the distance between the

points  $p$  and  $q$ , and  $\vec{n}$  is the normal vector to the surface of the body  $S_B$  pointing into the field domain.

The above integral equation is discretized using quadrilateral panels with constant strength dipole and source distributions over each panel on the pod and strut surfaces.

### 3.4.2 Kinematic Boundary Condition on the Body

The kinematic boundary condition requires that the flow is tangent to the body and there are no normal velocity components to the wall. Hence,

$$\frac{\partial \phi}{\partial n} = -\vec{U}_{in} \cdot \vec{n} \quad (3.31)$$

where  $\vec{n}$  is the normal vector on the body surface pointing into the fluid.

### 3.4.3 Kutta Condition

The Kutta condition requires that the velocity at the trailing edge (T.E.) of the rudder to be finite.

$$\nabla \phi \text{ is finite at T.E.} \quad (3.32)$$

The Kutta condition could be enforced numerically by applying the Morino condition [Morino and Kuo 1974], which requires the difference of the potentials at the two sides of the trailing edge to be equal to the potential jump in the wake. However, for the case with *zero* degree angle of attack,  $\nabla \phi$  does not exist at the trailing edge and hence equation 3.32 is not required due to symmetry.

### 3.4.4 Hull Effects

The strut of the pod in 3-D is assumed to be attached to a flat hull on the top. Hence, to include the hull effects the image of the pod with respect to the hull must be considered. The advantage of this approach is that the hull does not need to be modeled directly, but only the influence coefficients for each source and dipole panel need to be changed to include those of their images.

## 3.5 FLUENT

FLUENT is a commercial CFD package that is used for various CFD applications and problems. In this section the numerical schemes applied to solve the flow field with the propeller included via body forces are discussed. FLUENT is used both as an inviscid and a viscous flow solver in this case. FLUENT solves the RANS equations. The Navier-Stokes (N-S) equations are transformed so that the small scale turbulent fluctuations are not directly simulated, but Reynolds Averaging is carried out. The Reynolds Averaged Navier-Stokes (RANS) equations represent transport equations for the mean flow quantities only, with all the scales of the turbulence modeled. In Reynolds averaging, the solution variables in the exact N-S equations are decomposed into the mean,  $\bar{u}_i$  and fluctuating components  $u'_i$ . Hence the parameters can be written as,

$$u_i = \bar{u}_i + u'_i \quad (3.33)$$

Substituting expressions of this form for the flow variables into the instantaneous continuity and momentum equations and taking a time average yields the RANS

equations which are shown below,

$$\frac{\partial \rho}{\partial t} + \frac{\partial \rho u_i}{\partial x_i} = 0 \quad (3.34)$$

$$\begin{aligned} & \frac{\partial \rho u_i}{\partial t} + \frac{\partial \rho u_i u_j}{\partial x_j} = \\ & -\frac{\partial p}{\partial x_i} + \frac{\partial}{\partial x_j} \left[ \mu \left( \frac{\partial u_i}{\partial x_j} + \frac{\partial u_j}{\partial x_i} - \frac{2}{3} \delta_{ij} \frac{\partial u_l}{\partial x_l} \right) \right] + \frac{\partial}{\partial x_j} (-\rho \overline{u_i' u_j'}) \end{aligned} \quad (3.35)$$

In FLUENT various solver options are available. The details of those can be found in [FLUENT 2003] solver options used are,

- Segregated solver: The governing equations are solved in a sequence i.e. separately from each other using a finite volume method.
- Pressure Equation: The SIMPLE algorithm is used, which uses a relationship between the velocity and pressure corrections to enforce mass conservation and obtain the pressure field.
- Spatial Discretisation: A Second-Order Upwind scheme is used in FLUENT for spatial discretisation. In FLUENT this is achieved at cell faces through a Taylor series expansion of the cell centered solution about the cell centroid. Hence the face value  $u_f$  is computed as,

$$u_f = u + \nabla u \cdot \Delta \vec{s} \quad (3.36)$$

where  $u$  and  $\nabla u$  are the value at the cell center and its gradient at the upstream cell, and  $\Delta \vec{s}$  is the displacement vector from the upstream cell centroid to the face centroid.

- Turbulence Model: The  $k - \epsilon$  and *ReynoldsStressModel(RSM)* turbulence models are used for viscous cases in our problem. The  $k - \epsilon$  model is a two

equation model in which the solution of two separate transport equations allows the turbulent velocity and length scales to be independently determined. It is a semi-empirical model. Details of the calculation of parameters for this model are provided in Section 4.2.3. The RSM model closes the RANS equations by solving the transport equations for the Reynolds stresses, together with an equation for the dissipation rate. This results in five additional equations in 2D flows.

### **3.6 Coupling to determine pod and propeller interaction**

In the present methods, the effective inflow is used as the propeller inflow. To achieve this, first the induced velocities, due to the propeller sources and dipoles, are calculated at the effective wake location. The solution from the Euler or RANS solver gives the total velocity at that location. Subtracting the propeller induced from the total velocities, the effective velocity is obtained. In this coupled Euler or RANS/potential flow calculation, the propeller is solved by using the VLM based potential solver MPUF-3A. The inviscid flow field around the propeller and pod unit is solved using the Euler solver GBFLOW-3X or 3D or inviscid FLUENT. The viscous flow field around the podded unit is calculated using viscous FLUENT.

#### **3.6.1 GBFLOW or FLUENT/MPUF-3A coupling**

The coupling of GBFLOW or FLUENT with MPUF3A provides a way of analyzing the interactions among propeller, pod and strut. In the coupling MPUF3A is first solved for the potential flow distribution around the propeller and the pressure distributions on the blade are evaluated. The pressure distributions are then converted

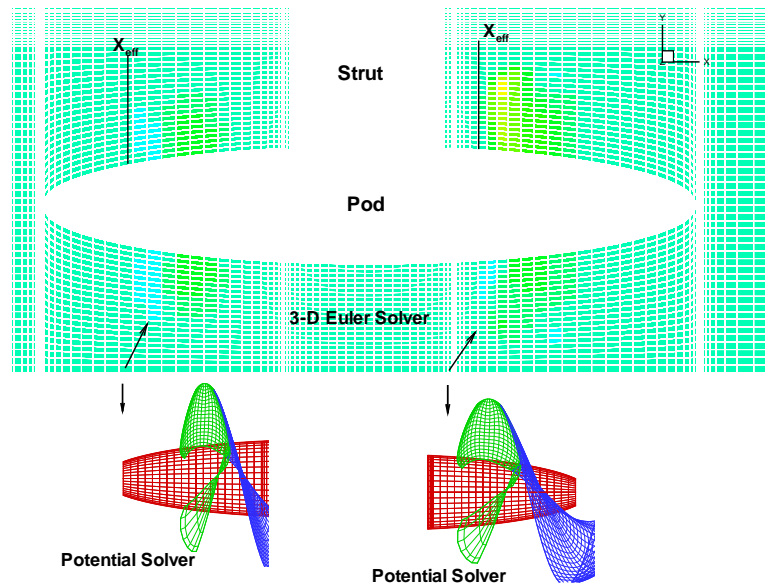


Figure 3.6: Pictorial representation of the coupling of the Finite Volume Method and the Vortex Lattice Method (from [Kinnas, Gu, Gupta and Lee 2004]).

into body force terms which represent the propeller in GBFLOW or in FLUENT. In FLUENT this is done by defining a User-Defined Function which incorporates the source terms in the Euler/RANS equations. GBFLOW or FLUENT is then solved, with the body force terms and appropriate boundary conditions, in the whole fluid domain which includes the pod and strut. From the solution, the total velocity at the effective wake location for each propeller is obtained. The propeller induced velocities are calculated via MPUF-3A, by summing the effects of all singularities representing the blade and its wake. The effective velocity is then calculated as the difference of the total from the propeller induced velocity. This is now used as the new inflow velocity to each propeller. Iterations are carried out between the methods till convergence is achieved. A pictorial representation of the iterative process is shown in Figure 3.6 [Kinnas, Gu, Gupta and Lee 2004].

### *Interpolation of body forces in FLUENT*

As mentioned earlier, the pressure distribution obtained from MPUF3A is converted into body forces which are then incorporated into GBFLOW/FLUENT. This incorporation in FLUENT is done via GBFLOW. Once the body forces are calculated by GBFLOW, and as the grids of GBFLOW and FLUENT are not the same, interpolation is carried out to assign body forces to cells in FLUENT. In GBFLOW, the body forces are known at the nodes of the GBFLOW grid. However, FLUENT is a cell centered scheme. The location of the cell centroids in the FLUENT grid is first determined. Then linear interpolation in both directions,  $x$  and  $r$  is carried out between the data available from GBFLOW and the interpolated body forces are assigned to the cell centroids in the FLUENT grid. This coupling with FLUENT has been carried out only for the case of axisymmetric flow.

### **3.6.2 Coupling of Non-dimensional Forces from FVM and VLM**

The propeller force given by MPUF-3A is in the form of  $K_T$  and  $K_Q$  values, where  $K_T$  is the thrust coefficient and  $K_Q$  is the torque coefficient.  $K_T$  is defined as

$$K_T = \frac{F}{\hat{\rho} n^2 D^4} \quad (3.37)$$

where  $D$  is the diameter of the propeller and  $n$  is the number of revolutions per second of the propeller. The advance ratio  $J_s$  is defined as

$$J_s = \frac{V_s}{nD} \quad (3.38)$$

To couple the forces obtained from GBFLOW-3D and MPUF-3A, both should be non-dimensionalized in a similar manner. Non dimensional force in GBFLOW is

given by equation 3.5

$$F_{GB} \equiv (f_x, f_y, f_z) = \frac{(\hat{f}_x, \hat{f}_y, \hat{f}_z)}{\hat{\rho} V_s^2 R^2}$$

using equation 3.37 and equation 3.38, we get

$$K_T = \frac{F}{\hat{\rho} n^2 D^2 D^2} = \frac{F}{4 \hat{\rho} \frac{V_s^2}{J_s^2} R^2} = \frac{F}{\hat{\rho} V_s^2 R^2} \times \frac{J_s^2}{4} = F_{GB} \times \frac{J_s^2}{4} \quad (3.39)$$

In GBFLOW the frictional force on the surface of the pod and strut is evaluated by using the formula:

$$F_{FR} = C_f \rho V_s^2 S \quad (3.40)$$

where, S is the surface area of the pod and strut, and  $C_f$  is a uniformly applied frictional coefficient, provided by the ITTC formula (equation 4.7). Making the equation 3.40 non-dimensional, we get

$$F_{FRND} = \frac{C_f \rho V_s^2 S}{\rho V_s^2 R^2} \quad (3.41)$$

$$F_{FRND} = \frac{C_f S}{R^2} \quad (3.42)$$

On the other hand, FLUENT is a dimensional code and all input and output obtained from FLUENT are in dimensional form. Hence they need to be handled appropriately. The first step is to dimensionalise the pressure forces obtained from the VLM and convert them to dimensional body forces. This is carried out in two steps. First, the forces from VLM are converted to body forces in a similar manner as done for GBFLOW and the non-dimensionalising is as shown in equation 3.5. Next the body forces are converted to dimensional form in the User Defined Function as,

$$F_{FL} = F_{GB} \times \hat{\rho} V_s^2 R^2 \equiv (f_x, f_y, f_z) \times \hat{\rho} V_s^2 R^2 \quad (3.43)$$

Once the solution is obtained from FLUENT and the total flow field is known, the velocities are to be used to calculate the effective wake. Accordingly, the velocities,  $\vec{V}_{FL}$ , resulting from FLUENT are non-dimensionalised as,

$$U = V_{FL}/V_s \quad (3.44)$$

### 3.6.3 BEM/MPUF3A coupling

The coupling between BEM (applied on the pod) and MPUF-3A (applied on the propeller) is carried out via induced potentials and induced velocities. More specifically the pod affects the propeller via induced velocities and the propeller affects the pod via induced potentials. This problem is also solved iteratively. This approach should help estimate the accuracy of the currently implemented image model in MPUF-3A. In the iterative procedure, first, MPUF-3A is solved to obtain the potential flow distribution around the propeller. The singularities associated with the blade and wake are known at this point. Next, the potentials induced by these singularities at the pod control points are calculated. After this has been done the pod problem can be solved as detailed in Section 3.4. The pod problem is now solved in a system with respect to the propeller. In addition the flow is also treated as non-axisymmetric. The governing equation 3.30 is now modified to account for the propeller effect via induced potentials. Accordingly the new equation is,

$$2\pi\phi_p = \int_{S_B} \left[ \phi_q \frac{\partial G(p; q)}{\partial n} - G(p; q) \frac{\partial \phi_q}{\partial n} \right] dS + 4\pi\phi_{pr} \quad (3.45)$$

where  $\phi_{pr}$  is the propeller induced potential at control point  $P$ .

The next step involves calculating the induced velocities at the blade control points due to the source and dipole distribution on the pod panels. MPUF-3A should then

be solved next, after accounting for the pod effect. This is done by modifying the kinematic boundary condition for the VLM. The new equation now is,

$$\sum_{\Gamma} \Gamma \vec{v} \cdot \vec{n} = -\vec{q}_t \cdot \vec{n} \quad (3.46)$$

where  $\vec{q}_t$  is the inflow velocity plus the pod induced velocity which has been modified to include the velocities induced by the pod,  $\vec{n}$  is the unit normal vector and  $\Gamma$  is the constant strength of each bound vortex. Iterations are carried out till a converged solution is obtained. The iterative procedure is shown in Figure 3.7. This procedure has been successfully implemented in the past by [Kerwin et al. 1987]. However the implementation has been unsuccessful in this case.

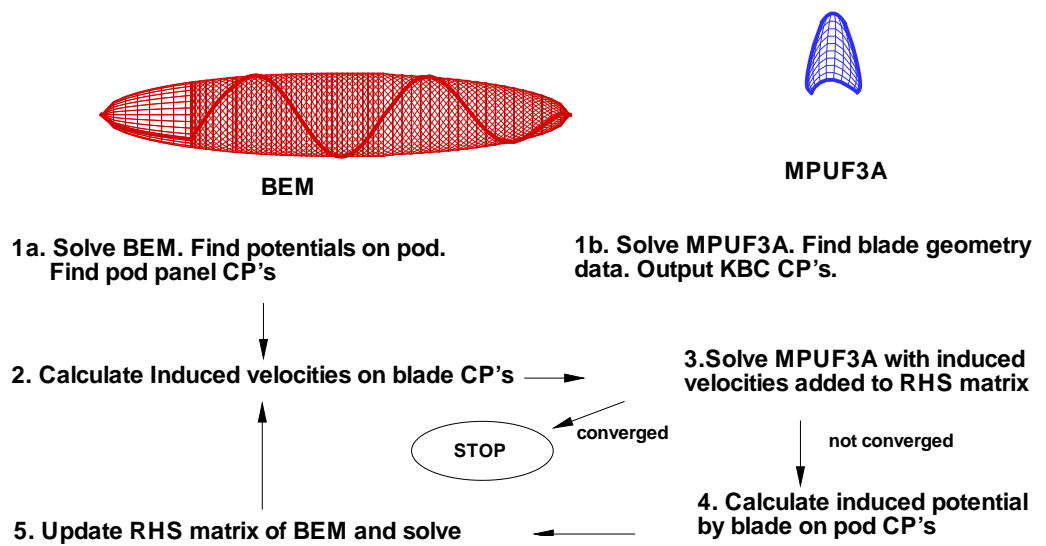


Figure 3.7: Pictorial representation of the coupling of the Boundary Element Method and the Vortex Lattice Method.

## **Chapter 4**

### **Validation and Comparisons with Other Methods - Axisymmetric Pod**

In this chapter comparisons are carried out among different axisymmetric codes, GBFLOW-3X, FLUENT and BEM. Validation of results from GBFLOW-3X is carried out by comparing on-pod and off-pod velocities and pressures with those obtained from FLUENT and BEM. Convergence studies are also carried out for all the methods. Viscous FLUENT is used to estimate the effects of viscosity. The changes in the flow field are observed but more importantly the pressures and shear stress distributions along the pod are studied. This is so because the frictional force on the pod is calculated in GBFLOW-3X using the ITTC friction formula and the accuracy of this simplification has to be assessed.

#### **4.1 Axisymmetric Euler Solver**

In the axisymmetric Euler solver, it is assumed that the pod is an axisymmetric body and the presence of the strut is ignored. The axisymmetric Euler Solver, called GBFLOW-3X, uses similar equations as the fully 3-D equations. Therefore, for the fully 3-D Euler solver to be correct, it is pertinent that the axisymmetric Euler solver

provide accurate results. The main benefit of using GBFLOW-3X is the smaller computing times than those associated with GBFLOW-3D.

The pod is assumed to be at the center of the domain. A wall (or a hull) condition which is a free slip condition given by equation 3.26 is applied on the pod, and far field conditions given by equation 3.25 are applied at those boundaries.

#### **4.1.1 Grid and Boundary Conditions**

##### *Grid Generation*

Figure 4.1 shows the grid for the axisymmetric Euler solver, which is symmetric about the axis of the pod. More cells have to be concentrated near the leading edge and trailing edge of the pod to capture the expected stagnation points. Since the fine resolution of grid points is not required near the inflow and outflow boundaries, an expansion ratio is used from the leading edge of the pod to the inflow boundary, and from the trailing edge to the outflow boundary, as shown in Figure 4.2. Along the  $j$  direction, denser grid is required close to the pod, than at the far field. Therefore the grid, as shown in Figure 4.1, is made uniform up to  $y=1.0$  (the propeller radius), and an expansion ratio is used thereafter. The geometry of the pod used for the axisymmetric runs is given in Appendix A and is the one used by Szantyr [Szantyr 2001*b*] for the experiments carried out at the Technical University of Gdansk.

The offsets of the pod (radius versus axial locations) are passed to the grid generation code. The grid points on the pod are then interpolated using a spline scheme developed by Lee, H. S. and Natarajan, S. (personal communication).

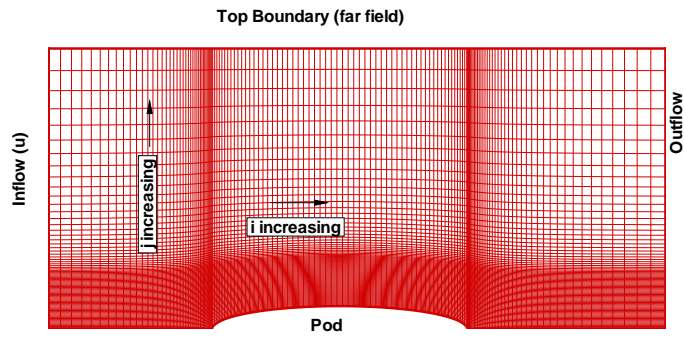


Figure 4.1: 2-D grid showing the boundaries for the axisymmetric Euler solver

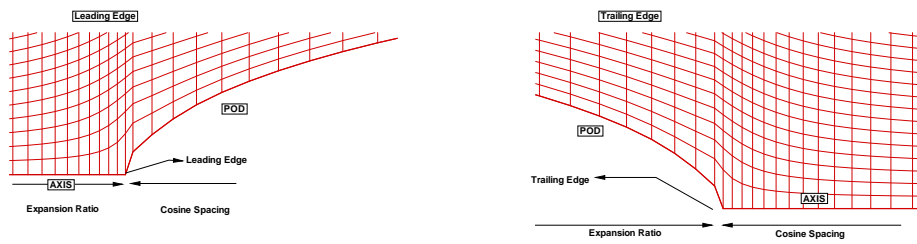


Figure 4.2: Closeup of the leading and trailing edge showing the uniform expansion ratio.

### *Boundary Conditions*

The top boundary is treated as far stream boundary. The left side boundary is the inflow, while the right boundary is the outflow. The bottom is considered as an axis of rotation. The only components of velocity required in the axisymmetric case are the axial and the radial components. Since this is axisymmetric flow the circumferential component is equal to zero (in the absence of a propeller). The details of the boundary conditions were presented in Section 3.2.3.

#### **4.1.2 Results**

GBFLOW-3X is run with different grids to obtain the flow field around the pod and the pressure force on it. As this is an inviscid solver, ideally the pressure force should be zero. However, due to discretisation errors this is not the case.

Figures 4.4 and 4.5 show the convergence of axial velocities and pressures on the body respectively, with different grids (with the number of axial nodes varied). Close-up of the different grids over the body and near the leading edge is shown in Figure 4.3.

The axial velocity and pressure contours are shown in Figures 4.6 and 4.7, respectively for the grid with  $140 \times 81$  nodes.

The total pressure force on the axisymmetric body is calculated by integrating the pressure force over the pod. Table 4.1 shows the pressure forces obtained for different grids. Effectively these values are the discretisation errors (as the force ideally should be zero) and hence can be viewed as a convergence criteria for the grids. It is seen that with increasing resolution the calculated force decreases.

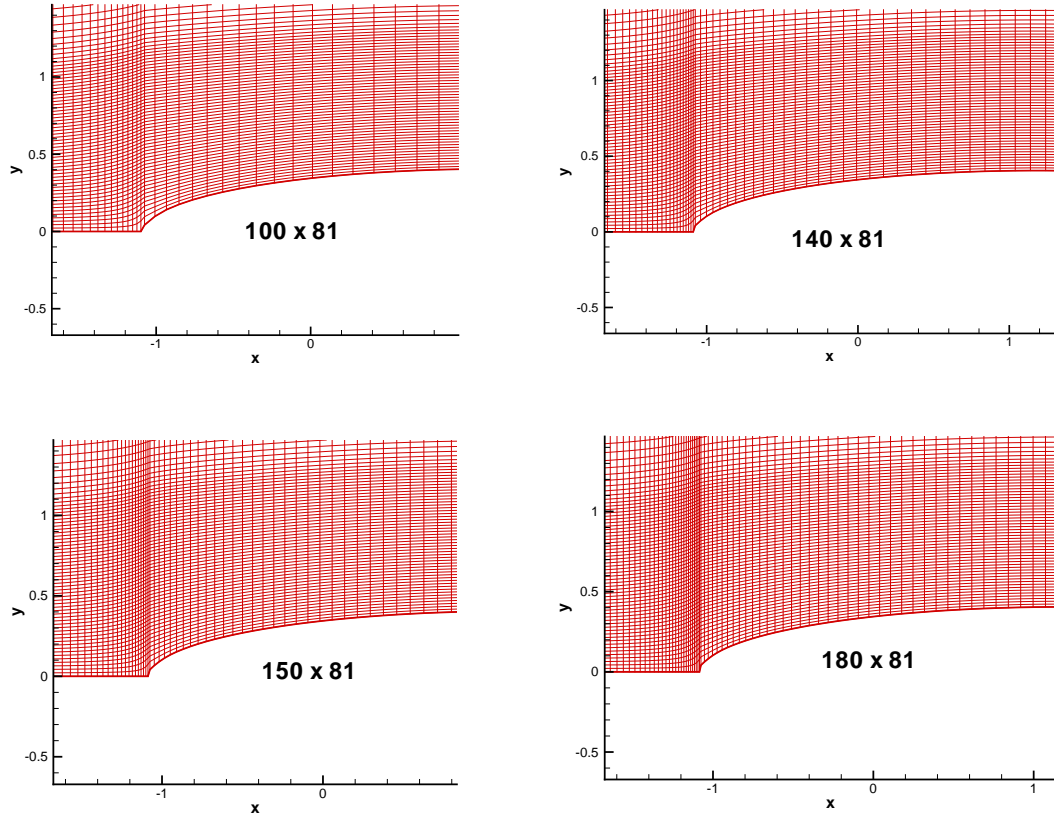


Figure 4.3: Close-up of different grids (near the leading edge) used for convergence studies in GBFLOW-3X without propeller

Grid Size $I \times J$	Pressure Force
100x81	$2.88 \times 10^{-4}$
140x81	$1.5909 \times 10^{-4}$
150x81	$1.2396 \times 10^{-4}$
180x81	$1.2565 \times 10^{-4}$

Table 4.1: Total force on the pod from Euler solver for axisymmetric runs for different grid densities. Forces made non-dimensional as given by equation 3.5

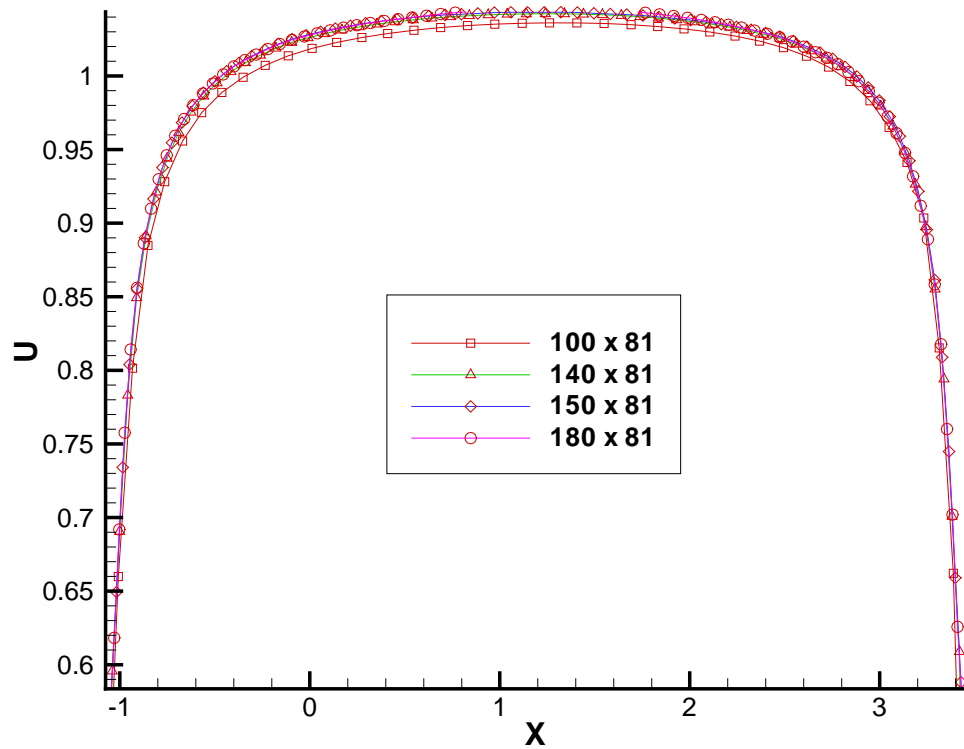


Figure 4.4: Convergence of axial velocities on body with different grids in GBFLOW-3X (number of nodes in axial direction is varied)

## 4.2 FLUENT

To validate the results of GBFLOW-3X it is essential to carry out comparisons with other methods. Inviscid axisymmetric version of FLUENT is used towards this purpose while viscous version of FLUENT is used to study the effects of viscosity on the flow field and the pressures and forces on the pod.

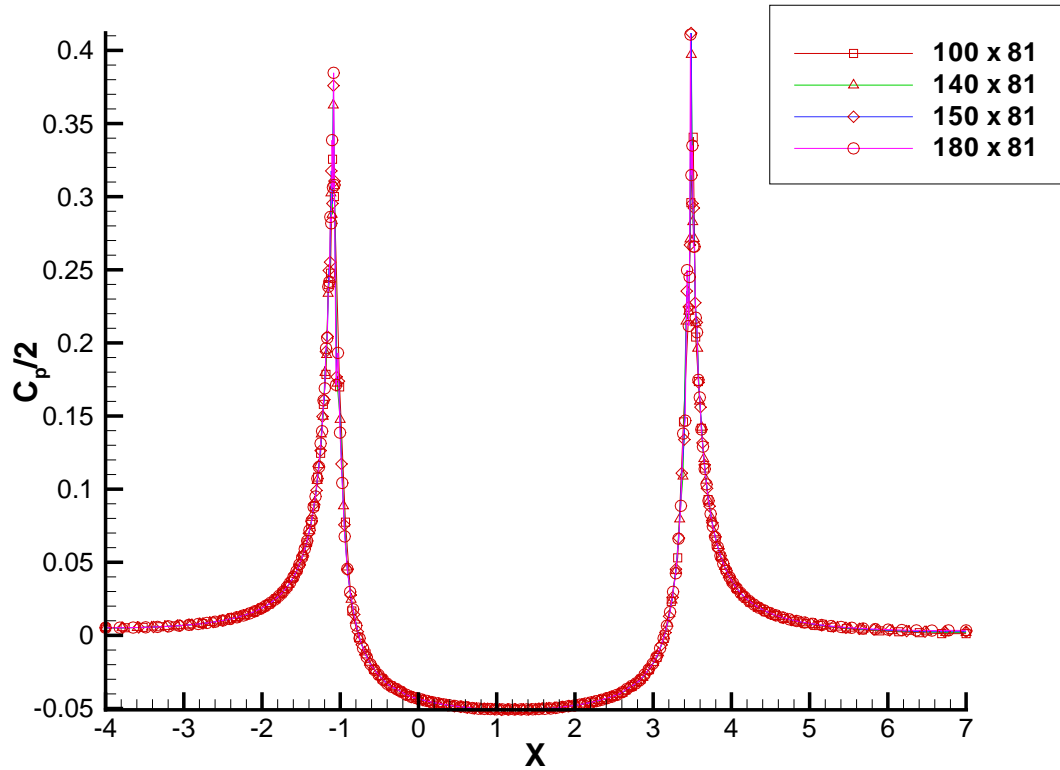


Figure 4.5: Convergence of pressure on body with different grids in GBFLOW-3X (number of nodes in axial direction is varied)

#### 4.2.1 Grid and Boundary Conditions

When inviscid runs are carried out with FLUENT, an unstructured grid is used. The main advantage of using an unstructured grid over structured grids is that it gives smoother discretisation near the leading and trailing edges and hence more cells can be concentrated near these regions. However, when inviscid runs are carried out with body forces (representing a propeller), a structured and finer grid is needed to obtain good results as shown in Chapter 5. Also it was desirable to compare the results from GBFLOW-3X and FLUENT using the same grid. Hence, the grid generated

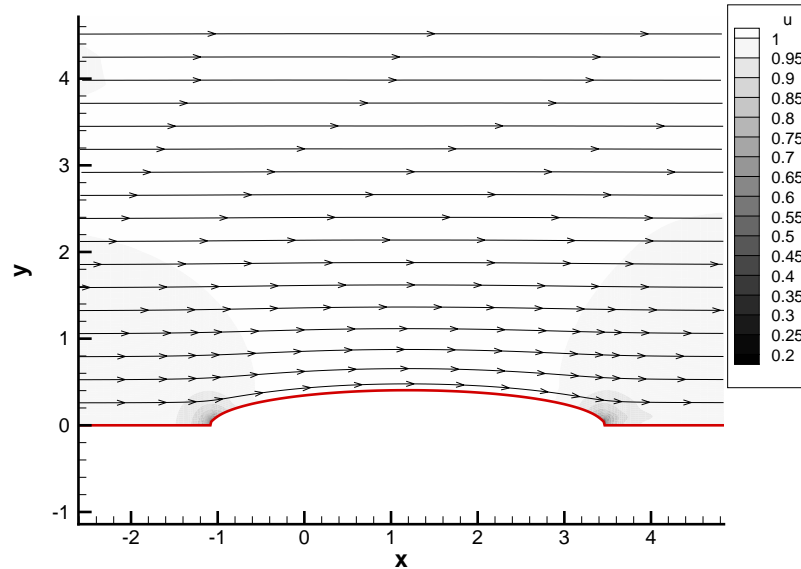


Figure 4.6: Axial velocity contour around the body from GBFLOW-3X

by GBFLOW-3X was exported to GAMBIT (grid generation code for FLUENT). So a structured grid was also used and results were compared with the unstructured one. In case of a viscous run, the unstructured grid has a boundary layer attached to the pod to capture the viscous effects as shown in Figure 4.9.

Table 4.2 gives the parameters used in FLUENT for the inviscid case. Figures 4.8, 4.9 and 4.10 show the unstructured grid used in FLUENT and a blow up near the leading edge to show the boundary layer and concentration of cells. The structured grid is shown in Figure 4.11. An expansion ratio is used on either side of the body. On the pod, a double sided expansion is used so as to concentrate more cells near the leading and trailing edges. In the y-direction, constant spacing is used till the propeller radius and then an expansion ratio is employed.

The boundary conditions are also given in Table 4.2. The left boundary is assumed

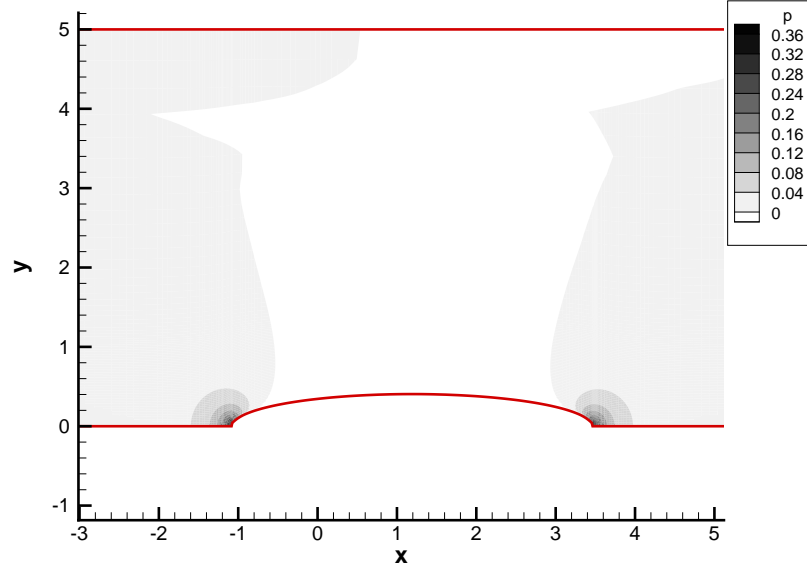


Figure 4.7: Pressure contour around the body from GBFLOW-3X

to be the inflow to the domain, and is set to

$$u = 1.0; \quad v = 0.0 \quad (4.1)$$

The top boundary is treated as a free stream boundary and assuming that there is no effect of the pod at that location, and hence, the boundary conditions are the same as given by equation 4.1. The outflow boundary on the right side of the domain is given as a pressure outlet condition:

$$\frac{\partial p}{\partial x} = 0 \quad (4.2)$$

For the pod, a wall boundary condition is given. This is a slip condition for the inviscid case, and a no-slip condition for the viscous case.

Solver	2DDP
Model	Inviscid
Method	Axisymmetric
Density	1000
Inflow	$u=1 ; v=0$
Top surface	free stream
Pod surface	wall
Centerline	Axis

Table 4.2: Run parameters for the 2-D axisymmetric inviscid version of FLUENT

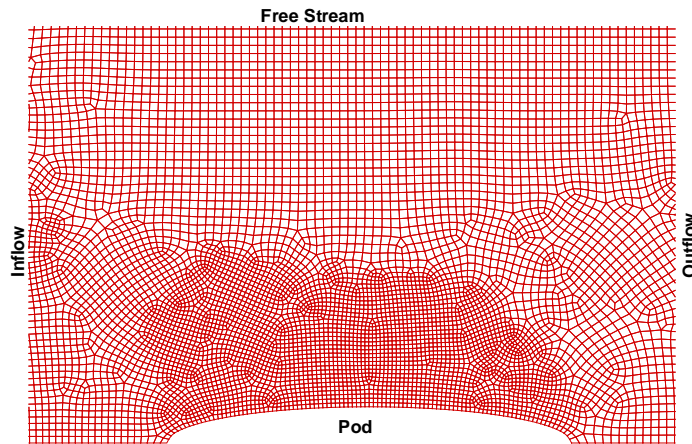


Figure 4.8: Unstructured grid used in inviscid FLUENT showing the inflow and outflow boundaries.

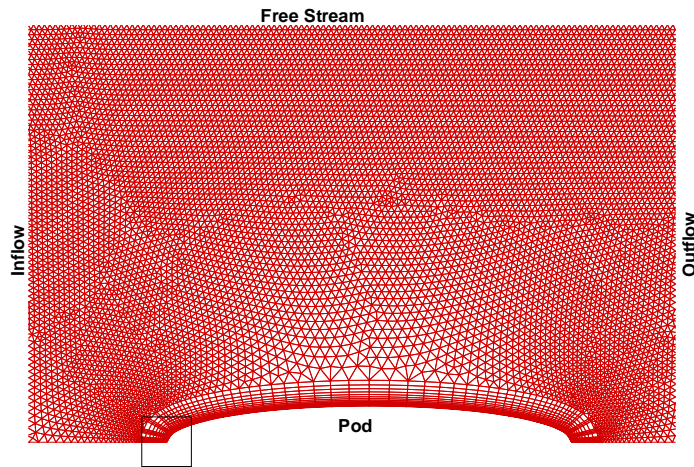


Figure 4.9: Unstructured grid used in viscous FLUENT showing the inflow and outflow boundaries.

#### 4.2.2 Results

Figures 4.12 and 4.13 show the convergence of the axial velocity and the pressure with unstructured grids, respectively. The axial velocity and pressure contours are shown in Figures 4.14 and 4.15 respectively.

Comparisons are carried out between the unstructured and structured grids to see if there are any differences in the solution. Figures 4.16 and 4.17 show the axial velocity and the pressure on the body obtained from both the grids. As can be seen they are almost the same. Figure 4.18 shows the comparison of the axial velocity at a y-plane location near the leading edge. They are almost the same, except near the body but even there they show the same tendency.

The pressure forces obtained from inviscid runs are shown in Table 4.3 The veloc-

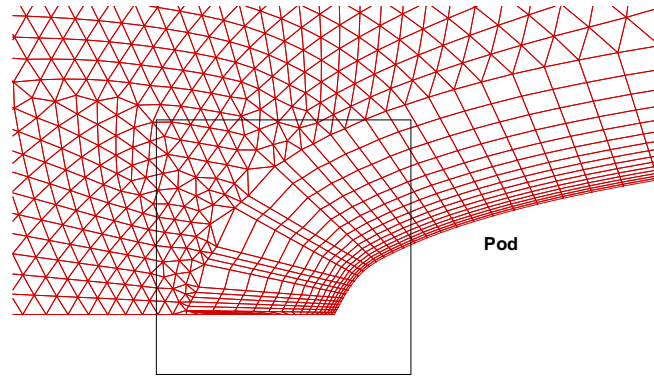


Figure 4.10: A closeup view of the grid near the pod, showing the boundary layer used and the triangular grid at the leading edge of the pod.

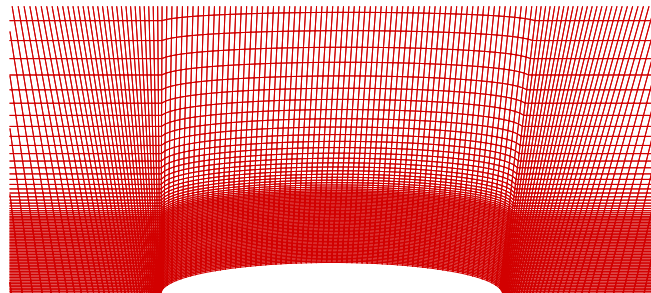


Figure 4.11: Structured grid used in FLUENT and exported from GBFLOW-3X

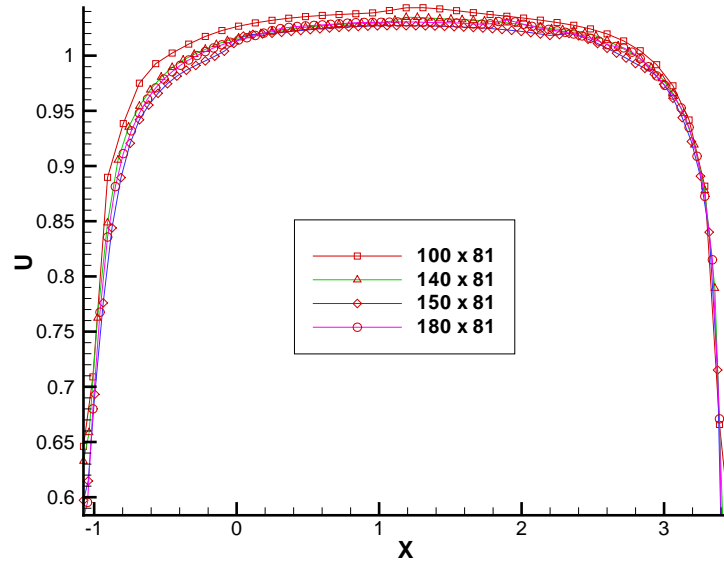


Figure 4.12: Convergence of axial velocities on body with different unstructured grids using FLUENT (inviscid)

ities and pressures obtained from GBFLOW-3X and FLUENT (inviscid) are also compared at a location near the leading edge. The location is shown in Figure 4.19. Figures 4.20 and 4.21 show the axial velocity and the pressure comparisons. The kink in the pressure near the top boundary can be attributed to the boundary condition applied on the top.

### 4.2.3 Viscous effects

Viscous runs are carried out to calculate the frictional forces on the pod and to study the changes in the velocity flow field. Runs for different Reynolds number (corresponding to experiment conditions with propeller) are done. The Reynolds number was calculated using the length of the pod as the characteristic length and the inflow

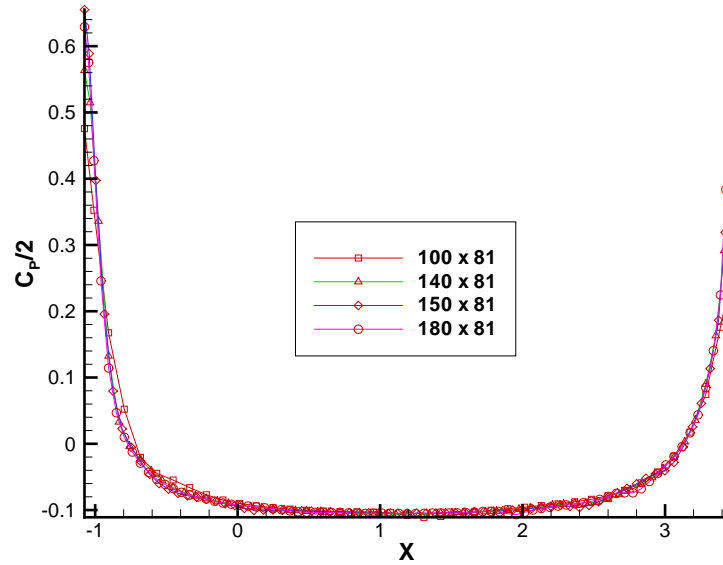


Figure 4.13: Convergence of pressure on body with different unstructured grids using FLUENT (inviscid)

velocity as the characteristic velocity. The viscous runs are done using the  $k - \epsilon$  model. The run parameters for viscous FLUENT are given in Table 4.4. The values of turbulence kinetic energy and turbulence dissipation rate are calculated from equations 4.5 and 4.6. It is important that the  $Y^+$  on the pod does not increase beyond the range where the wall functions in the boundary layer apply. Figure 4.22 shows the  $Y^+$  on the body of the pod. The maximum value of  $Y^+$  obtained by using the  $k - \epsilon$  method is 39, which is acceptable.

The dissipation constants are evaluated using the following equations.

$$Re = \frac{\rho UT}{\mu} \quad (4.3)$$

where,  $T$  is the maximum length of the pod, and  $U$  is the velocity of the flow.

Grid Size $I \times J$	Pressure Force
100x81	$3.81 \times 10^{-4}$
140x81	$1.94 \times 10^{-4}$
150x81	$1.70 \times 10^{-4}$
180x81	$1.41 \times 10^{-4}$

Table 4.3: Total force on the pod and the computed surface area from FLUENT for axisymmetric runs for different grid densities.

Solver	2DDP
Model	$k - \epsilon$
Density	998.2
Viscosity	$1 \times 10^{-3}$
$C_\mu$	0.09
Top surface	free stream
Pod surface	wall
centerline	axis
Grid type	mapped

Table 4.4: Run parameters for 2-D axisymmetric viscous FLUENT

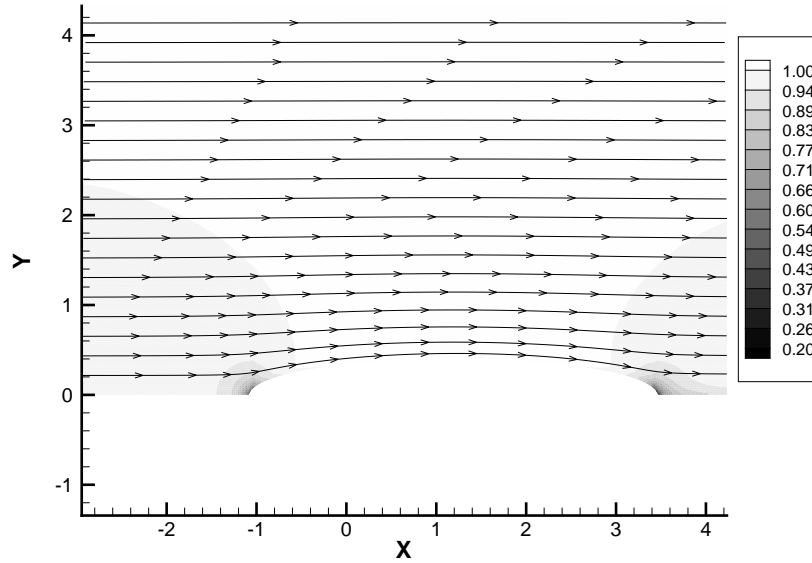


Figure 4.14: Axial velocity contour and streamlines from inviscid FLUENT

Turbulence intensity  $I$  can be written as

$$I = 0.16(Re)^{-\frac{1}{8}} \quad (4.4)$$

Turbulence kinetic energy  $k$  can be written as

$$k = \frac{3}{2}(UI)^2 \quad (4.5)$$

Turbulence length scale can be written as  $l = 0.07T$ , and turbulence dissipation rate  $\epsilon$  as

$$\epsilon = C_\mu^{3/4} \frac{k^{3/2}}{l} \quad (4.6)$$

where  $C_\mu \approx 0.09$ . The theoretical frictional coefficient can be calculated using the empirical ITTC friction formula

$$C_f = \frac{0.075}{(\log Re - 2)^2} \quad (4.7)$$

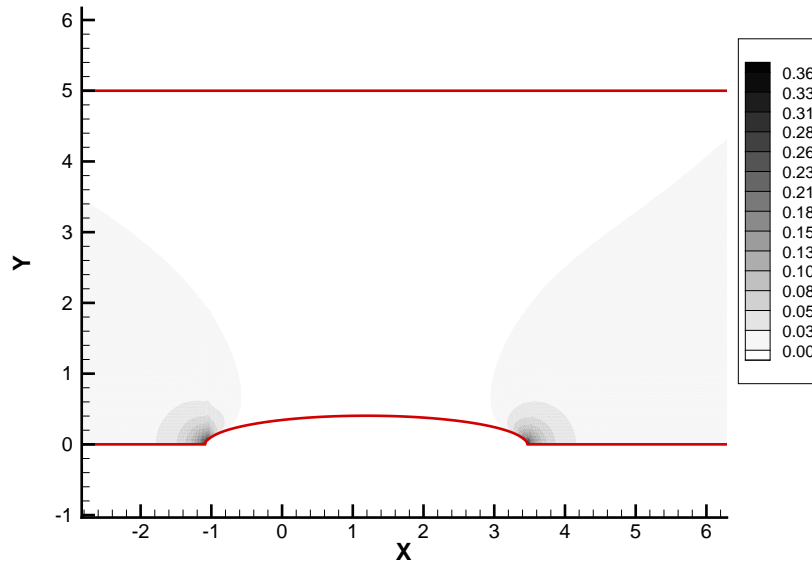


Figure 4.15: Pressure contour from inviscid FLUENT

Runs were carried out for the Reynolds number given in Table 4.5 and the corresponding  $k$  and  $\epsilon$  values.

The frictional force for all Reynolds numbers and the empirical force (used in the inviscid codes) calculated from Equation 4.7 is shown in Table 4.6. As is seen the values are very close to each other and the ITTC formula may be used for inviscid cases with reasonable accuracy.

To see what effect viscosity has on the velocities, the axial velocities for inviscid and viscous runs are compared at locations which would later serve as the effective wake locations for the fore and aft propellers. These locations are shown in Figure 4.23. The comparison between the velocities is shown in Figures 4.24 and 4.25. It can be seen that there is a small difference between the inviscid and viscous cases at the first location, but this difference increases as we move to the second location.

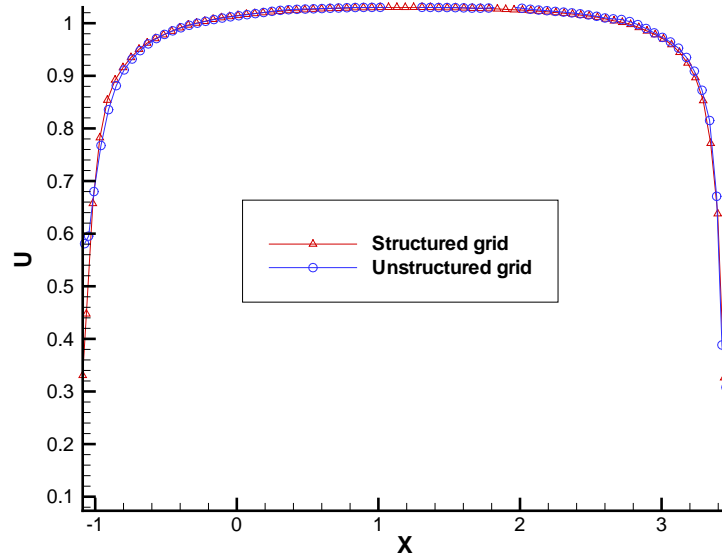


Figure 4.16: Axial velocities on body with unstructured and structured grids (FLUENT inviscid) as shown in Figures 4.8 and 4.11

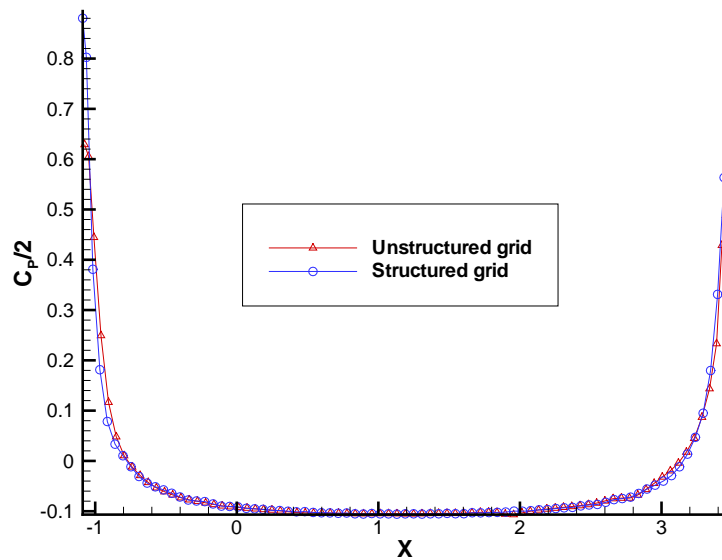


Figure 4.17: Pressure on body with unstructured and structured grids (FLUENT inviscid) as shown in Figures 4.8 and 4.11

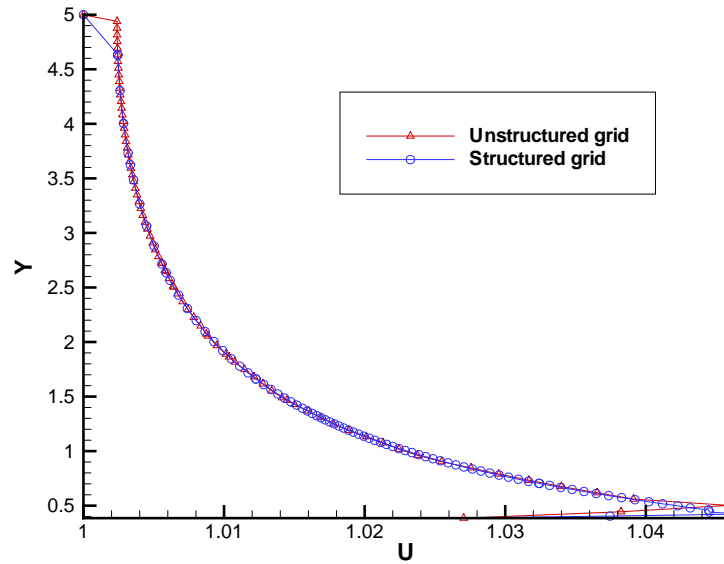


Figure 4.18: Axial velocities near leading edge with unstructured and structured grids at location shown in Figure 4.19

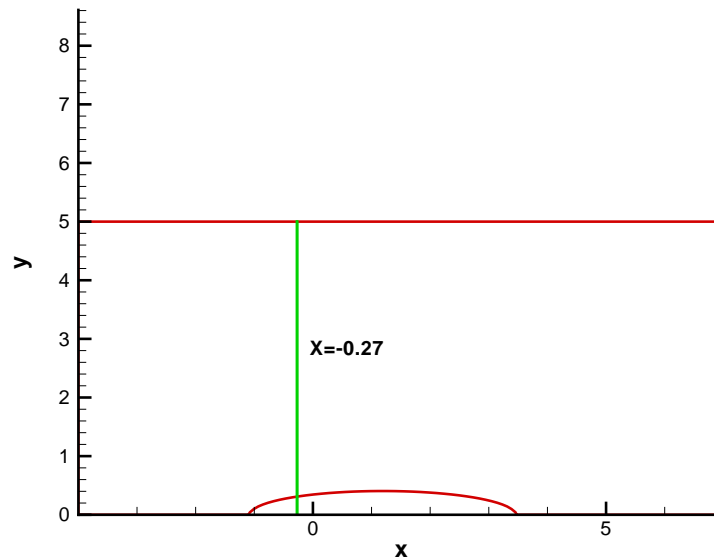


Figure 4.19: Locations where inviscid FLUENT and GBFLOW-3X axial velocities are compared

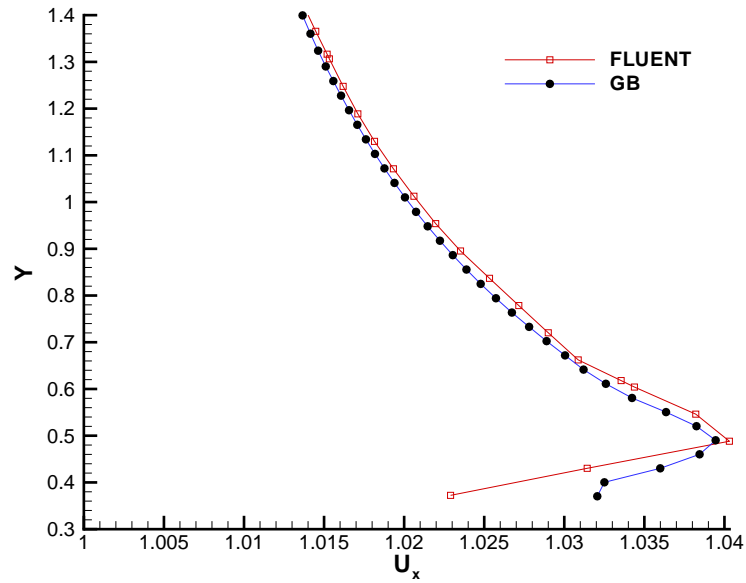


Figure 4.20: Comparison of axial velocities for inviscid FLUENT and GBFLOW-3X at given location

Re	k	$\epsilon$
$6.26 \times 10^5$	0.0056	0.00021
$8.24 \times 10^5$	0.009	0.00044
$10.5 \times 10^5$	0.0138	0.00084
$12.98 \times 10^5$	0.0200	0.00147

Table 4.5: Reynolds number,  $k$  and  $\epsilon$  for which runs are carried out using viscous FLUENT

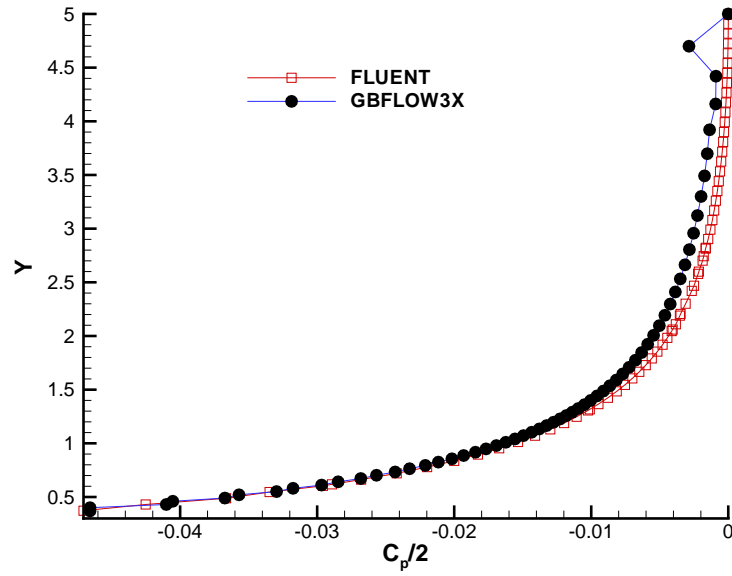


Figure 4.21: Comparison of pressure for inviscid FLUENT and GBFLOW-3X at given location

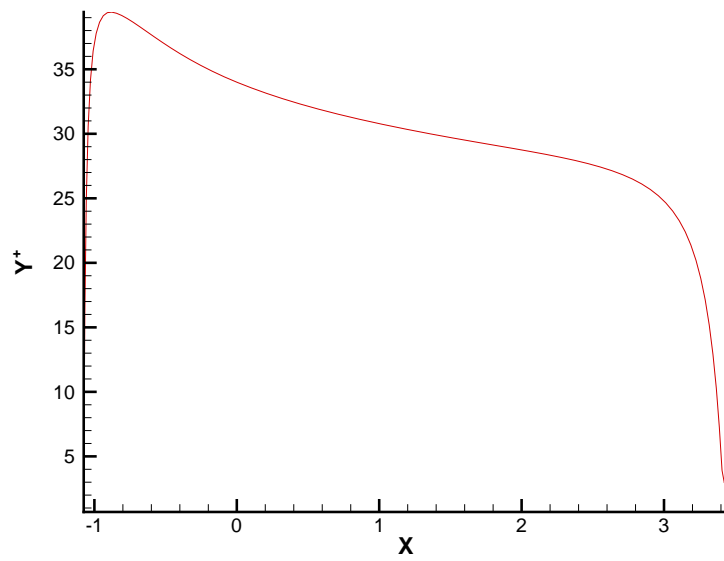


Figure 4.22:  $Y^+$  on the pod for viscous FLUENT run,  $Re=4.5 \times 10^5$

Re	$C_f ITTC$	$k - \epsilon$
$6.26 \times 10^5$	0.0096	0.0086
$8.24 \times 10^5$	0.0088	0.0083
$10.5 \times 10^5$	0.0082	0.0080
$12.98 \times 10^5$	0.0077	0.0078

Table 4.6: Comparison of mean empirical frictional force coefficient  $C_f$  with that from  $k - \epsilon$  model

This will have a significant effect in the case when we have an aft propeller. The discontinuity in the velocities predicted by the inviscid version of FLUENT near the pod, as shown in Figure 4.24, could be due to the manner in which the slip boundary condition is applied on the wall.

#### 4.2.4 Study of different models

Figure 4.25 shows the difference between the axial velocity from the inviscid and the viscous flow solver in the absence of the propeller. As can be seen the difference is not as small as someone would expect. To study this, different turbulence models in FLUENT were used. The RSM model and the  $k - \omega$  were used which provided results, much closer to the GBFLOW-3X result. This appears to be more accurate as the changes between the inviscid and viscous solvers should be near the wall region. The  $k - \epsilon$  model was also run with a grid with a very low  $Y^+ = 6$ , but the solution did not change much. The results are shown in Figure 4.25. So, a RSM model is also used to solve the case of pod with propeller.

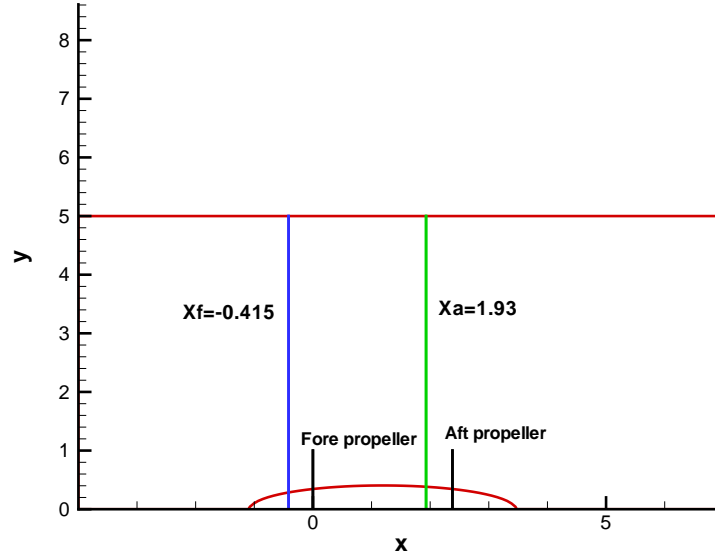


Figure 4.23: Locations for comparison of inviscid and viscous axial velocities

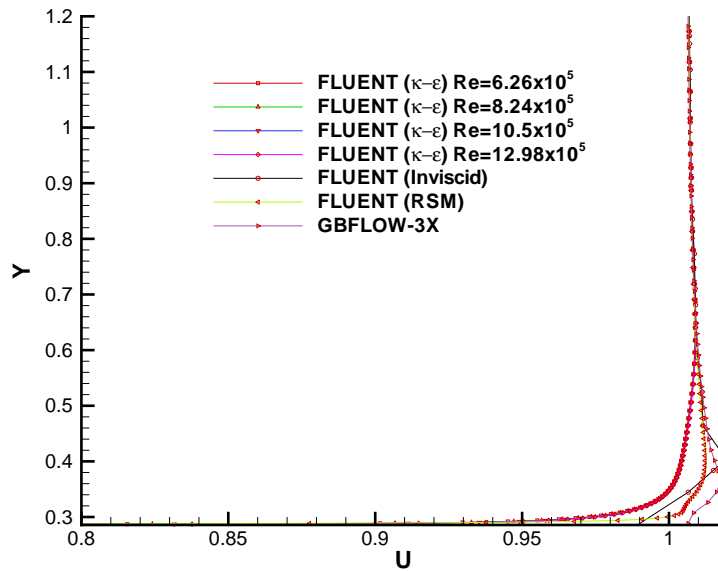


Figure 4.24: Axial velocities for different Re at  $X_f=-0.415$  location as shown in Figure 4.23.

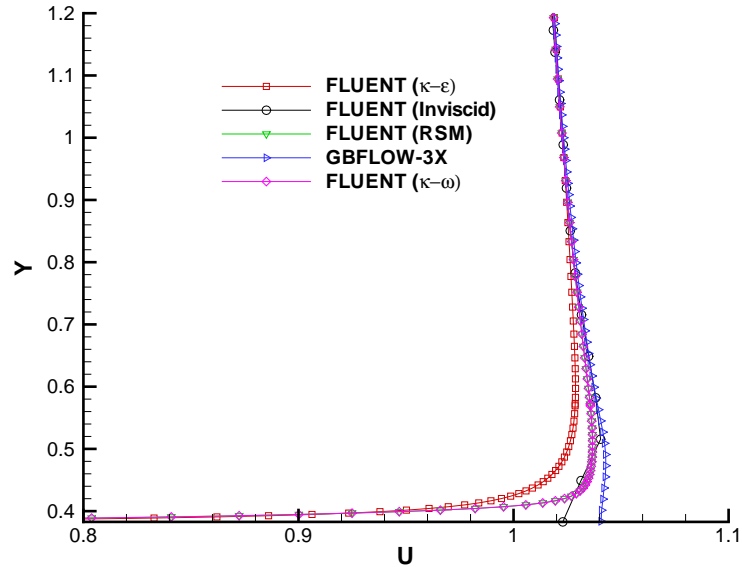


Figure 4.25: Axial velocities from different methods at  $X_a=1.93$  location as shown in Figure 4.23,  $Re = 6.26 \times 10^5$ .

### 4.3 BEM

The computation using a Boundary Element Method (BEM) code is developed to check the accuracy of the Euler solver. BEM, a potential solver, solves for the potential on the body, which could be used to evaluate the velocities and pressures. The main advantage of using BEM compared to the 3-D Euler solver is that the CPU time can be remarkably reduced. The solver though essentially axisymmetric carries out computations as a 3-D solver *i.e.* the influence coefficients are calculated based on all the panel control points and the solution is carried out for the complete matrix containing all the panel influence coefficients. Figure 4.26 shows the grid of the pod for the BEM solver.

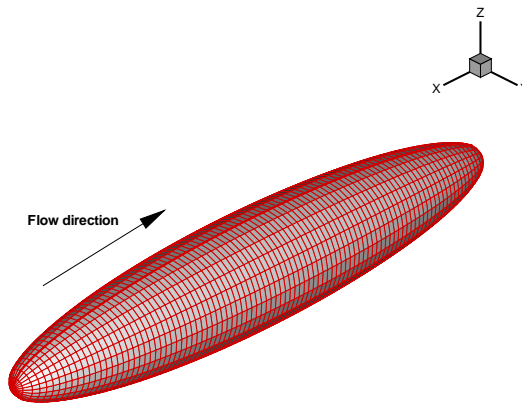


Figure 4.26: Grid used for the axisymmetric BEM solver

### 4.3.1 Results

Convergence studies are performed to understand the behavior of the results and to check their consistency. The dependence of axial velocity and pressures on the grid discretization is shown in Figures 4.27 and 4.28 respectively. Table 4.7 gives the total force from each grid obtained by integrating the non-dimensional pressures on the surface of the body. The forces are made non-dimensional as  $\frac{F}{\rho U^2 S}$ , where  $S$  is the surface area of the pod and  $U$  is the inflow velocity. It can be seen from the table 4.7 that with an increase of the grid panels on the pod, the pressure force reduces. Ideally for an inviscid case, the pressure force on the pod should be *zero*.

Figure 4.29 shows the convergence of forces with grid size for all the different methods. All the methods seem to have approximately the same rate of convergence.

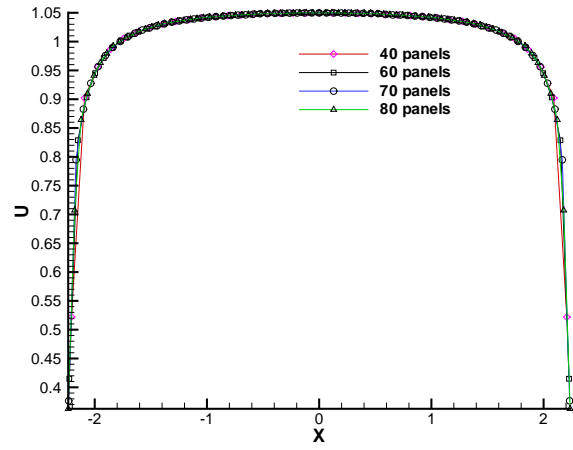


Figure 4.27: Convergence of axial velocities with different grids using BEM

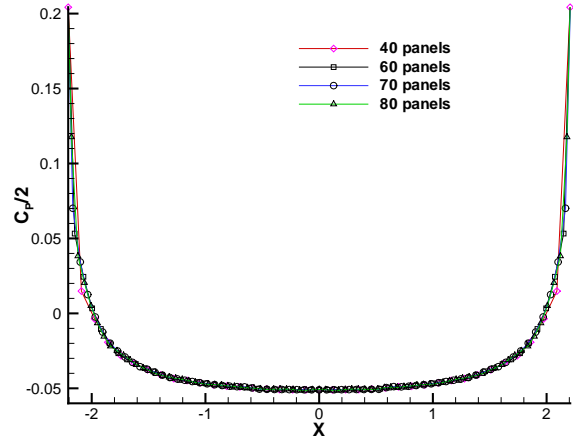


Figure 4.28: Convergence of pressure with different grids using BEM

Grid Size $I \times J$	Pressure Force
40x30	$1.984 \times 10^{-4}$
60x30	$1.288 \times 10^{-4}$
70x30	$1.106 \times 10^{-4}$
80x30	$1.041 \times 10^{-4}$

Table 4.7: Total force on the pod from BEM for axisymmetric runs for different paneling.

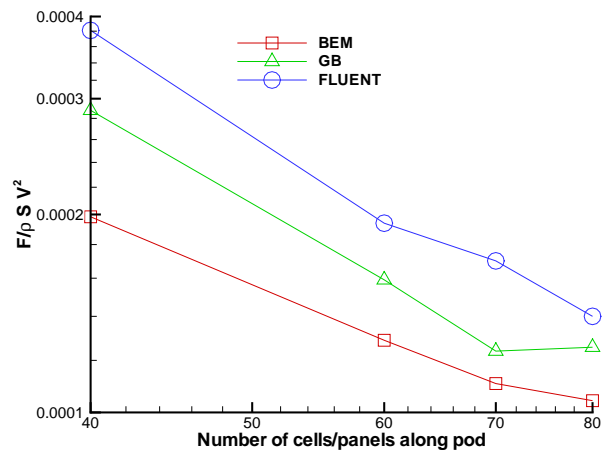


Figure 4.29: Convergence of forces with number of cells from all methods

#### **4.4 Comparisons among different methods**

The results from inviscid axisymmetric version of FLUENT are compared with the results from GBFLOW-3X and from the BEM solver. An unstructured grid with 140 nodes on the pod was used for FLUENT, a grid with  $140 \times 81$  nodes was used for GBFLOW and a grid with 80 panels on the pod was used in the BEM. The axial velocity and the pressures on the pod from FLUENT and the axisymmetric BEM solver are compared with those from the axisymmetric Euler solver in Figures 4.30 and 4.31, respectively. The pressure obtained from FLUENT has to be non-dimensionalized in a similar manner as done in GBFLOW as given by equation 3.6.

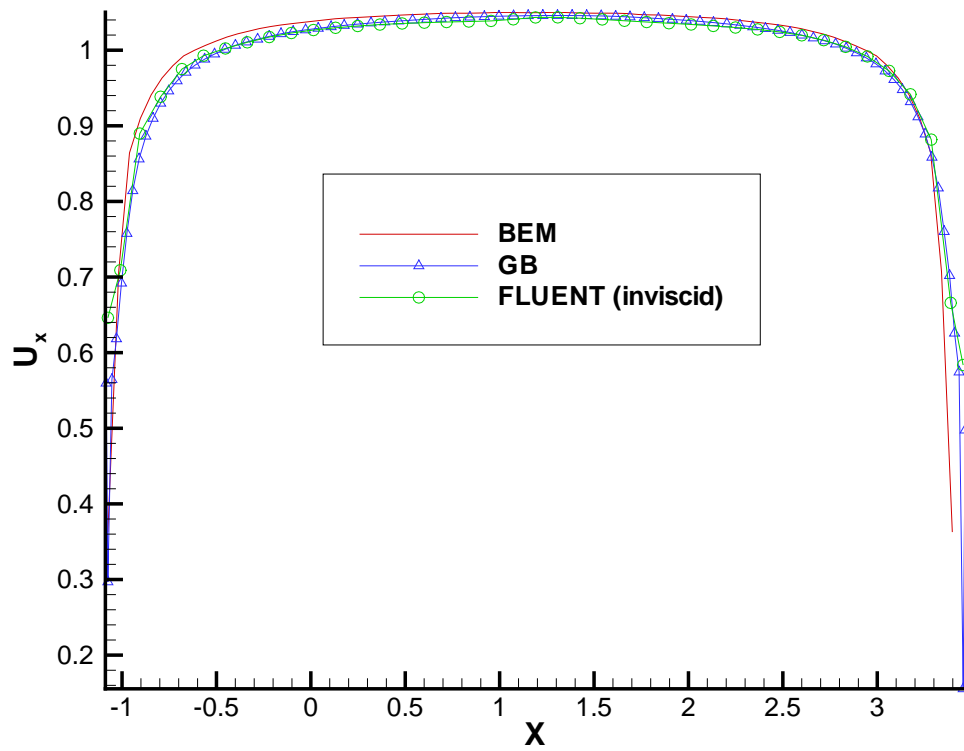


Figure 4.30: Non-dimensional axial velocity on the pod from axisymmetric inviscid FLUENT and BEM compared with GBFLOW-3X.

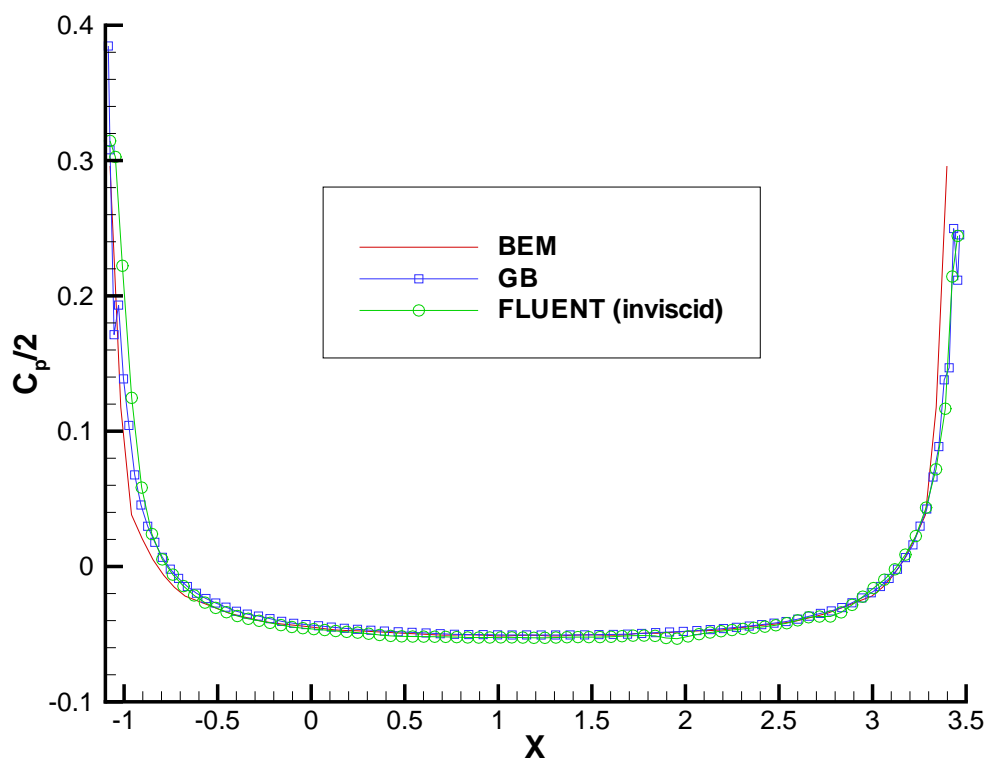


Figure 4.31: Non dimensional pressure on the pod from axisymmetric inviscid FLU-  
 ENT and BEM compared with GBFLOW-3X.

## Chapter 5

### Axisymmetric Pod and Propeller Interaction

In the previous Chapter, the flow around an axisymmetric pod was determined in the absence of a propeller. It is important to also know the flow, as well as the force on the pod, in the presence of a propeller. Moreover, the presence of the pod alters the inflow to the propeller and changes its performance characteristics. This Chapter focuses on the pod and propeller interaction. Coupling between the VLM and the FVM is carried out as detailed in Chapter 3. The axisymmetric version of FLUENT will only be used in this chapter, i.e. the effects of the strut will be ignored. However, the axisymmetric (GBFLOW-3X) as well as the 3-D (GBFLOW-3D) versions of the Euler solver will be used. In this way the effects of the strut on the overall flow can be estimated.

#### 5.1 Experiment

In order to validate the method thoroughly, it is essential to apply it to realistic geometries for which experimental data is available. One such experiment was done by [Szantyr 2001a]. A comparison with the experimental work has been presented in [Hsin et al. 2002], where the flow past a podded propulsor has been calculated

using both the boundary element method (applied to both the propeller and the pod) and a coupled viscous/potential flow solver.

### **5.1.1 Experimental Setup**

The experiments with the podded propulsor were performed in the cavitation tunnel of the Technical University of Gdansk. The podded propulsor is placed on a specially developed experimental stand. The stand is fitted with a tensometric dynamometer, enabling it to measure the longitudinal and the transverse components of force, and the moment component about the vertical axis. The forces and moments were measured in a coordinate system linked to the pod. The propulsor model is made of glass-reinforced plastic. The entire stand is mounted on top of the tunnel measuring section such that it could be rotated around the vertical axis. The forces were measured for a pulling propeller and for twin rotating propellers with the inflow at various yaw angles.

The principal dimensions of the pod used are presented below. More details on the exact geometry of the pod and the strut are given in Appendix A.

- Length of podded propulsor : 412 mm
- Maximum pod diameter: 74 mm
- Diameter at each propeller location: 64 mm
- Length of the strut: 140 mm
- Chord of the strut: 109 mm
- Maximum thickness of the strut: 47 mm

The propeller used were modified KCA 110, chosen from the series presented by [Gawn and Burrill 1957]. The propeller details are presented below.

- Propeller KCA 110 (modified) Gawn-Burrill series
- Propeller diameter for both propellers: 182 mm
- No. of blades: 3
- Blade area ratio of propeller  $A/A_0$ : 0.8
- Pitch of pulling propeller (radially constant)  $P/D$ : 0.8
- Pitch of pushing propeller (radially constant)  $P/D$ : 1.108

All dimensions are made non-dimensional with respect to the radius of the propeller. The detailed propeller geometries are given in Appendix A.

## 5.2 Propeller Configurations

The various podded propeller configurations that are solved using the present method are:

- Pull type: The propeller is located in front of the strut and can be viewed as if it is *pulling* the ship.
- Push type: The propeller is located aft of the strut, and it seems to *push* the ship.

- Twin rotating type : Two propellers rotating in the same direction, both placed either in front or aft of the strut, or, one propeller in front of the strut, and one aft of it.

### 5.3 Pull Type

In a pull type podded propeller, the propeller is placed in front of the strut, which joins the pod to the hull. The flow passes through the propeller before it passes over the strut. Since the propeller is in front of the strut, it seems as if the propeller is pulling the unit, and hence the name. Pull type podded propulsors are also called pre-swirl podded propulsors. In this case there is no strut, but the propeller location is similar to what it would be in the presence of a strut as shown in Figure 1.1.

#### 5.3.1 Coupling with GBFLOW-3X

Initially, GBFLOW-3X is used to solve the pod and propeller problem. The axial body force for  $J_s = 0.5$  and the effective wake location for a pull type configuration are shown in Figure 5.1. Note that all components of body force are considered in the calculations. A close-up of the body force is shown in Figure 5.2. It is obtained after integration of pressures on the propeller obtained from MPUF-3A as mentioned in Section 3.6.

Iterations are carried out between the methods (VLM and FVM) until a converged solution is obtained. Figures 5.3 and 5.4 show the converged velocity and pressure field contours around the pod, respectively. As can be seen the axial velocity increases as it passes the propeller and the flow seems to be *sucked* in. The

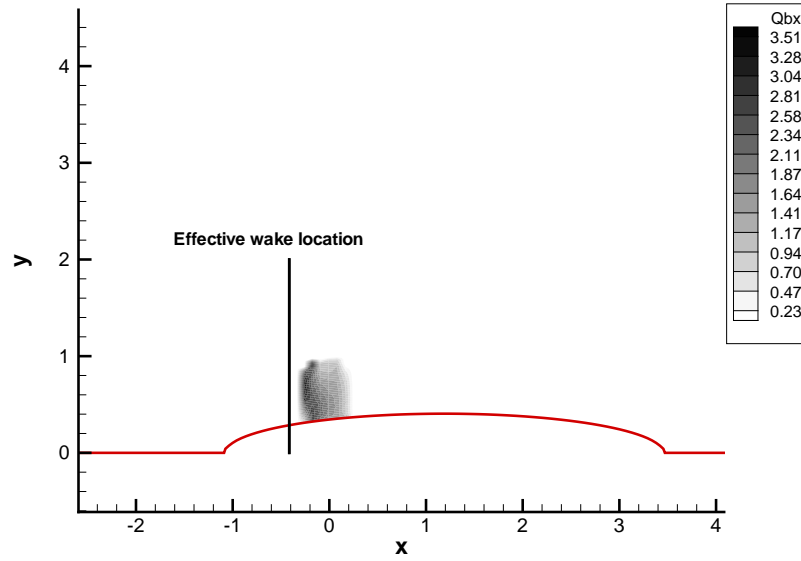


Figure 5.1: Axial body force contours in GBLFOW-3X domain obtained by integration of pressures on the propeller, for a pull type podded propulsor,  $J_s = 0.5$ .

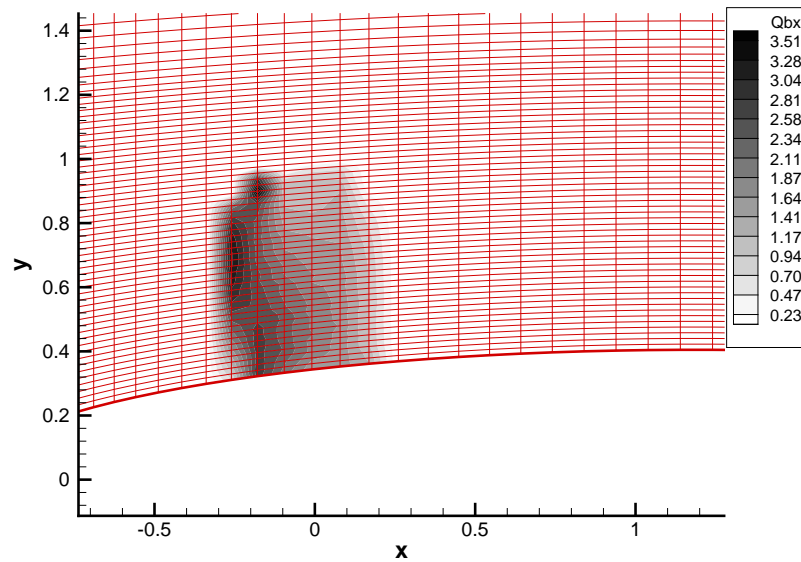


Figure 5.2: Close-up of axial body force contours in GBLFOW-3X for a pull type podded propulsor,  $J_s = 0.5$ .

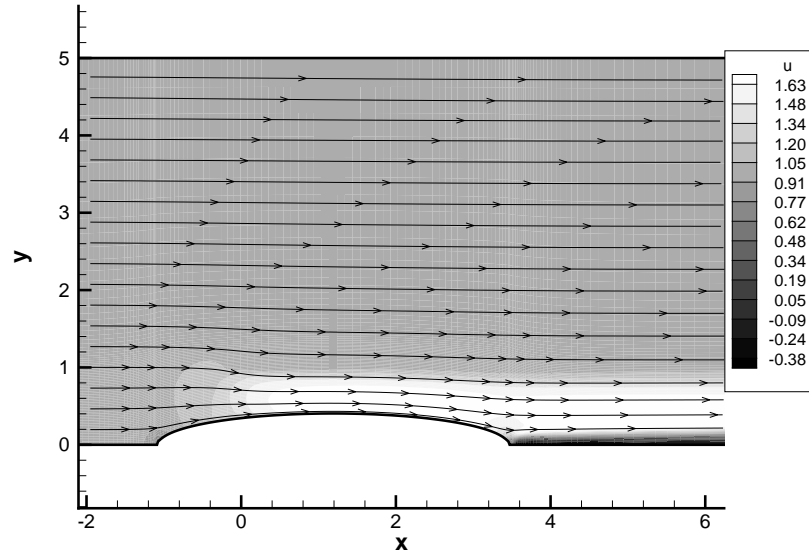


Figure 5.3: Axial velocity contour in GBFLOW-3X for pull type podded propulsor,  $J_s = 0.5$

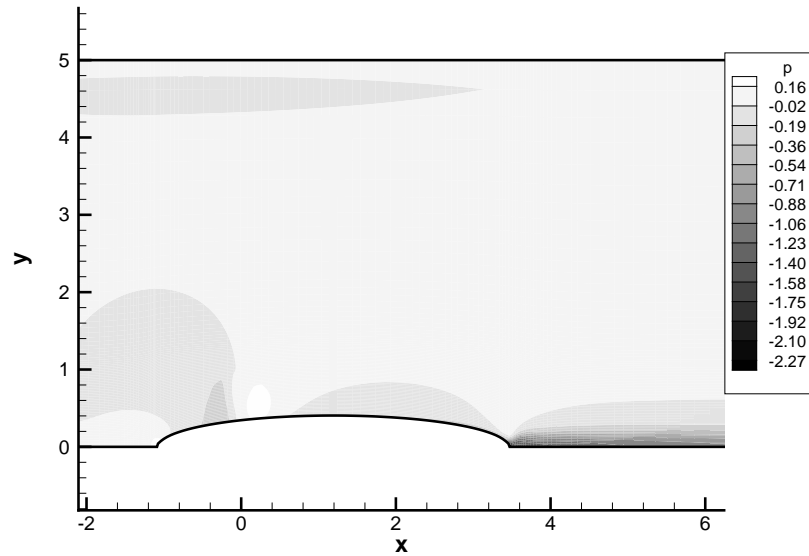


Figure 5.4: Pressure contour in GBFLOW-3X for pull type podded propulsor,  $J_s = 0.5$

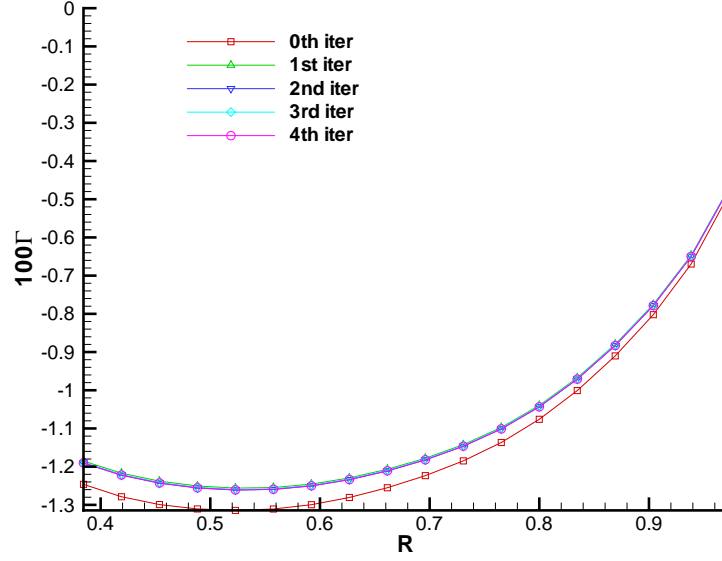


Figure 5.5: Convergence of circulation distribution with iterations for GBFLOW-3X coupled with MPUF-3A, for pull type podded propulsor,  $J_s = 0.5$

convergence of circulation distribution with iterations is shown in Figure 5.5. The circulation  $\Gamma$ , out of MPUF-3A is non-dimensionalised as,

$$\Gamma_{non-dim} = \frac{\Gamma \times 10^2}{2\pi R V_s} \quad (5.1)$$

where,  $\gamma$  is the strength of the bound vortices in MPUF-3A.

### *Force Calculations*

To get the total force on the pod, strut and the propeller system, the individual forces have to be added keeping in mind the direction of forces. The pictorial representation of the forces for  $0^\circ$  yaw angle is shown in Figure 5.6. The propeller thrust  $F_{prop}$  is given in the negative  $X$  direction while the force from GBFLOW and FLUENT is in the positive  $X$  direction. The frictional force acting on the pod (and strut in the 3-D

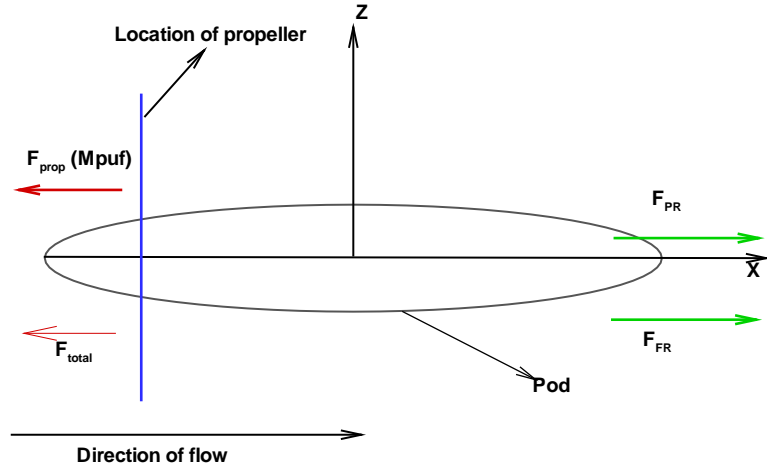


Figure 5.6: Pictorial representation of the direction of forces from MPUF-3A and GBFLOW/FLUENT, for  $0^0$  yaw angle.

case) calculated by equation 3.40 also acts in the positive  $X$  direction. The effect of the *tear force*,  $F_{NP}$ , or the force obtained on the strut and pod in the absence of propeller is considered in order to reduce the discretization error.

$$F_{Total} = F_{prop} - F_{PR} - F_{FR} - F_{NP} \quad (5.2)$$

where,  $F_{PR}$  is the non-dimensional pressure force from GBFLOW-3X/FLUENT in the presence of the propeller,  $F_{FR}$  is the non-dimensional frictional force obtained from equation 3.40, and  $F_{NP}$  is the non-dimensional *tear force*. The frictional force in case of FLUENT is given by the code itself and hence, the ITTC formula is not used. Also in case of viscous FLUENT no tear force correction is employed ( $F_{NP} = 0$ ).

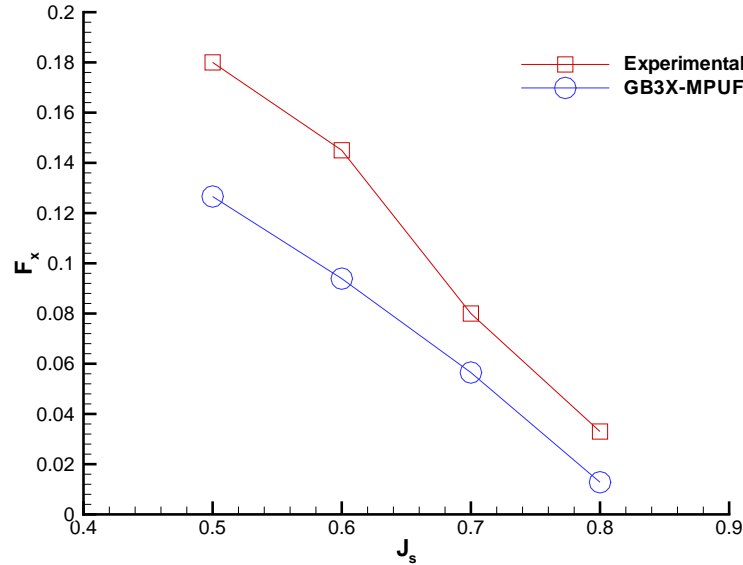


Figure 5.7: Comparison of axial force for a pulling propeller from the present method compared with the measurements of [Szantyr 2001a].

### Results

Runs for force calculations are carried out for four different advance ratios  $J_s$ . Figure 5.7 shows the comparison of the total axial force calculated for a pulling propeller from the numerical method (GBFLOW-3X/MPUF-3A) with that measured in the experiments performed by [Szantyr 2001a]. Comparison of these two is not entirely correct as the measurements are for a pod with a strut. The effects of the strut can also be included by coupling GBFLOW-3D with MPUF-3A and the results are shown in Figure 5.7. The break-up of non-dimensional forces from MPUF-3A and GBFLOW-3X are shown in Table 5.1. The forces from GBFLOW-3X are modified according to equation 3.39, so that they are non-dimensionalized the same way as the forces from MPUF-3A and from [Szantyr 2001a].

$J_s$	$F_{prop}$	$F_{PR} + F_{FR}$	$F_{NP}$	$F_{Total}$	$F_{Exp}$
0.5	0.1376	0.01103	0.00009	0.1266	0.18
0.6	0.1031	0.00933	0.00013	0.0939	0.145
0.7	0.0643	0.008	0.00017	0.0565	0.08
0.8	0.0200	0.0074	0.00022	0.0128	0.033

Table 5.1: Break-up of forces from MPUF-3A and GBFLOW-3X for pulling propeller for various advance ratios

### 5.3.2 Coupling with FLUENT

The inviscid and the viscous versions of FLUENT are coupled with MPUF-3A to solve the pull type podded propeller problem. Body forces are incorporated as sources via User Defined Functions (UDF). A structured grid is used for both inviscid and viscous runs. Unstructured grids were also used but they produced inaccurate results mainly owing to the interpolation of body forces over large cells. The distribution of body forces over a structured grid was found to be more accurate. Figures 5.8 and 5.9 show the axial body force distribution used over an unstructured and a structured grid, respectively. The axial body forces with varying grid sizes in FLUENT are also shown in Figure 5.10. Figure 5.11 shows the axial body force when a very fine grid is used in FLUENT. As can be seen the body force distribution is very close to that from GBFLOW-3X, shown in Figure 5.2 and hence, this verifies that the interpolation scheme reproduces the original body force distribution with sufficient grid resolution.

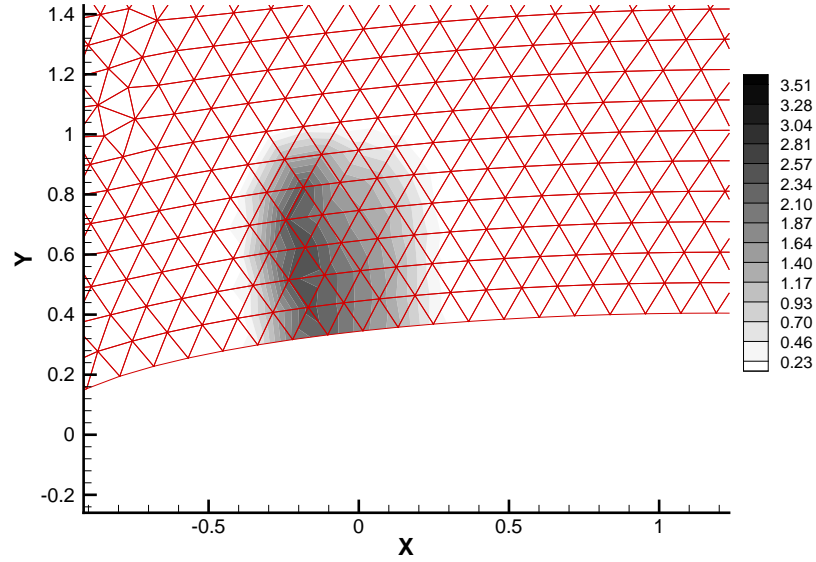


Figure 5.8: Axial body force distribution in FLUENT for an unstructured grid,  $J_s = 0.5$

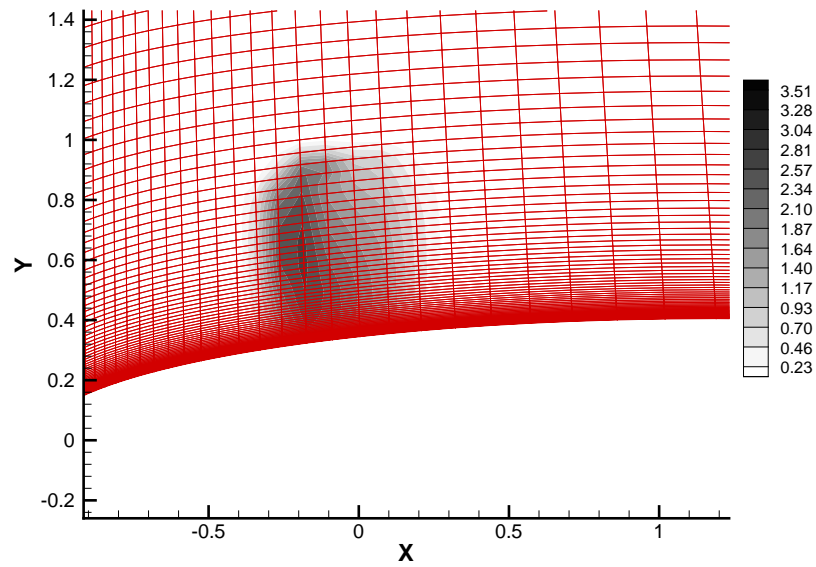


Figure 5.9: Axial body force distribution in FLUENT for a structured grid,  $J_s = 0.5$

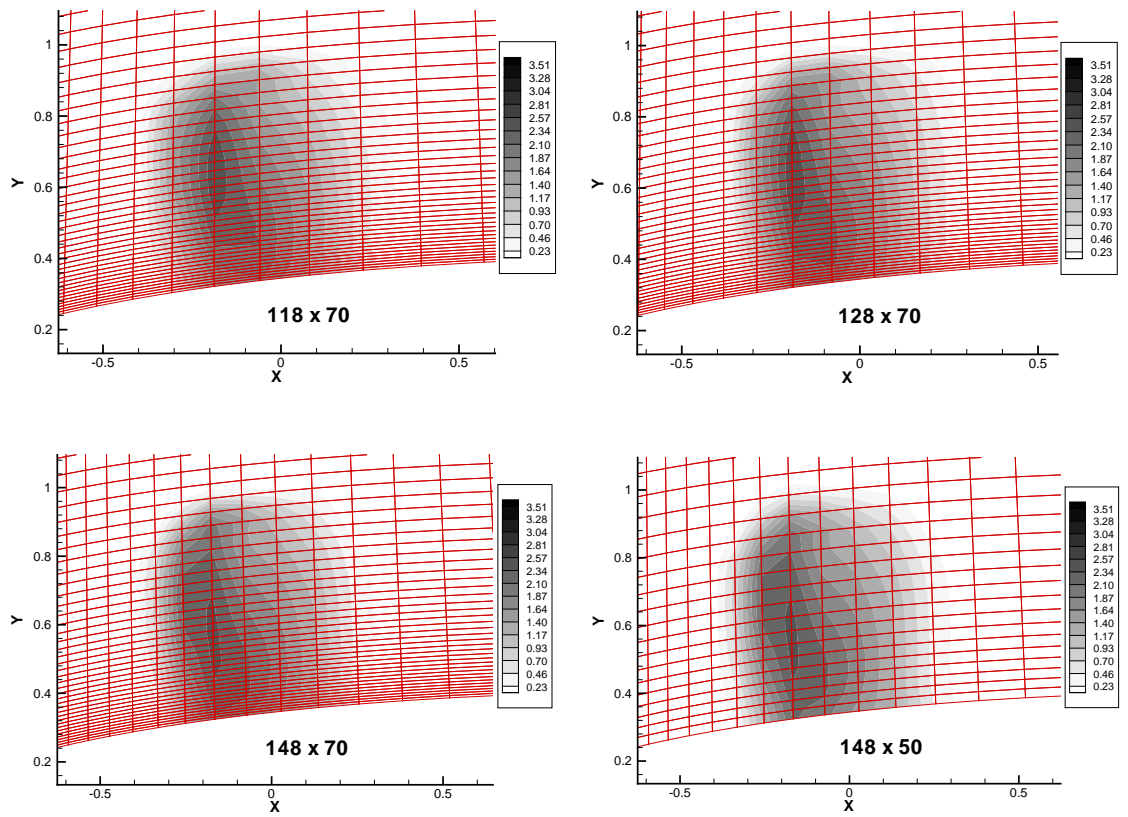


Figure 5.10: Convergence of axial body force distribution in FLUENT for varying grid sizes,  $J_s = 0.5$

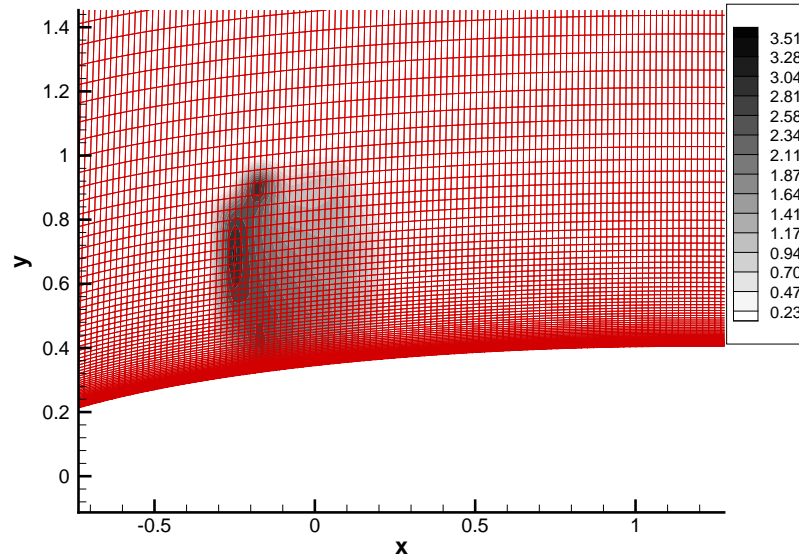


Figure 5.11: Axial body force distribution in FLUENT over a very fine structured grid,  $J_s = 0.5$

*Inviscid case*

Inviscid FLUENT is run with the same parameters as in Table 4.2 and with the source terms included. Figures 5.12 and 5.13 show the converged velocity and pressure field contour around the pod. The comparison of converged circulation distributions from GBFLOW-3X and FLUENT (inviscid) is shown in Figure 5.14. It can be seen that they agree very well. Figure 5.15 shows the comparison of the total axial force calculated for a pulling propeller from FLUENT and from GBFLOW-3X. The break-up of the forces is shown in Table 5.2.

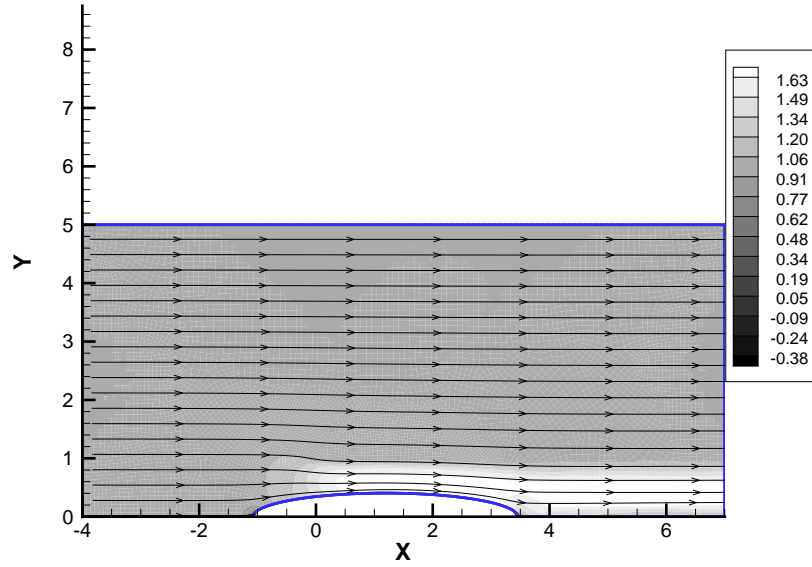


Figure 5.12: Axial velocity contour from inviscid FLUENT for pull type podded propulsor,  $J_s = 0.5$

$J_s$	$F_{prop}$	$F_{PR} + F_{FR}$	$F_{NP}$	$F_{Total}$
0.5	0.1370	0.0085	0.0004	0.1289
0.6	0.1028	0.0071	0.00054	0.0962
0.7	0.0740	0.0068	0.00074	0.0679
0.8	0.0200	0.0071	0.00096	0.0138

Table 5.2: Break-up of forces from MPUF-3A and FLUENT for pulling propeller for various advance ratios

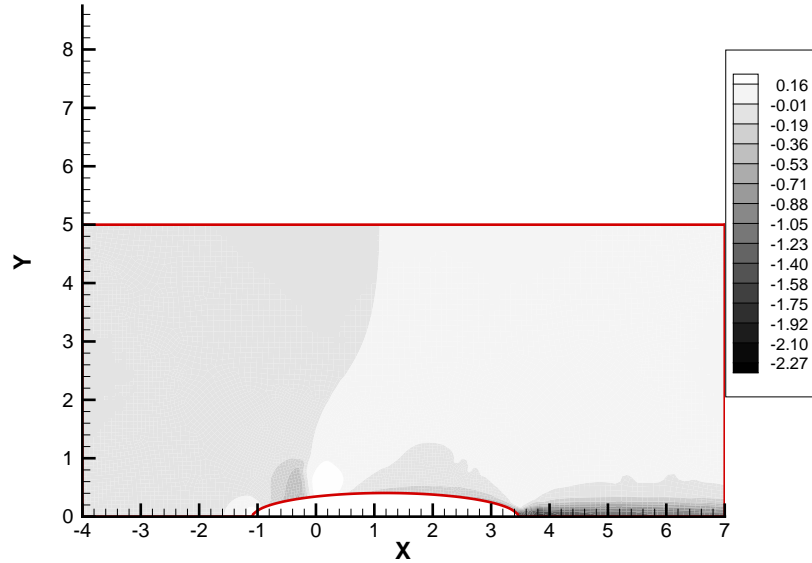


Figure 5.13: Pressure contour from inviscid FLUENT for pull type podded propulsor,  $J_s = 0.5$

#### *Viscous case*

Viscous FLUENT is run for parameters shown in Table 4.4 and Table 4.5. Reynolds scaling was carried out between the actual experimental data and FLUENT to keep the Reynolds number the same in both cases for different  $J_s$ . This was done by changing the dynamic viscosity  $\mu$  in FLUENT. Reynolds scaling has to be carried out since the dimensions of the pod in FLUENT are scaled by the radius of the propeller. When the effective wake is evaluated extrapolation of total velocity is carried out very near the pod instead of applying the exact velocity in the boundary layer. This was necessary to avoid unrealistically high loads at the propeller root. This is also consistent with the employed inviscid flow assumptions on the blades. Figures 5.16 and 5.17 show the converged velocity and pressure field contours around

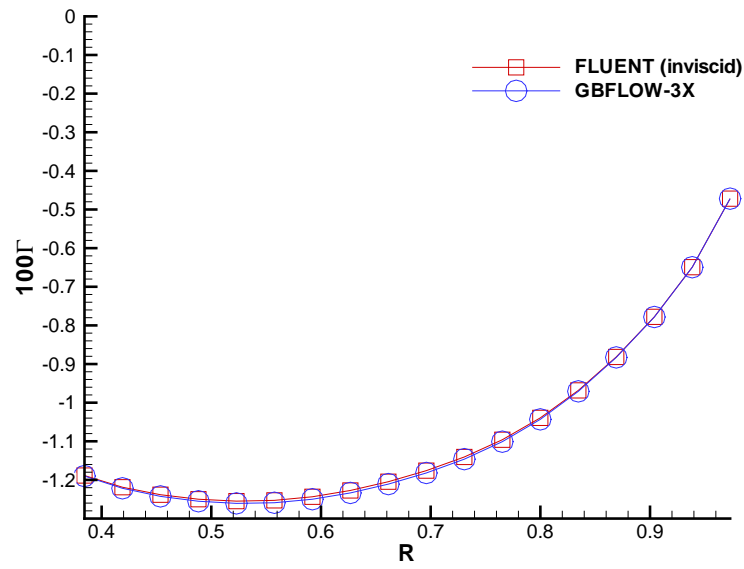


Figure 5.14: Comparison of converged circulation distributions predicted from GBFLOW-3X and FLUENT(inviscid) coupled with MPUF-3A, for pull type podded propulsor,  $J_s = 0.5$

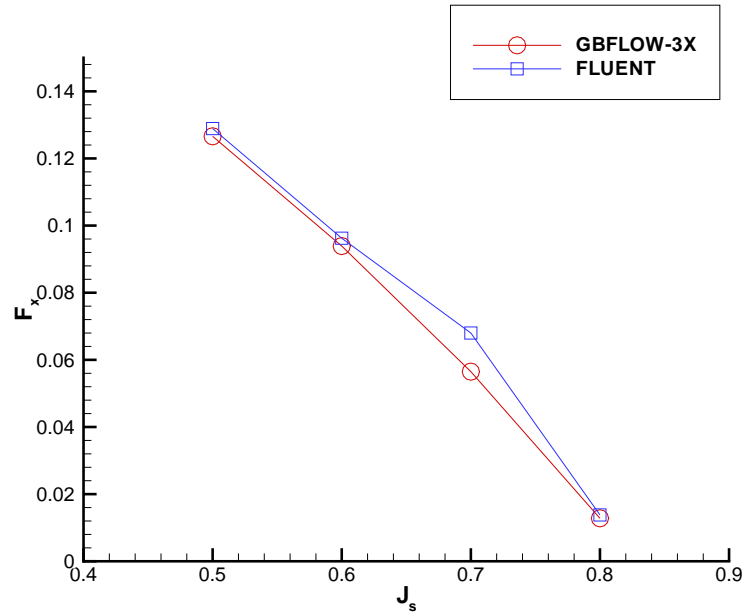


Figure 5.15: Comparison of axial force for a pulling propeller from FLUENT(inviscid) and GBFLOW-3X coupled with MPUF-3A.

the pod. The total axial velocity at the effective wake location from inviscid and viscous FLUENT is shown in Figure 5.18. As it can be seen there is only a small difference between the two, as expected, since the viscous flow effects are limited to a very thin boundary layer at the front part of the pod. The converged circulation distributions from FLUENT (viscous) and FLUENT (inviscid) are shown in Figure 5.19. As seen the circulations are very close to each other and this is consistent with the effective wake velocities, which are also found to be close to each other. The pressure distributions on the pod in the presence of the propeller as predicted from the three methods are shown in Figure 5.20. Figure 5.21 shows the comparison of the total axial force calculated for a pulling propeller from FLUENT inviscid and viscous and GBFLOW-3X. The break-up of the forces is shown in Table 5.3. GBFLOW-3D coupling was also included and this shows that the effect of strut is

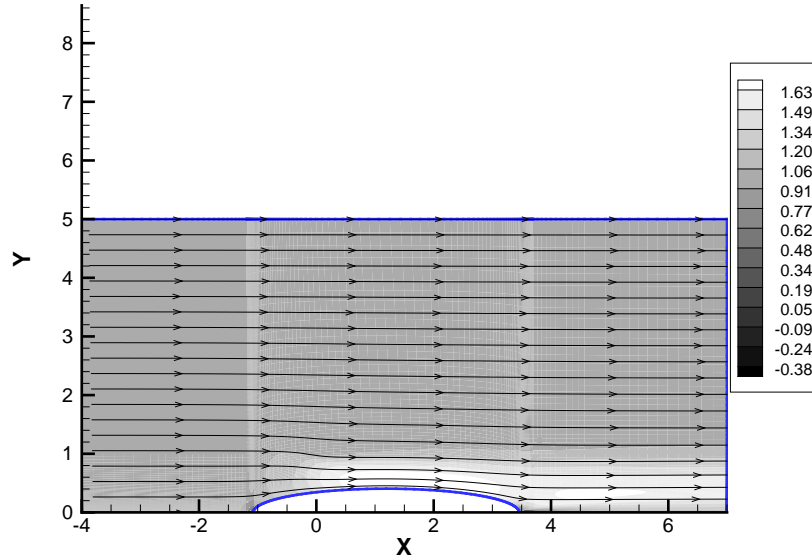


Figure 5.16: Axial velocity contour in viscous FLUENT for pull type podded propulsor,  $J_s = 0.5$ ,  $Re = 6.26 \times 10^5$

not very significant in this case. Also, including the effects of viscosity did not seem to improve the correlation with experiments. The reasons for the discrepancy of the results from all the methods with the measurements especially at lower  $J_s$  are not known at this point.

Similar to the results shown in Figure 4.25, runs were carried out using the RSM model in FLUENT and compared to those from the  $k - \epsilon$  model. The fore propeller was present and comparisons were carried out at the aft effective wake location between the axial and swirl velocities. Figures 5.22 and 5.23 show this comparison. It can be seen that the velocities from the RSM model are much closer (except very close to the pod) to the inviscid result, as expected, and hence this model is used for all future runs. The  $k - \epsilon$  model, as already discussed in Section 4.2.4, appears to over diffuse the flow vorticity.

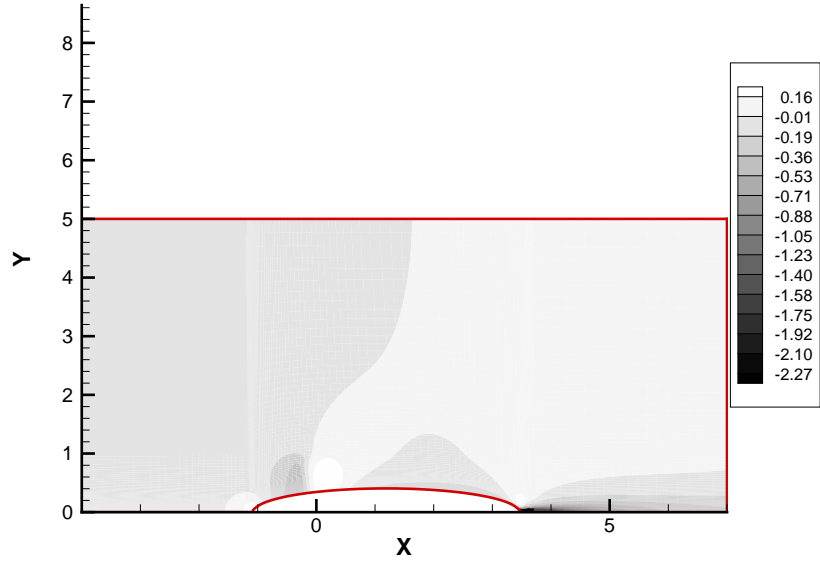


Figure 5.17: Pressure contour in viscous FLUENT for pull type podded propulsor,  $J_s = 0.5$ ,  $Re = 6.26 \times 10^5$

$J_s$	$F_{prop}$	$F_{PR} + F_{FR}$	$F_{Total}$
0.5	0.1371	0.0057	0.1314
0.6	0.1031	0.0061	0.0970
0.7	0.0646	0.0049	0.0597
0.8	0.0202	0.0051	0.0151

Table 5.3: Break-up of forces from MPUF-3A and viscous FLUENT for pulling propeller for various advance ratios

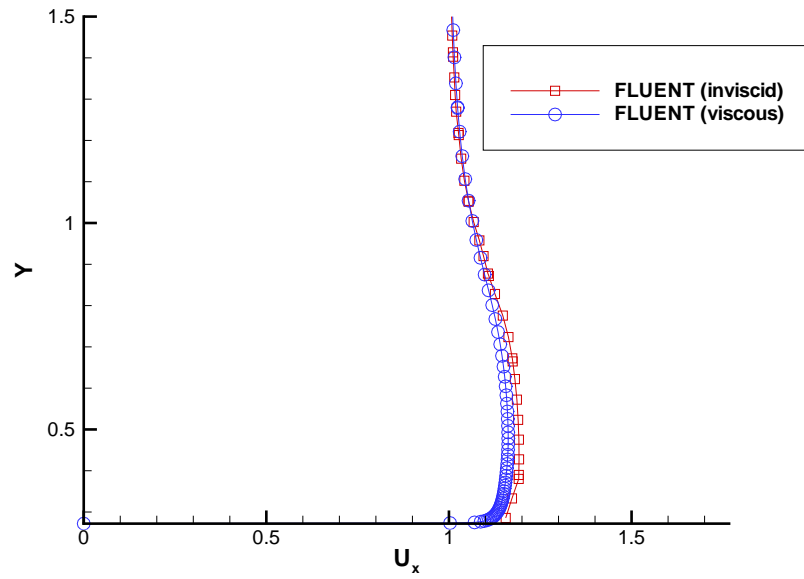


Figure 5.18: Total axial velocity at effective wake location for viscous and inviscid FLUENT coupled with MPUF-3A, for pull type podded propulsor,  $J_s = 0.5$ ,  $Re = 6.26 \times 10^5$

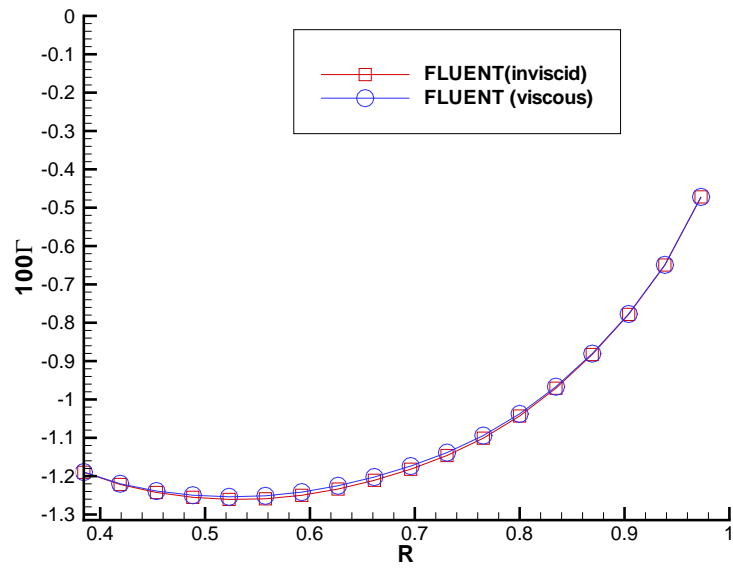


Figure 5.19: Converged circulation distributions predicted from FLUENT (viscous) and FLUENT(inviscid) coupled with MPUF-3A, for pull type podded propulsor,  $J_s = 0.5$ ,  $Re = 6.26 \times 10^5$

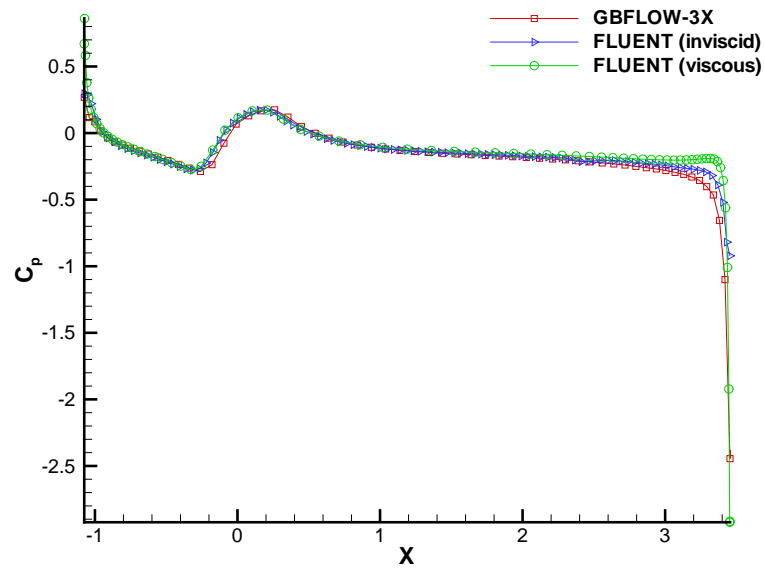


Figure 5.20: Converged pressure distributions predicted from GBFLOW-3X, FLUENT (viscous) and FLUENT(inviscid) coupled with MPUF-3A, for pull type podded propulsor,  $J_s = 0.5$ ,  $Re = 6.26 \times 10^5$

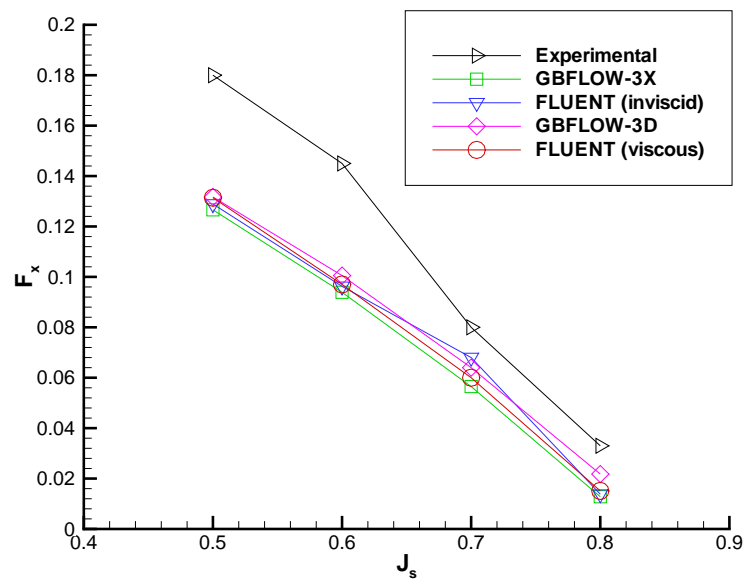


Figure 5.21: Comparison of axial force for a pulling propeller from FLU-ENT(inviscid & viscous) and GBFLOW coupled with MPUF-3A.

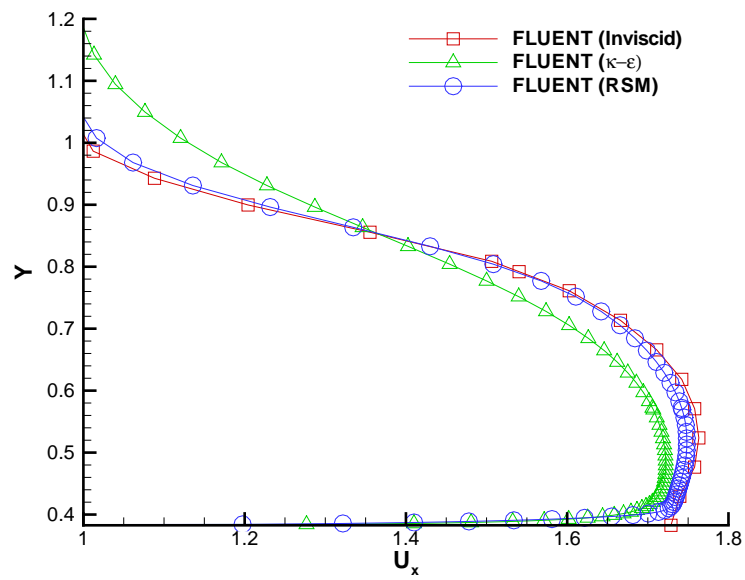


Figure 5.22: Comparison of axial velocity at aft effective wake location from inviscid,  $k - \epsilon$  and RSM models,  $J_s = 0.5Re = 6.26 \times 10^5$ .

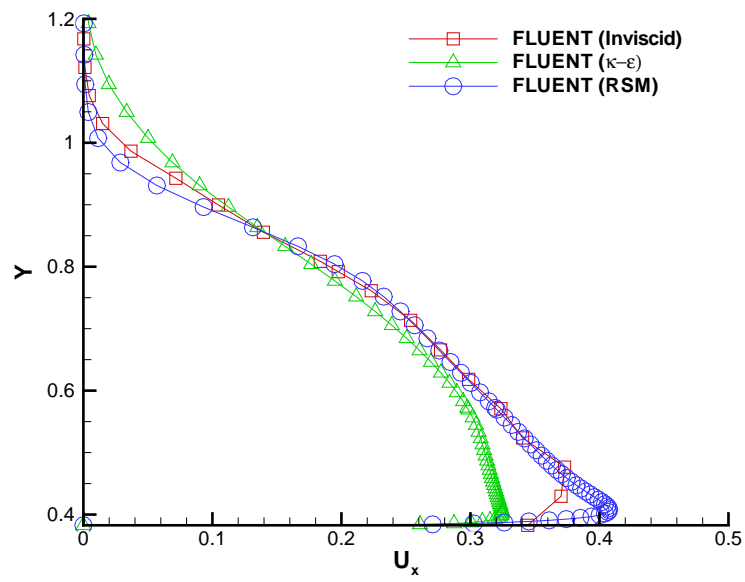


Figure 5.23: Comparison of swirl velocity at aft effective wake location from inviscid,  $k - \epsilon$  and RSM models,  $J_s = 0.5Re = 6.26 \times 10^5$ .

## 5.4 Push Type

In a push type podded propulsor the propeller is placed aft of the strut. The flow passes the strut before it reaches the propeller. Since we will use axisymmetric flow solvers the effect of the strut will be ignored. GBFLOW-3D has also been coupled with MPUF-3A and the effects of the strut on the solution can be estimated. The propeller and effective wake locations are as shown in Figure 4.23.

### 5.4.1 Coupling with GBFLOW-3X

Again, GBFLOW-3X is used initially to solve the push type unit in inviscid flow. The body force distribution for the push type propeller (for  $J_s = 0.5$ ) is shown in Figure 5.24. Figures 5.25 and 5.26 show the converged velocity and pressure field

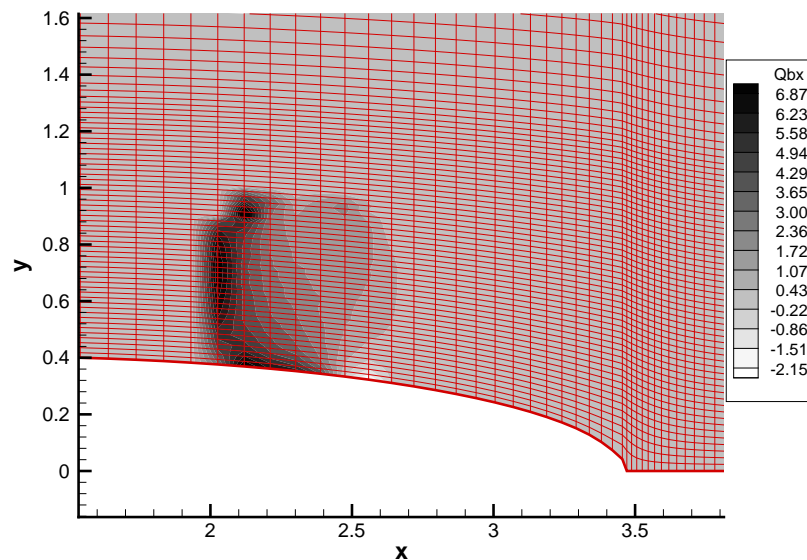


Figure 5.24: Body force contours in GBLFLOW-3X domain obtained by integration of pressures on the propeller, for a push type podded propulsor,  $J_s = 0.5$ .

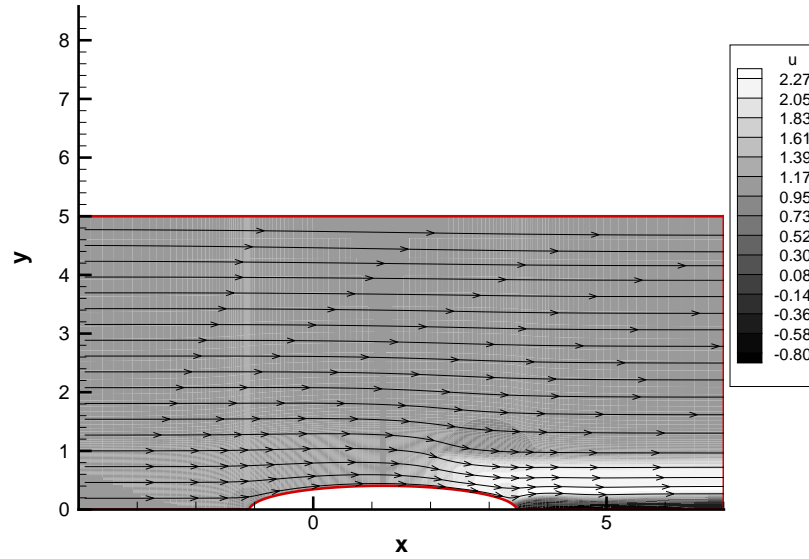


Figure 5.25: Axial velocity contour in GBFLOW-3X for push type podded propulsor,  $J_s = 0.5$

contour around the pod. The convergence of circulation distribution with iterations is shown in Figure 5.27. Force calculations are carried out for four different advance ratios. The break-up of the non-dimensional forces from MPUF-3A and GBFLOW-3X are shown in Table 5.4.

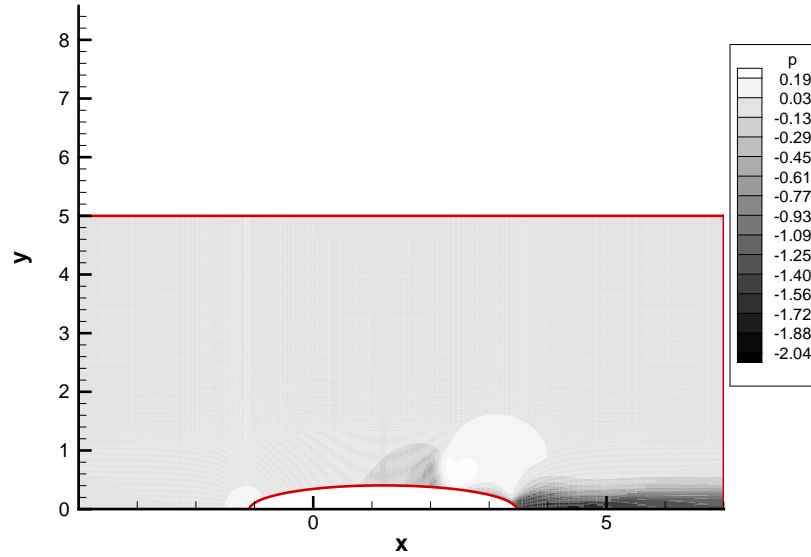


Figure 5.26: Pressure contour in GBFLOW-3X for push type podded propulsor,  $J_s = 0.5$

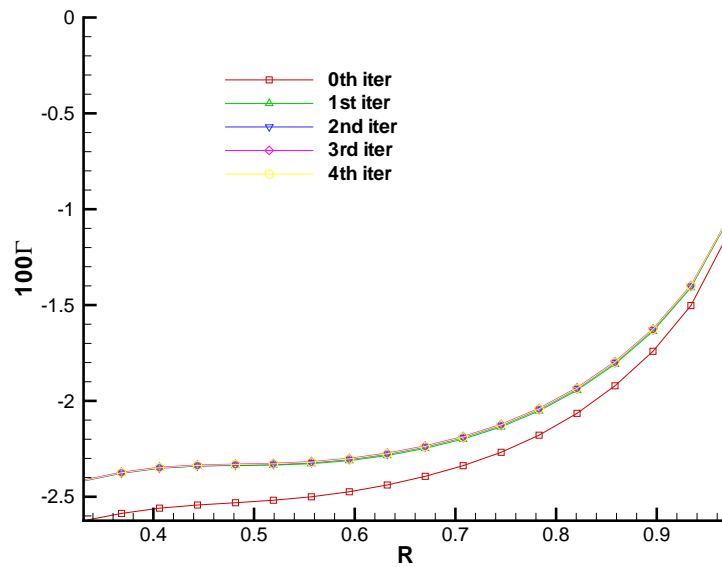


Figure 5.27: Convergence of circulation distribution with iterations for GBFLOW-3X for push type podded propulsor,  $J_s = 0.5$

$J_s$	$F_{prop}$	$F_{PR} + F_{FR}$	$F_{NP}$	$F_{Total}$
0.5	0.2806	0.0233	0.00009	0.2572
0.6	0.2471	0.0234	0.00013	0.2236
0.7	0.2090	0.0218	0.00017	0.1871
0.8	0.1662	0.0192	0.00022	0.1468

Table 5.4: Break-up of forces from MPUF-3A and GBFLOW-3X for pushing propeller for various advance ratios

### 5.4.2 Coupling with FLUENT

Both the inviscid and viscous versions of FLUENT are used to solve the coupled problem. Figures 5.28 and 5.29 show the body forces for the inviscid and viscous runs.

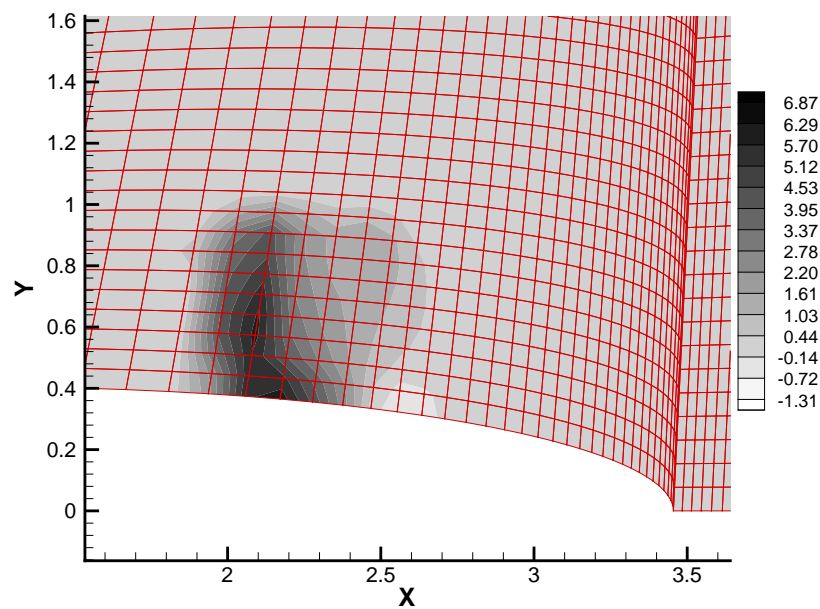


Figure 5.28: Body force distribution in FLUENT on the grid for inviscid case,  $J_s = 0.5$

#### *Inviscid case*

Inviscid FLUENT is run with the same parameters as for the pull type case. Figure 5.30 shows the axial velocity contour for this case. Next, comparisons are carried out between GBFLOW-3X and FLUENT inviscid. Figure 5.31 shows the comparison of converged effective axial velocity at the effective wake location. As is seen

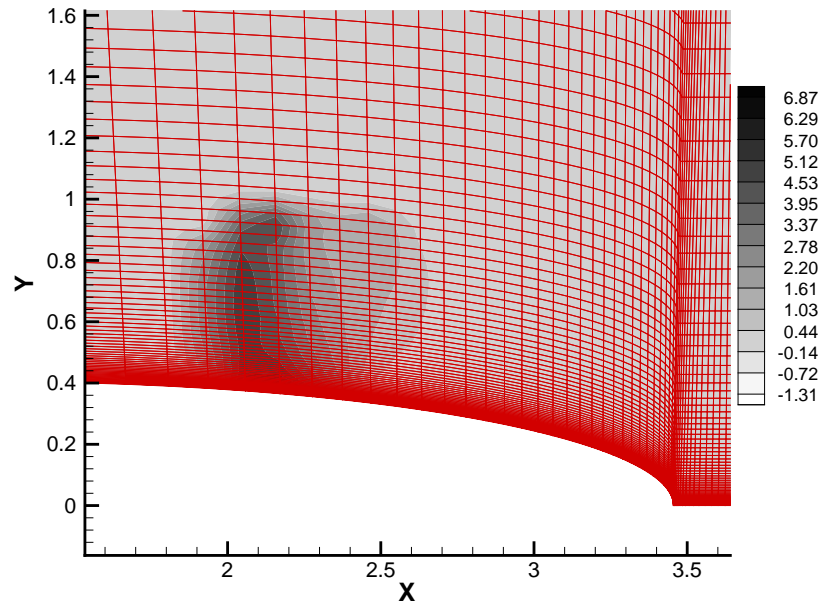


Figure 5.29: Body force distribution in FLUENT on the grid for viscous case,  $J_s = 0.5$ ,  $Re = 6.26 \times 10^5$

the effective axial velocity from both methods compare very well with each other. The comparison of converged circulation distribution between GBFLOW-3X and FLUENT (inviscid) is shown in Figure 5.32. Figure 5.33 shows the comparison of the total axial force calculated for a pulling propeller from FLUENT (inviscid) and from GBFLOW-3X. The break-up of the forces is shown in Table 5.5. We see that results from GBFLOW-3X and the inviscid version of FLUENT are very close to each other and this is a very strong indication that both methods are implemented correctly. Nevertheless, a systematic grid dependence study is needed to verify the two approaches fully.

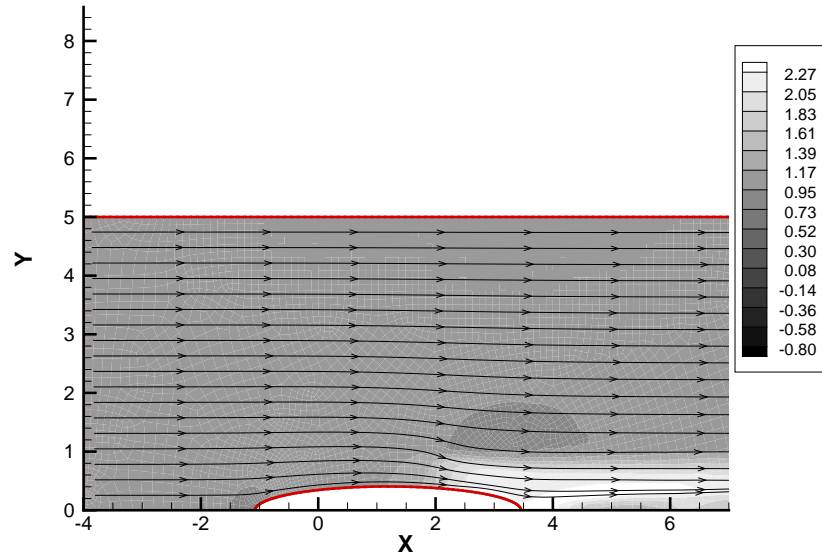


Figure 5.30: Axial velocity contour in inviscid FLUENT for push type podded propulsor,  $J_s = 0.5$

$J_s$	$F_{prop}$	$F_{PR} + F_{FR}$	$F_{NP}$	$F_{Total}$
0.5	0.279	0.024	0.0004	0.2546
0.6	0.2474	0.021	0.00054	0.2259
0.7	0.2106	0.018	0.00074	0.1918
0.8	0.1693	0.015	0.00096	0.1533

Table 5.5: Break-up of forces from MPUF-3A and inviscid FLUENT for pushing propeller for various advance ratios

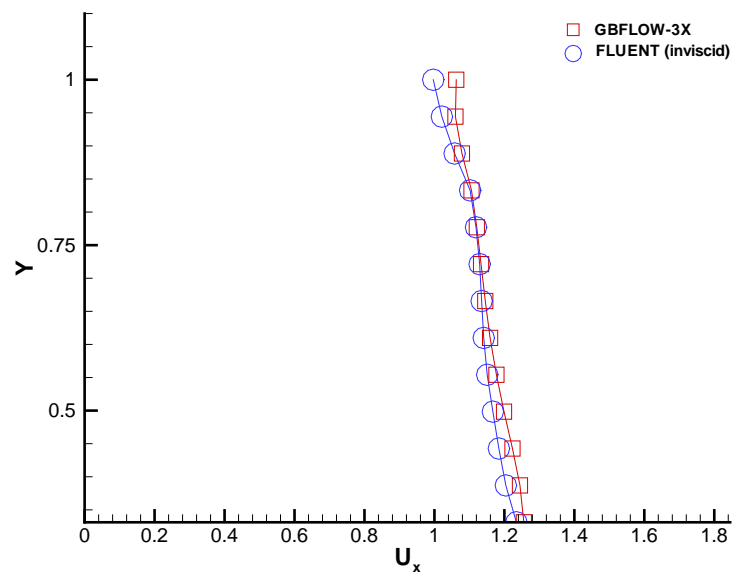


Figure 5.31: Comparison of effective axial velocity between GBFLOW-3X and FLUENT (inviscid) coupled with MPUF-3A, for a push type unit,  $J_s = 0.5$ .

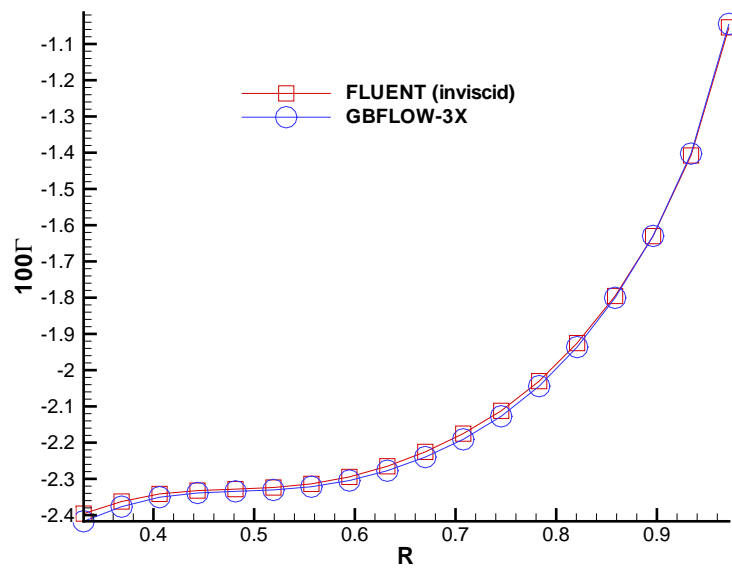


Figure 5.32: Converged circulation distributions predicted from GBFLOW-3X and FLUENT(inviscid) coupled with MPUF-3A, for push type podded propulsor,  $J_s = 0.5$

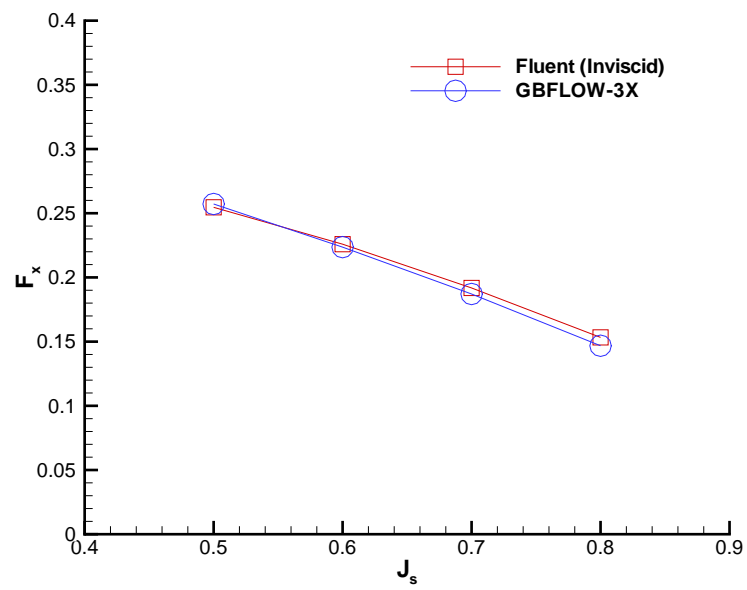


Figure 5.33: Axial force for a pushing propeller predicted from FLUENT (inviscid) and GBFLOW-3X coupled with MPUF-3A.

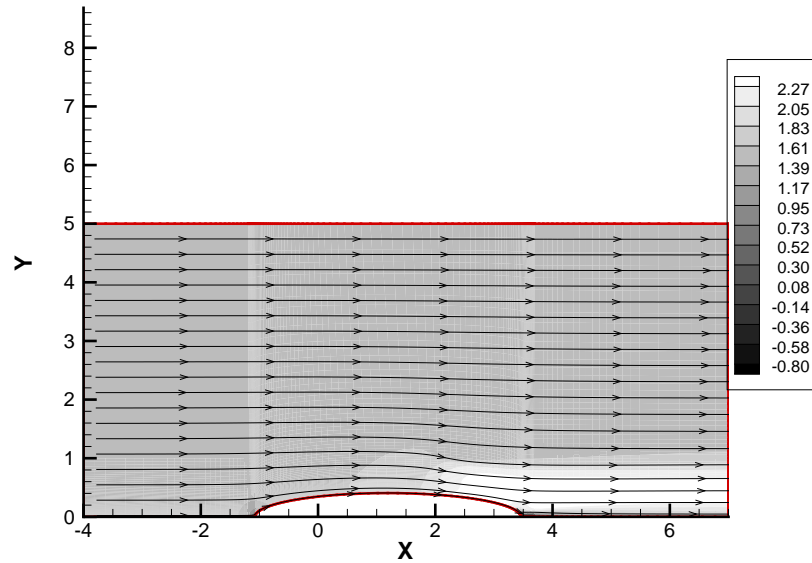


Figure 5.34: Axial velocity contours predicted by viscous FLUENT for push type podded propulsor,  $J_s = 0.5$ ,  $Re = 6.26 \times 10^5$

#### *Viscous Case*

Viscous FLUENT is run for the same parameters as for the pull type case except now by using the RSM turbulence model. Figure 5.34 shows the axial velocity contour from the viscous solver. The total axial velocity at the effective wake plane location from inviscid and viscous FLUENT is compared next in Figure 5.35. The effective wakes are also compared in Figure 5.36. It can be seen that the velocity in the viscous case is lower due to onset of viscous effects. The circulation distributions obtained from inviscid and viscous FLUENT are compared in Figure 5.37. Figure 5.39 shows the comparison of the total axial force calculated for a pulling propeller from FLUENT (inviscid and viscous) and from GBFLOW-3X. The break-up of the forces is shown in Table 5.6. The lower effective velocity in the viscous case results

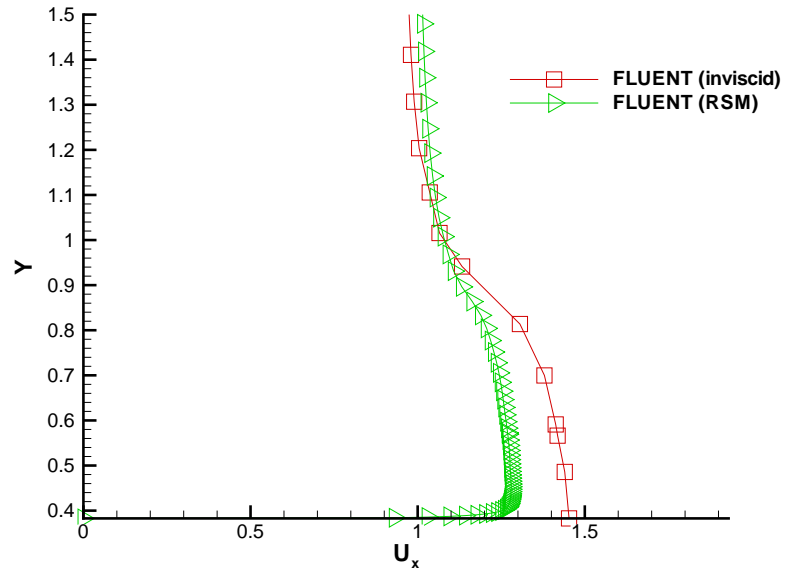


Figure 5.35: Comparison of total axial velocity at effective wake plane location from inviscid and viscous FLUENT coupled with MPUF-3A,  $J_s = 0.5$ ,  $Re = 6.26 \times 10^5$

in higher circulation and hence higher forces. Figure 5.38 also shows the pressure distribution along the body obtained from the different methods. As expected the GBFLOW-3X and inviscid FLUENT solutions are close to each other. In the case of the presence of the strut the flow will change significantly for the push type unit. The velocity from the viscous solver should be considerably lower at the top of the propeller disk due to the viscous losses at the strut. Comparisons are not carried out with experiments as no measurements were available for this type of propulsor.

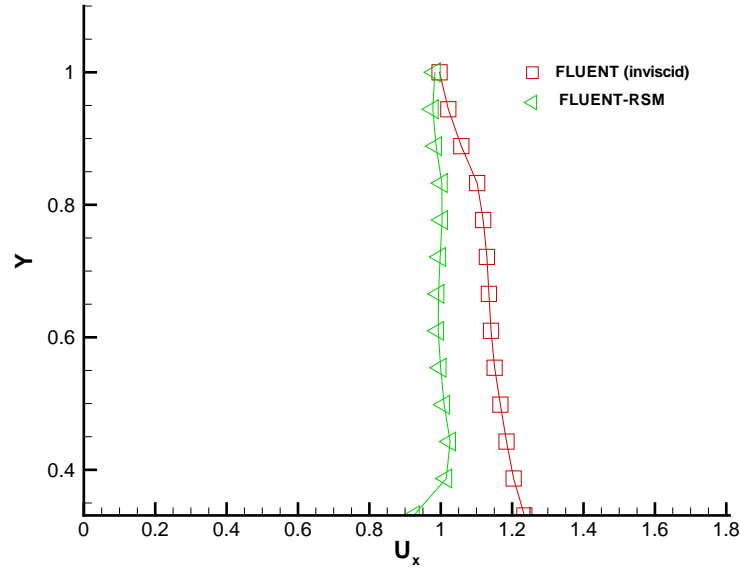


Figure 5.36: Comparison of effective velocity at effective wake plane location from inviscid and viscous FLUENT coupled with MPUF-3A,  $J_s = 0.5$ ,  $Re = 6.26 \times 10^5$

$J_s$	$F_{prop}$	$F_{PR} + F_{FR}$	$F_{Total}$
0.5	0.298	0.0255	0.2725
0.6	0.278	0.020	0.258
0.7	0.244	0.020	0.224
0.8	0.20	0.025	0.175

Table 5.6: Break-up of forces from MPUF-3A and viscous FLUENT for pushing propeller for various advance ratios

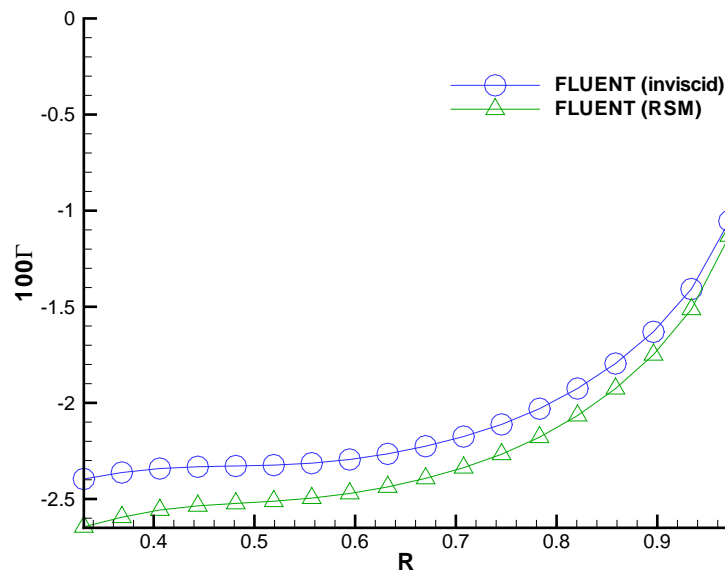


Figure 5.37: Comparison of converged circulation from inviscid and viscous FLU-ENT coupled with MPUF-3A,  $J_s = 0.5$ ,  $Re = 6.26 \times 10^5$

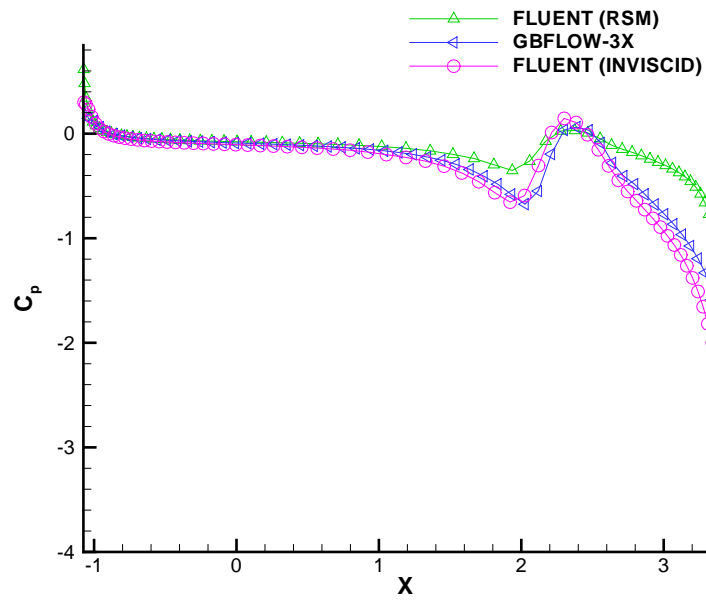


Figure 5.38: Comparison of pressure distributions along the body for a pushing propeller from FLUENT(inviscid & viscous) and GBFLOW-3X coupled with MPUF-3A.

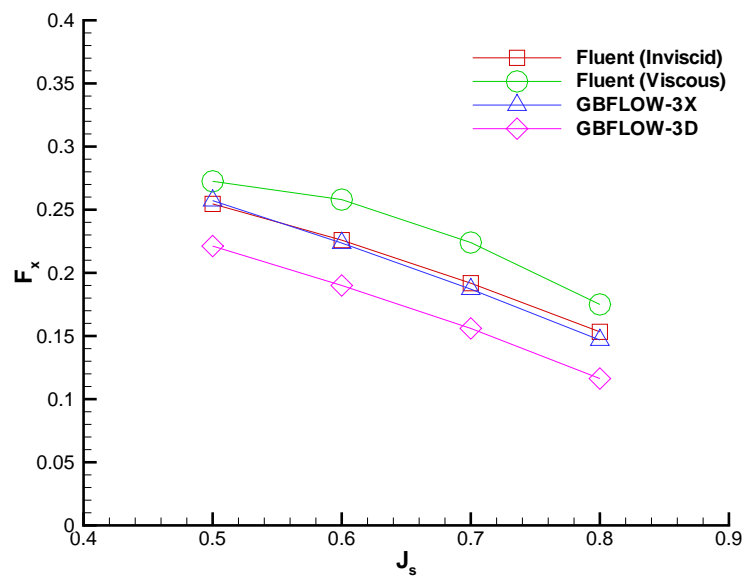


Figure 5.39: Comparison of axial force for a pushing propeller from FLUENT(inviscid & viscous) and GBFLOW-3X coupled with MPUF-3A.

## 5.5 Twin type

In this case there are two propellers each at the fore and aft propeller location. The flow to the aft propeller is modified by the fore propeller. In this case both propellers are left handed. So unlike the case of a contra-rotating system there is no cancellation of swirl downstream of the aft propeller.

### 5.5.1 Coupling of GBFLOW-3X

GBFLOW-3X is coupled with MPUF-3A to solve the twin type propulsor problem. The interaction between both the propellers and the pod is taken into account by solving each propeller individually and by including the body forces from both in GBFLOW-3X. Figures 5.40 and 5.41 show the axial velocity and the pressure contours around the pod in presence of the propellers. The convergence of circulation distribution for fore and aft propeller are shown in Figures 5.42 and 5.43. Runs for force calculations are carried out for four different advance ratios  $J_s$ . Figure 5.44 shows the comparison of the total axial force calculated for a twin type propeller unit using the numerical method, with that measured in the experiments performed by [Szantyr 2001a]. Comparison of these two is not entirely correct as explained for the pull type case. The break-up of non-dimensional forces from MPUF-3A and GBFLOW-3X are shown in Table 5.7.

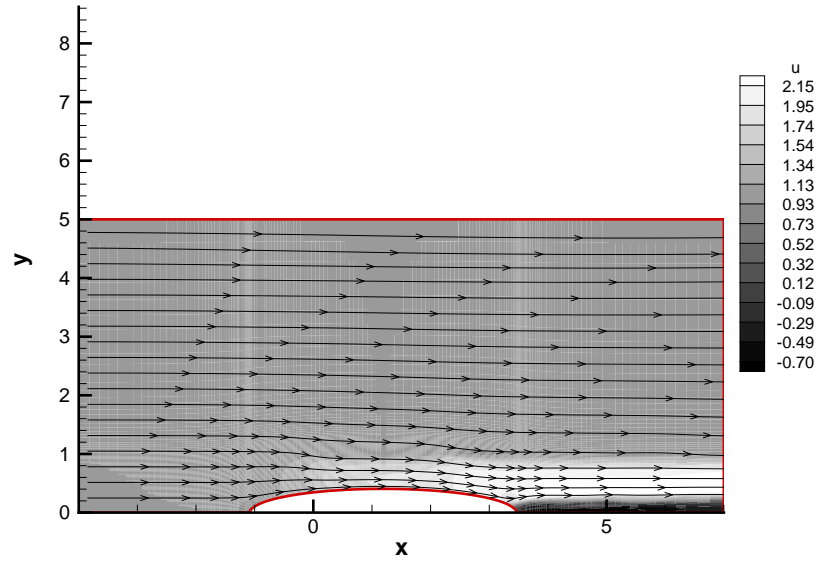


Figure 5.40: Axial velocity contour in GBFLOW-3X for twin type podded propulsor,  $J_s = 0.5$

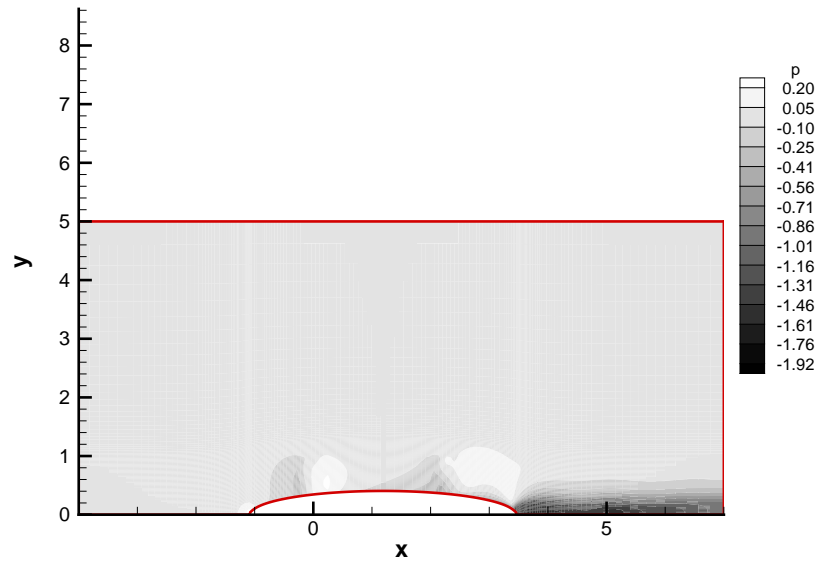


Figure 5.41: Pressure contour in GBFLOW-3X for twin type podded propulsor,  $J_s = 0.5$

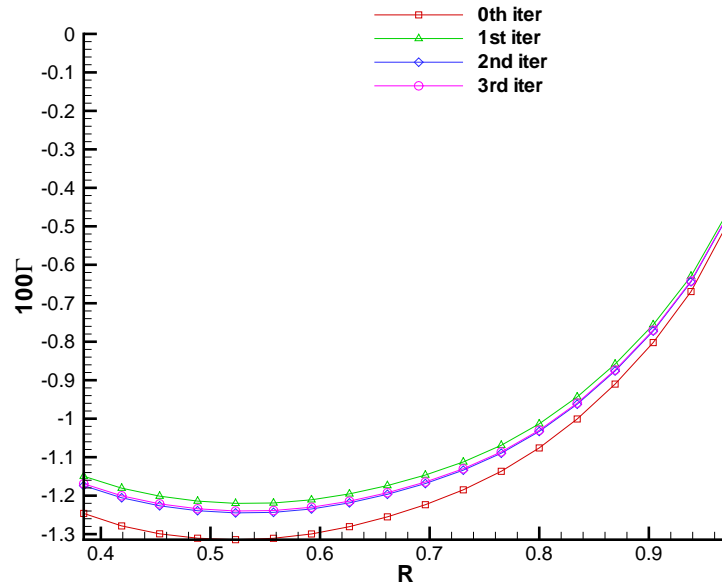


Figure 5.42: Convergence of circulation distribution with iterations for fore propeller from GBFLOW-3X for twin type podded propulsor,  $J_s = 0.5$

$J_s$	$F_{propf}$	$F_{propa}$	$F_{PR} + F_{FR}$	$F_{NP}$	$F_{Total}$
0.5	0.1355	0.1477	0.02628	0.00009	0.257
0.6	0.1009	0.1428	0.02522	0.00013	0.2186
0.7	0.0618	0.1394	0.0242	0.00017	0.1764
0.8	0.0161	0.1400	0.0231	0.00022	0.1332

Table 5.7: Break-up of forces from MPUF-3A and GBFLOW-3X for twin propeller unit for various advance ratios

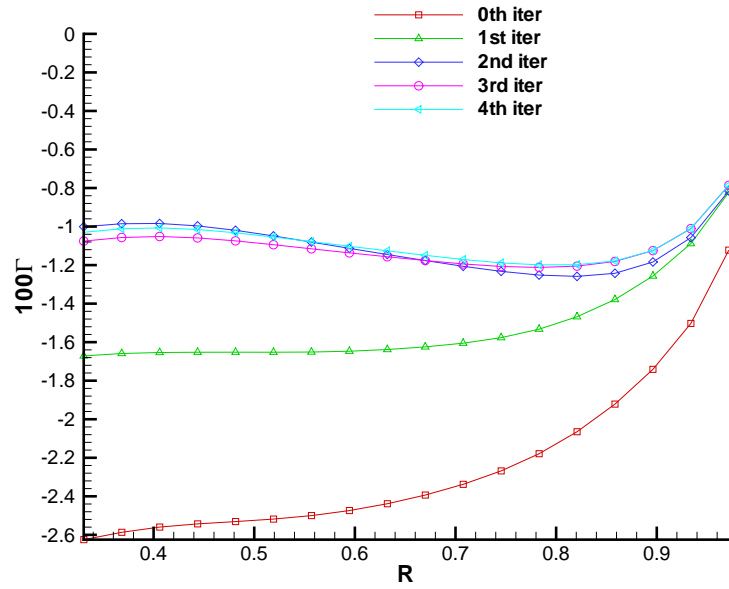


Figure 5.43: Convergence of circulation distribution with iterations for aft propeller from GBFLOW-3X for twin type podded propulsor,  $J_s = 0.5$

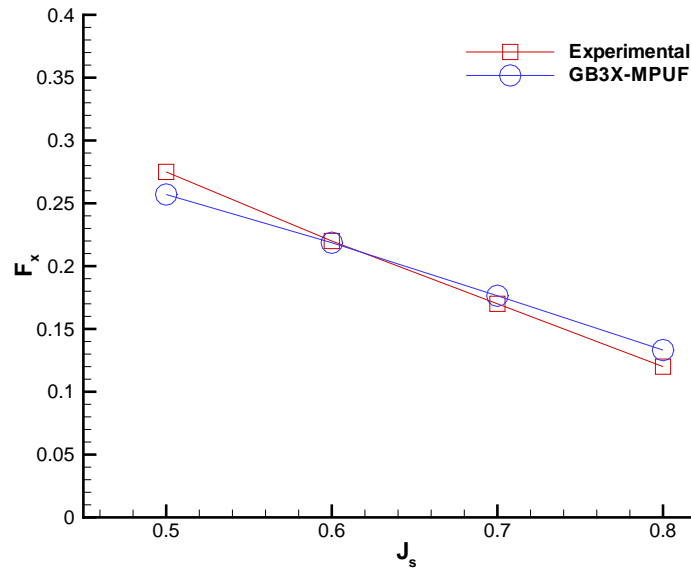


Figure 5.44: Comparison of axial force for a twin type propeller unit from present method compared with experiments of [Szantyr 2001a].

### 5.5.2 Coupling with FLUENT

FLUENT viscous is run for the twin case to study the effects of viscosity. The RSM model is used for viscous runs. Figures 5.45 and 5.46 show the axial velocity and the pressure contours around the pod in presence of the propellers. The effective

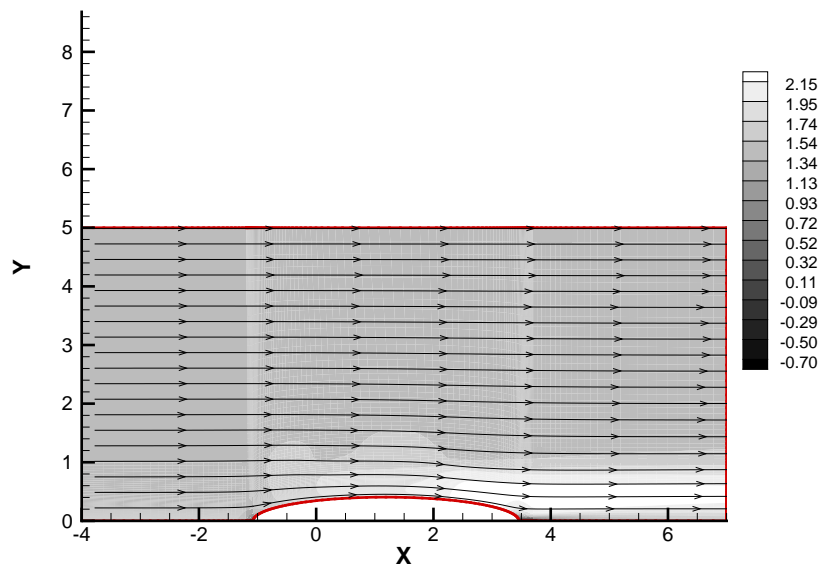


Figure 5.45: Axial velocity contour from viscous FLUENT for twin type podded propulsor,  $J_s = 0.5$ ,  $Re = 6.26 \times 10^5$

wakes from GBFLOW-3X and viscous FLUENT are compared for the fore and aft propeller. Figures 5.47 and 5.48 show the comparison. It is seen that there is not much difference for the fore propeller. This is because the fore propeller is very near to the leading edge of the pod and hence, the viscous effects are not significant. The swirl velocities at the aft effective wake location are also compared in Figure 5.49. The converged circulation distributions for both propellers as predicted from GBFLOW-3X and viscous FLUENT are shown in Figures 5.50 and 5.51. The dif-

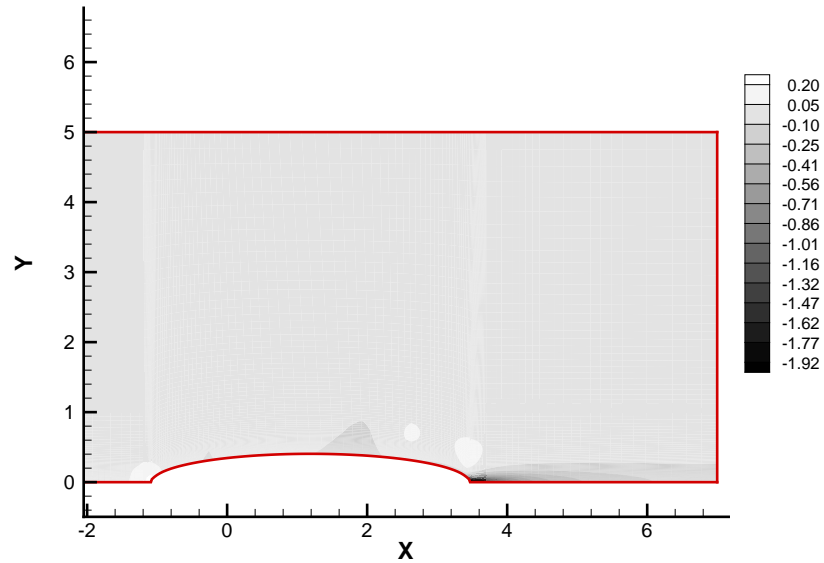


Figure 5.46: Pressure contour from viscous FLUENT for twin type podded propulsor,  $J_s = 0.5$ ,  $Re = 6.26 \times 10^5$

ference in the circulation distribution for the aft propeller can be attributed to the difference in the swirl velocity component.

The break-up of non-dimensional forces from MPUF-3A and viscous FLUENT is shown in Table 5.8. Figure 5.53 shows the comparison of the total axial force between GBFLOW-3X and viscous FLUENT. Also, the results from GBFLOW-3D are somewhat higher. This is mainly because the flow to the aft propeller is changed due to the presence of the strut, which reduces the effective velocity resulting in higher circulation. Figure 5.52 shows the pressure distribution along the body obtained from the different methods.

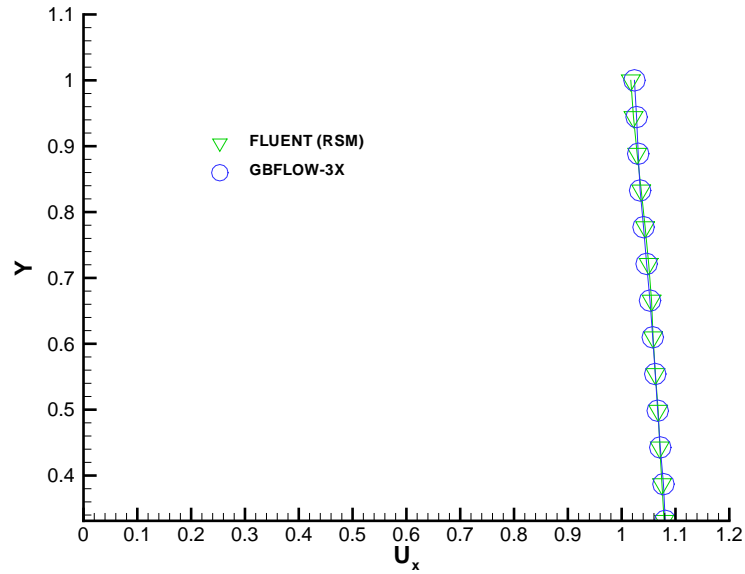


Figure 5.47: Comparison of effective velocity for fore propeller between GBFLOW-3X and FLUENT (viscous) coupled with MPUF-3A, for a twin type unit,  $J_s = 0.5$ ,  $Re = 6.26 \times 10^5$ .

$J_s$	$F_{propf}$	$F_{propa}$	$F_{PR} + F_{FR}$	$F_{Total}$
0.5	0.1349	0.1642	0.01122	0.2878
0.6	0.1004	0.1571	0.02236	0.2351
0.7	0.0616	0.1502	0.0195	0.1923
0.8	0.0164	0.1438	0.0177	0.1425

Table 5.8: Break-up of forces from MPUF-3A and FLUENT (RSM) for twin propeller unit for various advance ratios

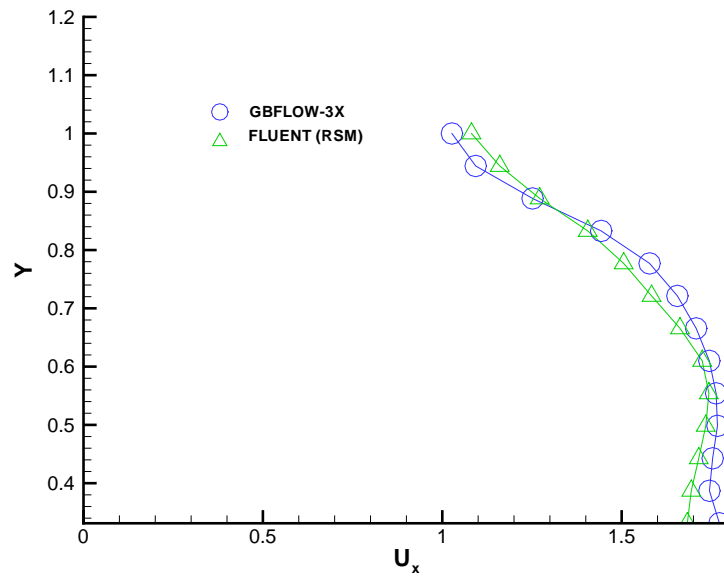


Figure 5.48: Comparison of effective axial velocity for aft propeller predicted from GBFLOW-3X and FLUENT (viscous) coupled with MPUF-3A, for a twin type unit,  $J_s = 0.5$ ,  $Re = 6.26 \times 10^5$ .

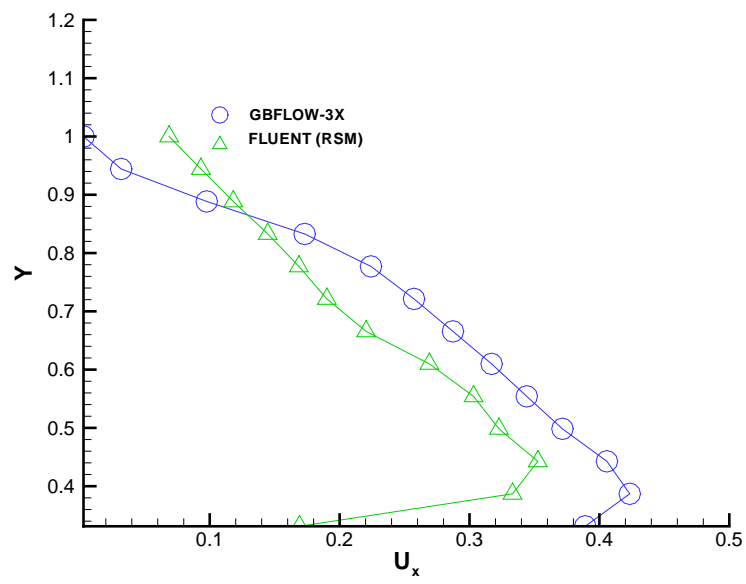


Figure 5.49: Comparison of effective swirl velocity for aft propeller predicted from GBFLOW-3X and FLUENT (viscous) coupled with MPUF-3A, for a twin type unit,  $J_s = 0.5$ ,  $Re = 6.26 \times 10^5$ .

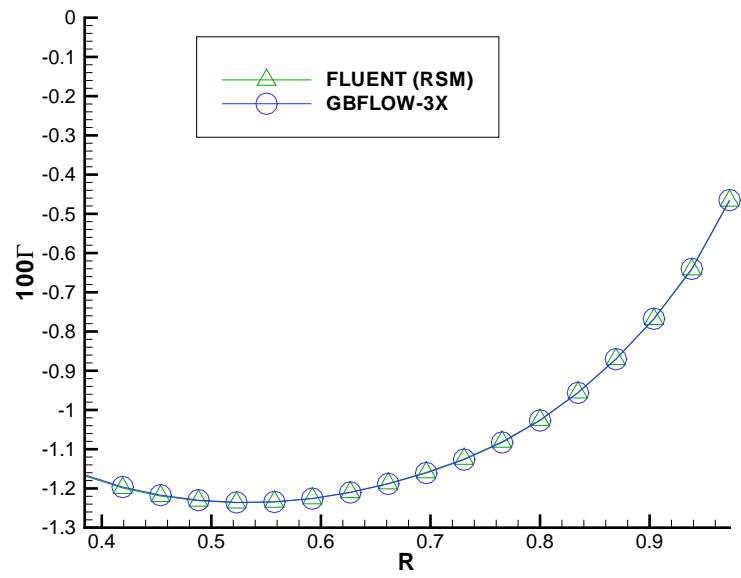


Figure 5.50: Comparison of circulation distributions for fore propeller predicted from GBFLOW-3X and FLUENT (viscous) coupled with MPUF-3A, for a twin type unit,  $J_s = 0.5$ ,  $Re = 6.26 \times 10^5$ .

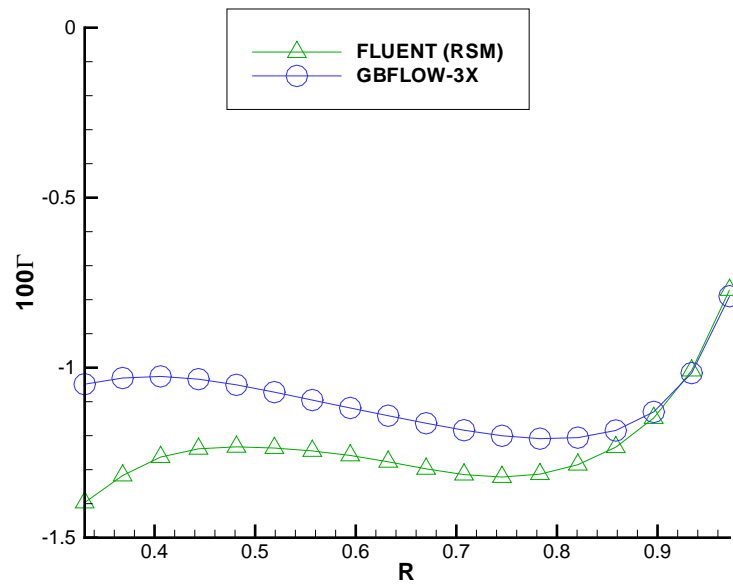


Figure 5.51: Comparison of circulation distributions for aft propeller predicted from GBFLOW-3X and FLUENT (viscous) coupled with MPUF-3A, for a twin type unit,  $J_s = 0.5$ ,  $Re = 6.26 \times 10^5$ .

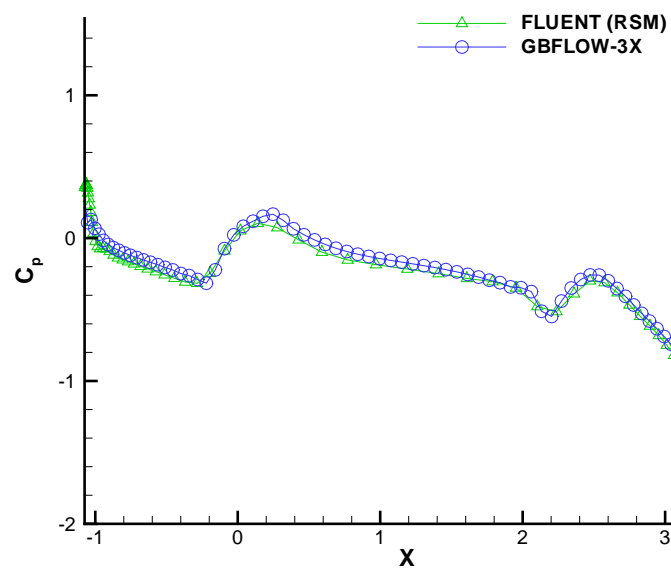


Figure 5.52: Comparison of pressure distributions along the body for a twin propeller from FLUENT(viscous) and GBFLOW-3X coupled with MPUF-3A.

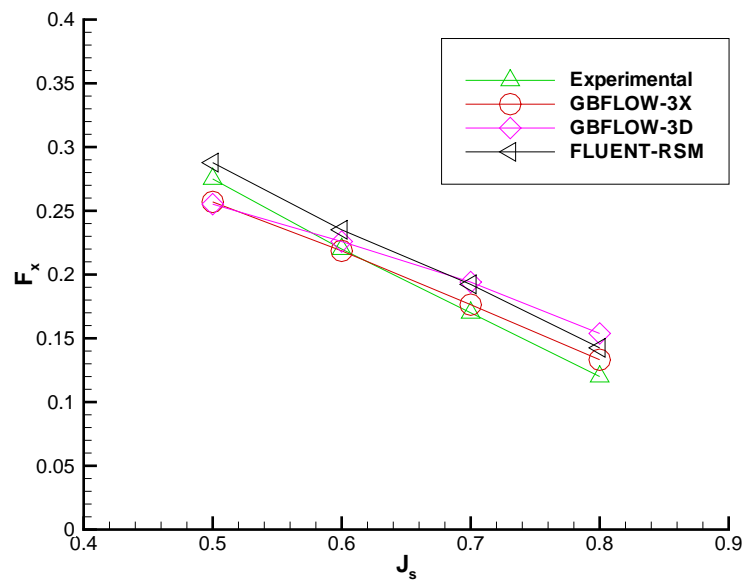


Figure 5.53: Comparison of axial force for a twin type propeller unit from GBFLOW-3X and viscous FLUENT coupled with MPUF-3A.

## **Chapter 6**

### **Pod with strut**

In this chapter, GBFLOW-3D, the fully 3-dimensional Euler solver is applied to a pod with the strut and the results are compared with those from other methods namely, the 3-D version of FLUENT and the three dimensional BEM. The existence of the strut over the pod makes the problem fully 3-dimensional and non-symmetric in nature. Convergence studies are carried out for all methods.

#### **6.1 3-D Euler Solver (GBFLOW-3D)**

In Chapter 4 an axi-symmetric pod was solved. But a real situation involves the presence of a strut and a hull over the strut, which acts as a wall. The Euler solver has to be capable of handling the interactions among the pod, the strut and the hull. The wall boundary conditions are applied on the pod, strut and hull so that the flow does not penetrate the body. A Finite Volume Method based Euler solver is applied to solve the problem. [Kakar 2002]

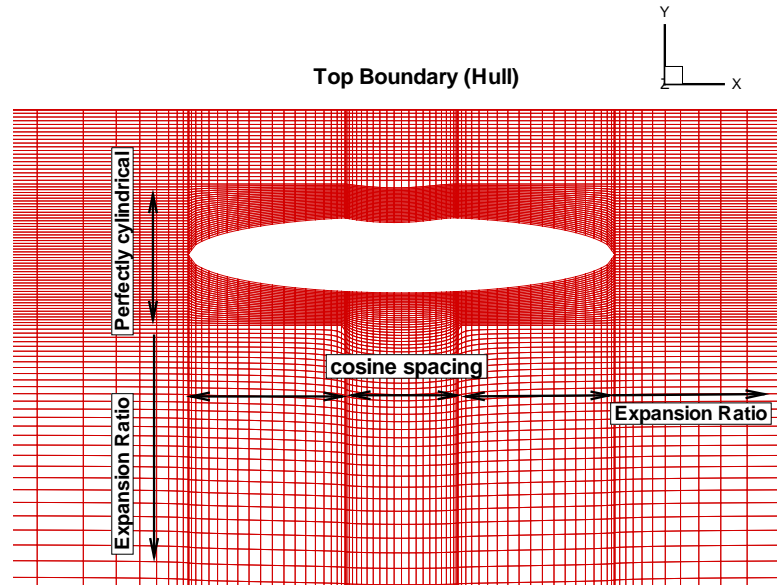


Figure 6.1: Cross-sectional view of the domain in axial direction showing the type of grid cells distribution at different locations (taken from [Gupta 2004]).

### 6.1.1 Grid Generation

The grid for the 3-D Euler solver is generated based on the 2-D ( $xy$  plane) pod geometry, the location of the strut on the pod, and the maximum thickness of the strut. In this study the strut has zero camber and a parabolic thickness distribution. Full cosine spacing is used along the chord of the strut to concentrate more cells at the leading and trailing edge and to capture the stagnation points. The pod section upstream of the leading edge and downstream of the trailing edge of the strut uses a full cosine spacing as well. The cell size in front of the leading edge of the pod is adjusted with an expansion ratio to avoid an abrupt change in the cell size. A similar grid is constructed downstream of the trailing edge of the pod. Figure 6.1 shows the grid along a vertical plane through the pod axis.

In order to capture the flow field near the strut and the hull properly, the grid near

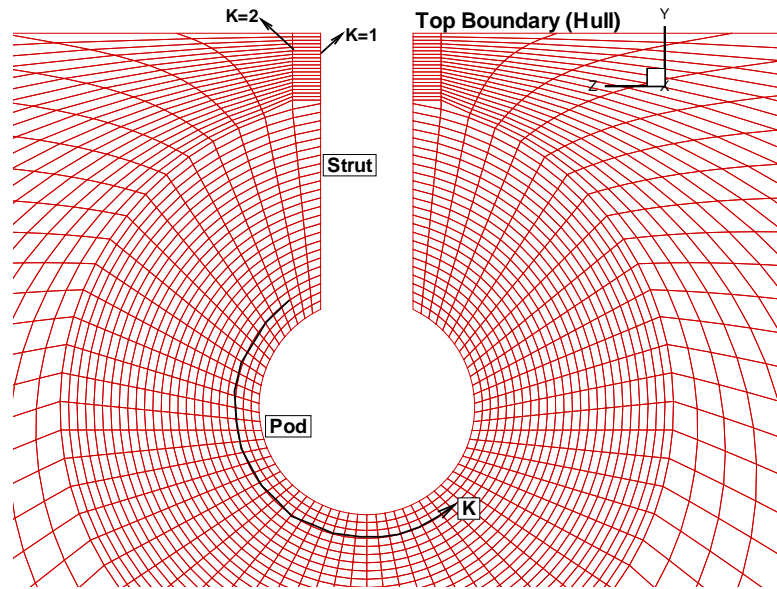


Figure 6.2: Cross-sectional view of the domain showing the grid cells near the strut and the pod. Circumferential cells are uniformly distributed.

the strut has to be fairly dense, and the aspect ratio of the grid cells should be close to one. Figure 6.2 shows the view of the strut in a plane along a station. To make a uniform grid at the far stream boundary, with dense grid near the strut, a large number of circumferential cells are required. One-fourth of the total circumferential cells are placed on the hull, with three-fourths on the circular far stream domain. If less cells are used, the grid points near the strut move away from the body, which leads to inaccurate results. Large number of cells lead to increase in the run time. Therefore, a grid like that shown in Figure 6.2 is chosen. The hull and far stream is given the index  $j = Nj$ . An alternate grid arrangement is also used in which the circumferential cells, index  $k$ , are clustered near the strut. Figure 6.3 shows this cell arrangement.

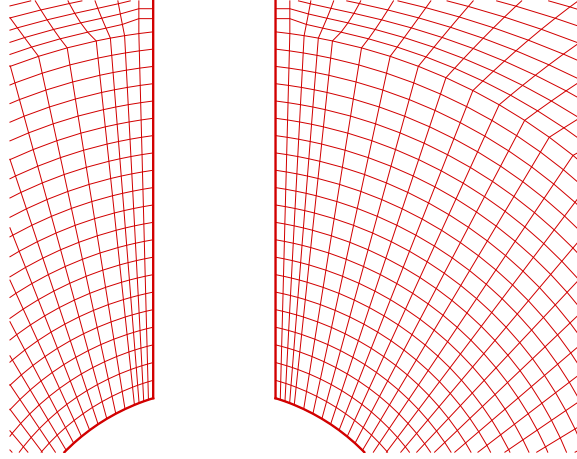


Figure 6.3: Cross-sectional view of the domain showing the grid cells near the strut and the pod. Circumferential cells are clustered near the strut.

### 6.1.2 Boundary Conditions

The boundary conditions are applied as detailed in Section 3.2.3. The *wall* boundary conditions are applied on the surface of the pod, strut and the hull. Free stream boundary condition is applied at  $j = Nj$ , where the circumferential index  $k$  is greater than  $(Nk - 1)/8$  and less than  $7(Nk - 1)/8$ . In the region  $j = Nj$ ,  $k$  less than  $(Nk - 1)/8$ , and  $k$  greater than  $7(Nk - 1)/8$  hull boundary condition is applied.

### 6.1.3 Results

Convergence studies are carried out for GBFLOW-3D. The flow field around the body and the pressure force on the body is obtained. First, runs are carried out with the grid having uniform circumferential cell distribution, but varying number of cells in the axial direction. Velocity and pressure comparisons are carried out at a location

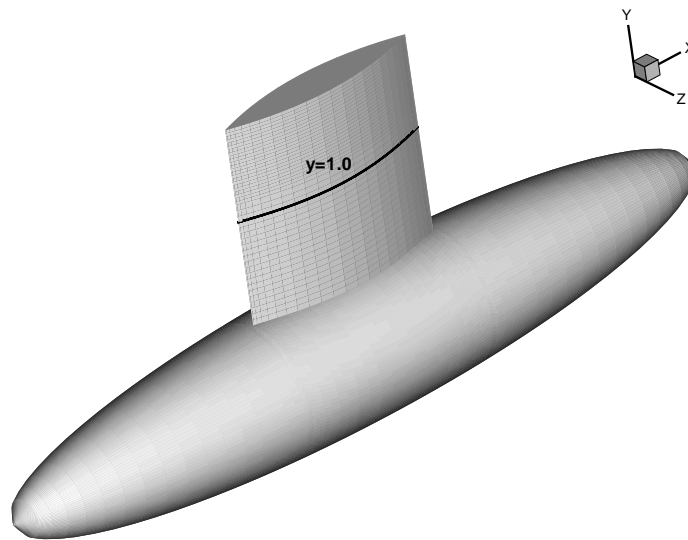


Figure 6.4: Location on strut where velocity and pressure comparisons are carried out.

on the strut where it intersects the plane  $y=1.0$ . The location is shown in Figure 6.4. Initially convergence studies are carried out by varying the number of nodes in the axial direction. Runs were carried out for 101, 121 and 141 nodes in the axial direction over the whole domain. The axial velocity and pressure were compared at the location  $y = 1.0$ . Figures 6.5 and 6.6 show the convergence with varying grid size in the axial direction. Next, comparisons are carried out between the two different types of grids used in the  $k$  direction, i.e. one uniformly distributed and the other with cells clustered near the strut. The number of nodes in the circumferential direction is fixed to  $k = 121$ . Figures 6.7 and 6.8 show the comparison of axial velocity and pressure, respectively, from the two grids. It will be seen (when comparisons are carried out with FLUENT) that the results from the grid with cells clustered near the strut are more accurate. It is also important to validate the solution obtained from the new grid by carrying out convergence studies. Runs are carried out by varying

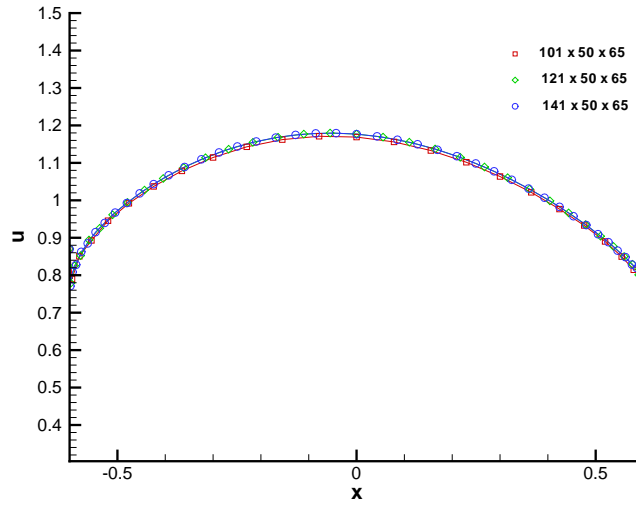


Figure 6.5: Convergence of axial velocity with varying number of nodes in axial direction in GBFLOW-3D.

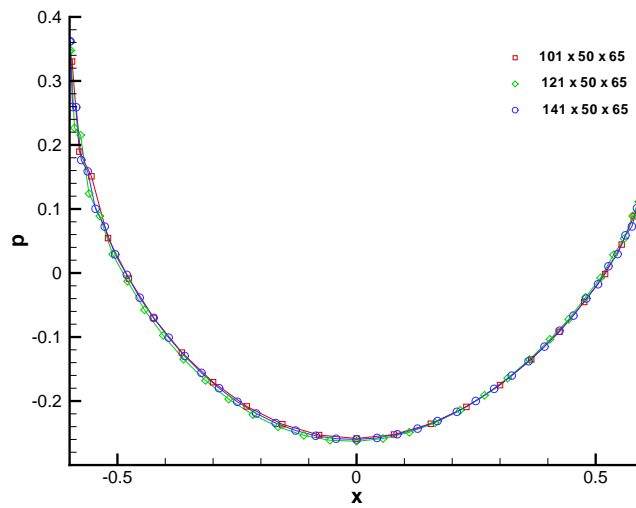


Figure 6.6: Convergence of pressure with varying number of nodes in axial direction in GBFLOW-3D.

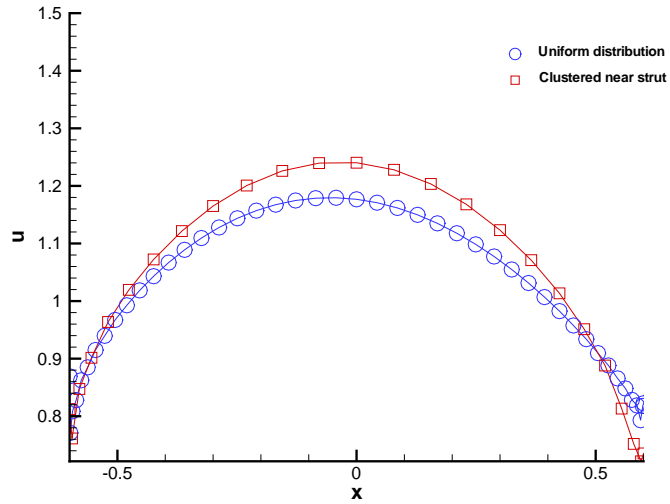


Figure 6.7: Comparison of axial velocity between the two different types of grids used in  $k$  direction in GBFLOW-3D,  $k = 121$

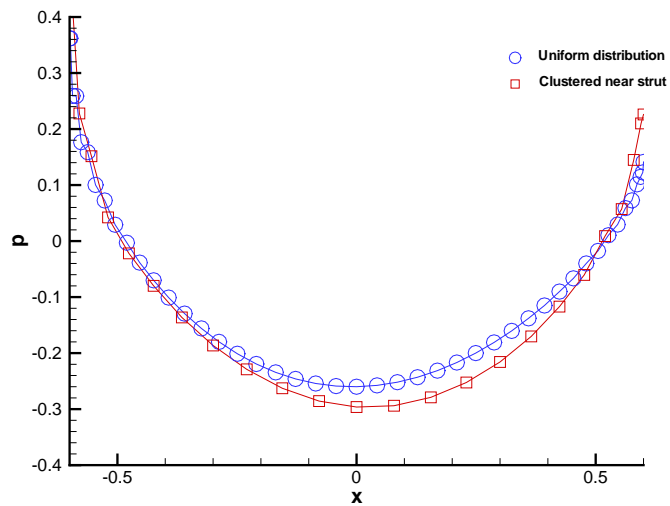


Figure 6.8: Comparison of pressure between the two different types of grids used in  $k$  direction in GBFLOW-3D,  $k = 121$

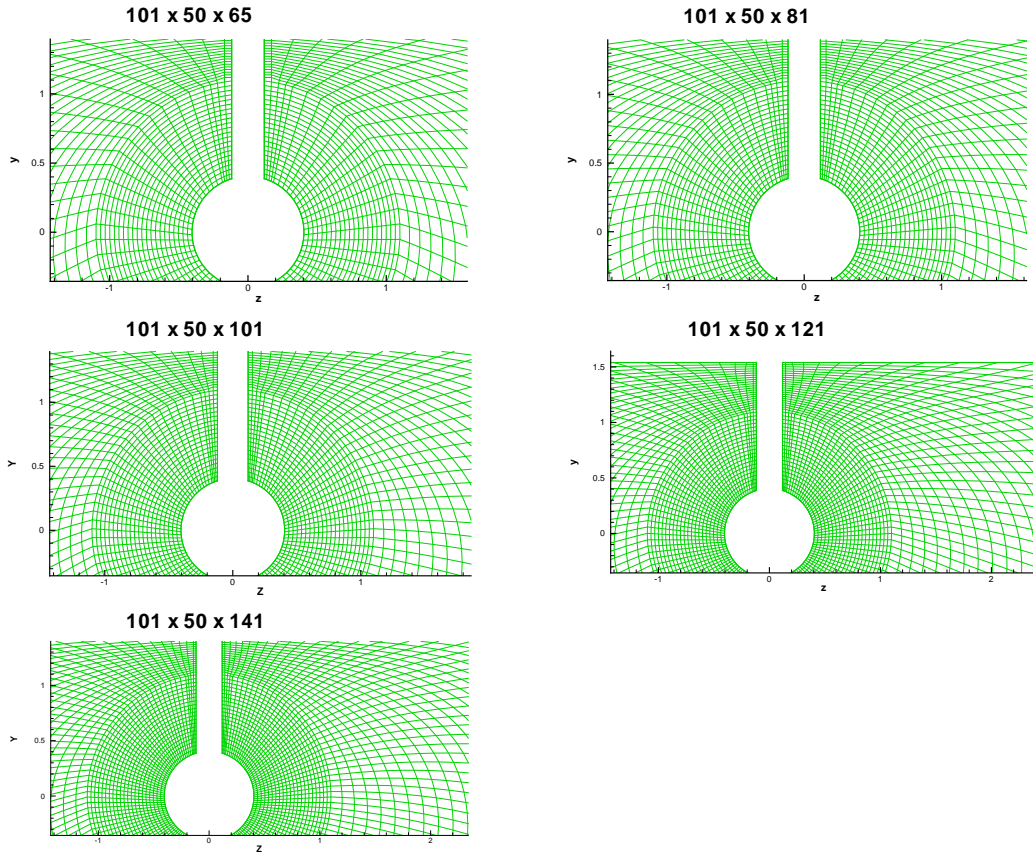


Figure 6.9: Different grids for which convergence with varying number of nodes along the circumferential direction in GBFLOW-3D

the number of nodes in the circumferential direction for the new grid. The different grids are shown in Figure 6.9. Figures 6.10 and 6.11 show the convergence of axial velocity and pressure with varying grid size in circumferential direction.

## 6.2 FLUENT-3D

The 3-dimensional inviscid version of FLUENT was used to solve for the pod with strut case, and to carry out comparisons with GBFLOW-3D. In this section the details of the grid and the boundary conditions are provided. Convergence studies were

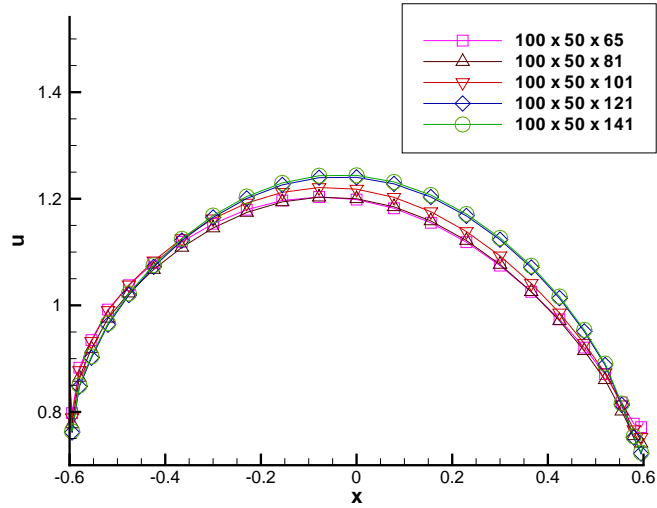


Figure 6.10: Convergence of axial velocity with varying number of nodes along the circumferential direction in GBFLOW-3D

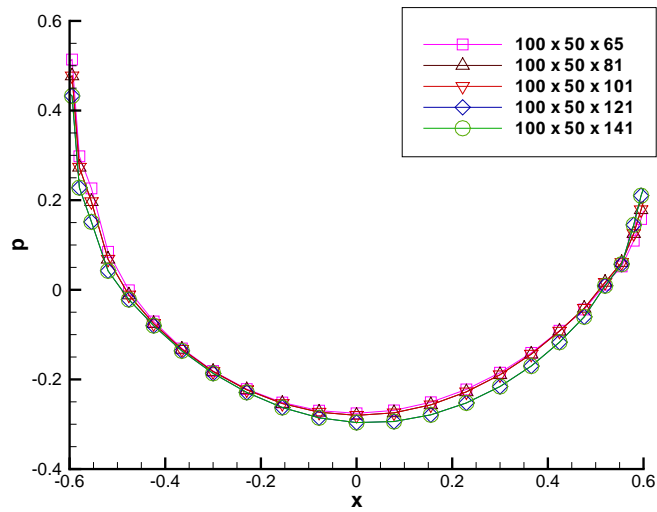


Figure 6.11: Convergence of pressure with varying number of nodes along the circumferential direction in GBFLOW-3D

also carried out for different grids.

### 6.2.1 Grid and boundary conditions

An unstructured grid was used in this case. The pod and strut were included inside a rectangular domain. The domain is shown in Figures 6.12 and 6.13. As can be seen the domain size is,  $-8 < x < 8$ ,  $-8 < y < 1.54$ ,  $-8 < z < 8$ . To generate the grid, the strut, the pod and the outside domain faces were meshed individually and then the volume was meshed as a whole. The domain faces were meshed using the *mapped* scheme in GAMBIT. The strut was also meshed using the *mapped* scheme. The pod, however, was meshed using the *sub-map* scheme. The reason for this is that the pod surface cannot be represented by four edges, which is a requirement for the mapped scheme. Having mapped the surfaces, the domain volume was meshed using *tetrahedral* elements and unstructured grid. Figure 6.14 shows the close up of the grid near the pod and strut in a plane that cuts through the center of the domain and is in the  $x$ - $y$  plane (i.e.  $z = 0$ ). Figure 6.15 shows the close up of the grid near the pod and strut in a plane that cuts through the center of the domain and is in the  $y$ - $z$  plane (i.e.  $x = 0$ ).

Boundary conditions are specified on the six faces of the rectangular domain and on the pod and strut. The wall boundary condition is applied on the pod and the strut. The top face of the domain serves as the hull and hence a wall condition is also specified on it. The two side faces, the bottom face and the face through which the flow comes in are specified as inflow boundaries, while the face through which the flow exits is specified as outflow boundary. The velocities specified at the inflow faces were  $u = 1.0m/s$ ,  $v = 0$ ,  $w = 0$ .

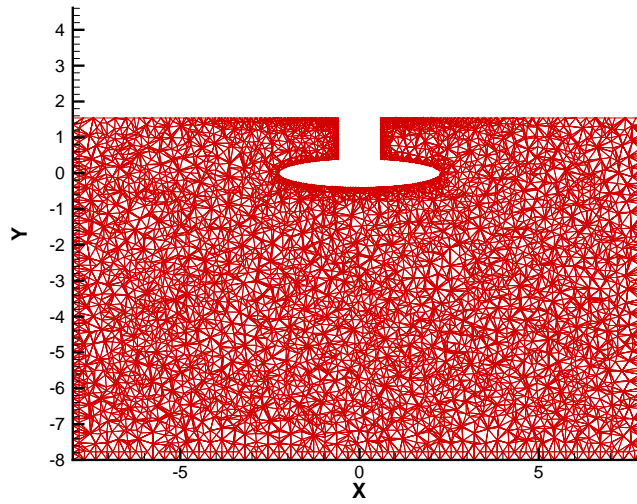


Figure 6.12: The domain used in 3D FLUENT, showing the projection in  $x$ - $y$  plane.

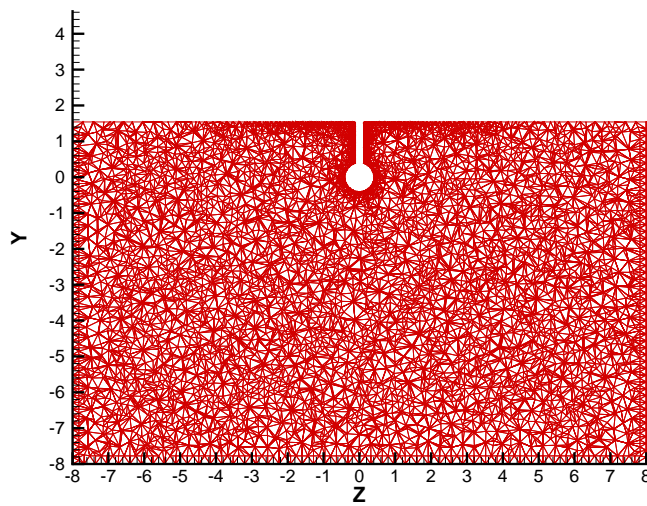


Figure 6.13: The domain used in 3D FLUENT, showing the projection in  $y$ - $z$  plane.

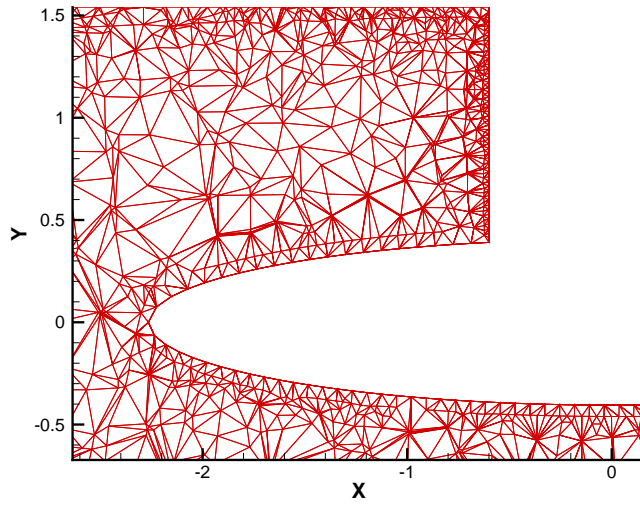


Figure 6.14: Close up of the grid used in 3D FLUENT near the pod and strut in the  $x$ - $y$  plane.

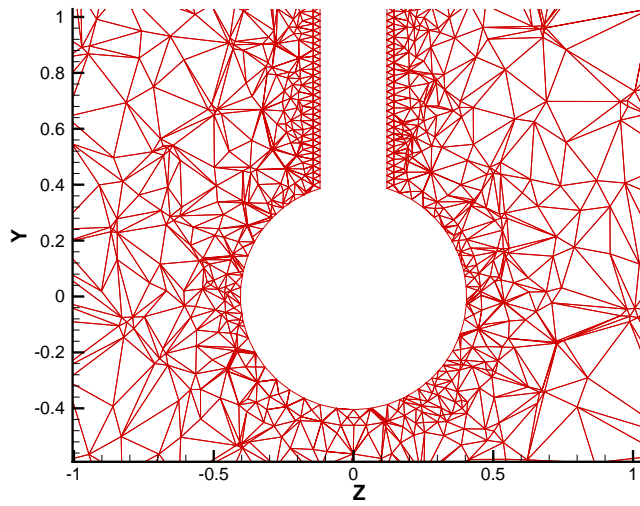


Figure 6.15: Close up of the grid used in 3D FLUENT near the pod and strut in the  $y$ - $z$  plane.

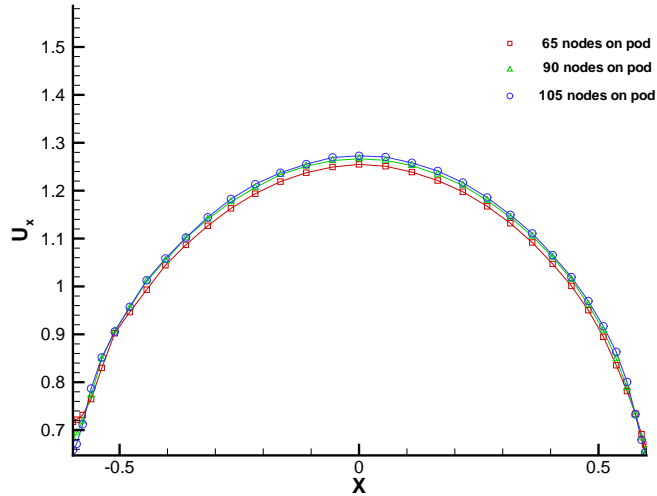


Figure 6.16: Convergence of axial velocity with varying number of nodes on the pod using FLUENT-3D (inviscid).

## 6.2.2 Inviscid Results

Convergence studies were carried out by varying the number of nodes on the pod. Since the grid is unstructured, by increasing the number of nodes on the pod, the cells near the pod and strut get finer. Comparison of pressures and velocities is carried out at the same location as shown in Figure 6.4. Figures 6.16 and 6.17 show the convergence of axial velocity and pressure with different grid sizes, respectively.

## 6.2.3 Viscous Results

Viscous runs were carried out using the same unstructured grids detailed above. The run parameters for the viscous runs are shown in Table 6.1. Since the grids are unstructured and no boundary layer is present on the wall, the  $y^+$  is very high.

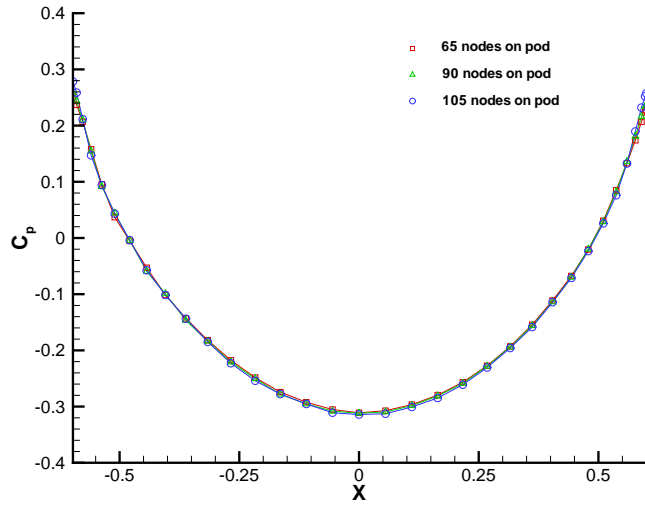


Figure 6.17: Convergence of pressure with varying number of nodes on the pod using FLUENT-3D (inviscid).

Solver	3DDP
Model	$k - \epsilon$
Density	998.2
Viscosity	$1 \times 10^{-3}$
$C_\mu$	0.09
Reynolds Number	$4.52 \times 10^6$
Inflow velocity	1.0
$k$	0.0009227
$\epsilon$	$2.193 \times 10^{-5}$

Table 6.1: Run parameters for 3-D viscous FLUENT

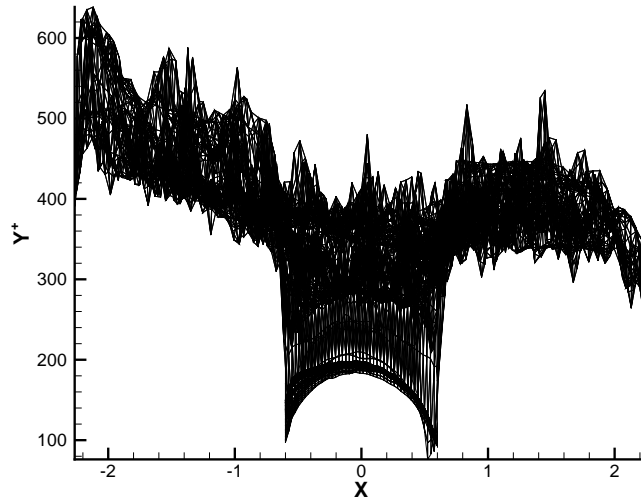


Figure 6.18:  $y^+$  distribution over the 3D pod and strut.

Figure 6.18 shows the  $y^+$  distribution along the pod and the strut. As can be seen the  $y^+$  is almost 700, with the higher values taking place over the surface of the pod. Hence, the solution might not be trustworthy. To judge the accuracy of the solution a test with the axisymmetric case was carried out. As shown in Figure 4.22 the  $y^+$  for the axisymmetric viscous case was about 40. The grid for the axisymmetric case was modified and made coarser such that the resultant  $y^+$  was around 700. The solution, namely, the pressure distribution along the body and the wall shear stress from both cases were compared to each other. It was observed that the distribution was not very different and hence it was deduced that the solution with a  $y^+$  of 700 is acceptable. The convergence of the velocities and pressures is shown in Figures 6.20 and 6.21. The velocities and pressures are compared at a location just after the strut,  $x = 1.01$  and in  $z = 0$  plane. The location is shown in Figure 6.19. The different grids used are unstructured and hence the number of nodes specified refer to the number of nodes on the pod edge before it is meshed.

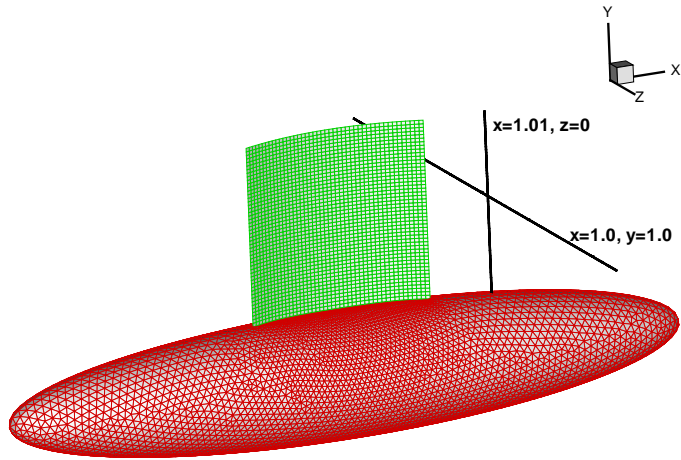


Figure 6.19: Locations behind the strut where the velocity and pressure comparisons are carried out for viscous 3D FLUENT.

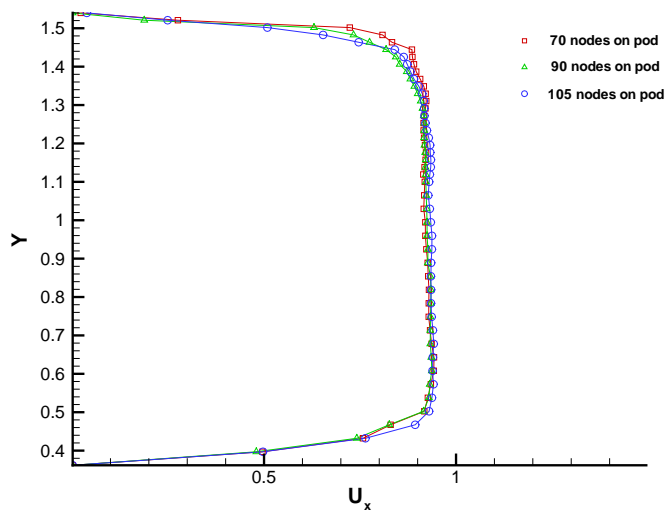


Figure 6.20: Convergence of axial velocity with varying number of nodes on the pod using FLUENT-3D (viscous),  $Re = 4.52 \times 10^6$ .

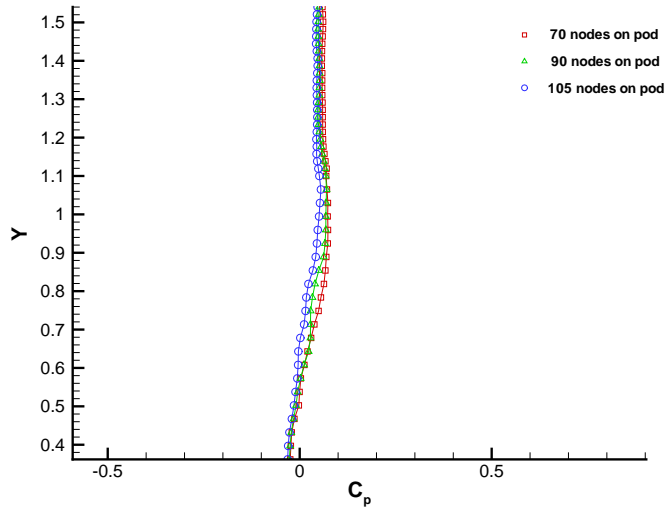


Figure 6.21: Convergence of pressure with varying number of nodes on the pod using FLUENT-3D (viscous),  $Re = 4.52 \times 10^6$ .

### 6.3 Comparison among different methods

A comparison of velocities and pressures predicted by GBFLOW-3D, inviscid FLUENT-3D and BEM is carried out. The details of the boundary element method as well as convergence studies are detailed in [Gupta 2004]. In this section the results of Gupta are used in the comparison. The GBFLOW-3D solution used is from the grid with cells clustered near the strut and  $k = 121$ . Figures 6.22 and 6.23 show the comparison of the axial velocity and the pressure at the location as shown in Figure 6.4. As it can be seen, the results from FLUENT and BEM agree very well with each other and that the axial velocity obtained from GBFLOW-3D is somewhat larger at the leading edge and smaller at the mid part of the strut. However, the pressures predicted from the three methods seem to be in closer agreement with each other.

Comparisons are also carried out between inviscid and viscous FLUENT at the locations shown in Figure 6.19. Figures 6.24 and 6.25 show the comparison for the

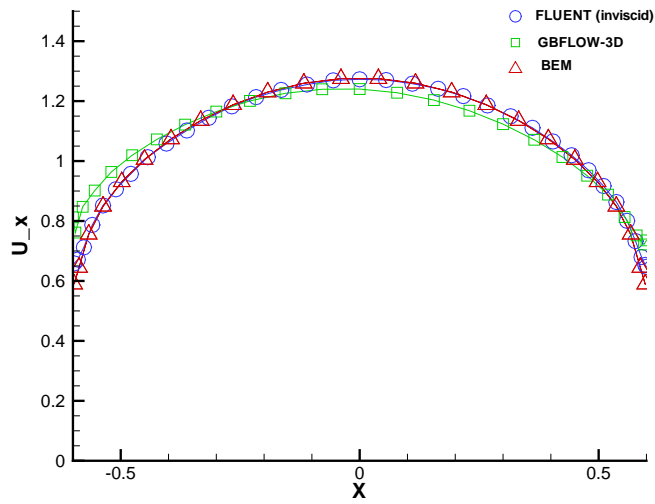


Figure 6.22: Comparison of axial velocity on the pod among the different methods.

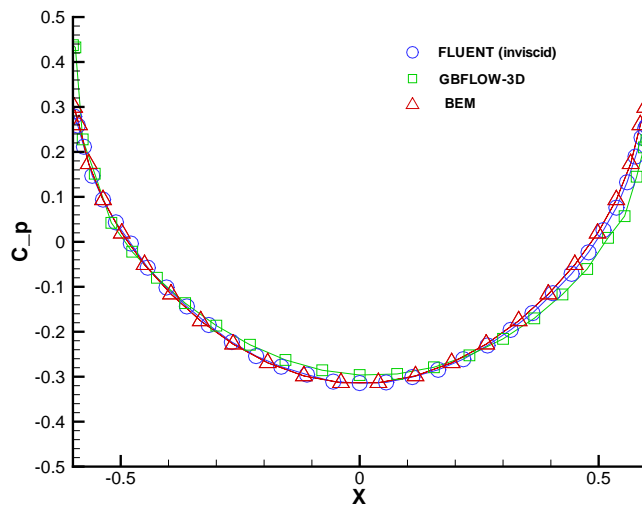


Figure 6.23: Comparison of pressure on the pod among the different methods.

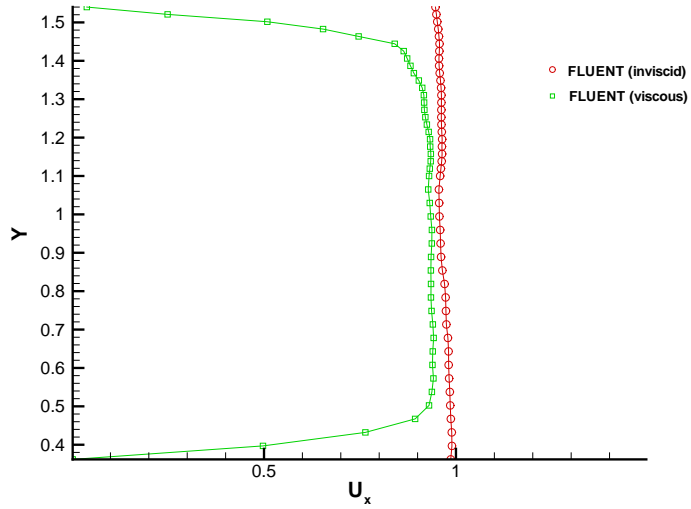


Figure 6.24: Comparison of axial velocity among inviscid and viscous 3D FLUENT at the line on the  $x$ - $z$  plane,  $Re = 4.52 \times 10^6$ .

line on the  $x$ - $z$  plane and Figures 6.26 and 6.27 shows the comparison at the line on the  $x$ - $y$  plane. It can be seen that the velocity in the case of the viscous flow is lower, since the presence of the strut (wall) causes shear and decreases the velocity.

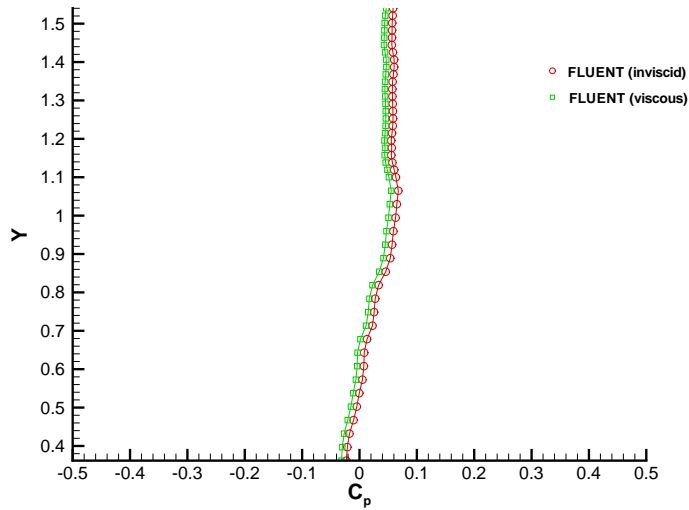


Figure 6.25: Comparison of pressure among inviscid and viscous 3D FLUENT at the line on the  $x$ - $z$  plane,  $Re = 4.52 \times 10^6$ .

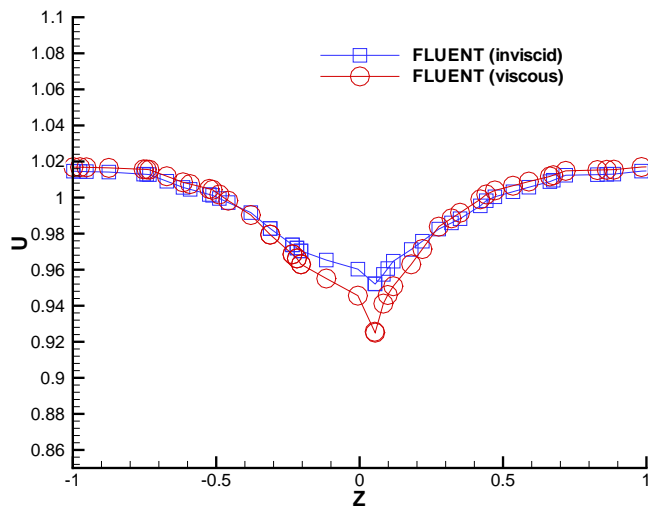


Figure 6.26: Comparison of axial velocity among inviscid and viscous 3D FLUENT at the line on the  $x$ - $y$  plane,  $Re = 4.52 \times 10^6$ .

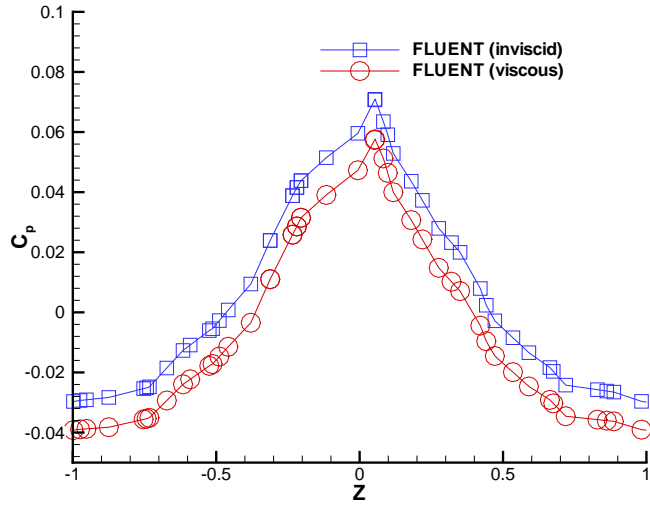


Figure 6.27: Comparison of pressure among inviscid and viscous 3D FLUENT at the line on the  $x$ - $y$  plane,  $Re = 4.52 \times 10^6$ .

## Chapter 7

### Conclusions and Recommendations

#### 7.1 Conclusions

As mentioned in earlier chapters, podded propulsion systems are now being widely used on commercial or naval vessels. Hence, the prediction of the performance of such systems is of utmost importance. [Kakar 2002] outlines some preliminary work carried out towards the numerical prediction of performance of podded propellers. This work was furthered in [Gupta 2004], where a 3-dimensional Euler solver was used to predict the flow around podded propulsors. The Euler solver was also extended to solve for yaw angles of attack. In this thesis, the Vortex Lattice Method has been coupled with an axi-symmetric Euler solver and an axi-symmetric viscous flow solver, to predict the performance of podded propellers and also estimate the effects of viscosity on the predictions.

The axi-symmetric Euler solver was validated by carrying out comparisons with a BEM solver and inviscid FLUENT. Viscous runs were also carried out using the viscous flow solver in FLUENT and the frictional force on the body was estimated. This was compared to the force obtained from the empirical ITTC formula which is used by the inviscid solver (GBFLOW) to account for the frictional force. It was found that the ITTC formula provided a reasonable approximation for the frictional

force acting on the pod.

The pod with a propeller case was solved via coupling between MPUF3A and GBFLOW or FLUENT. Both inviscid and viscous flow solvers were used in FLUENT. It was seen that viscosity did not affect the performance of the pull type podded unit significantly but the performance of the push type and the twin type (especially the aft propeller) podded unit changed significantly. Nevertheless, in the case of a twin propeller pod, the total force acting on the pod was not found to be influenced appreciably by the effects of viscosity. The  $k - \epsilon$  viscous model in FLUENT was found to be over dissipative and hence the RSM model was used. The 3-dimensional problem (pod with strut) was also solved without the propeller and comparisons were carried out with FLUENT and BEM. An alternate grid arrangement was used in GBFLOW-3D which seemed to provide more accurate results.

As detailed in Chapter 3, coupling between the VLM and the BEM was carried out. However, the method is not in complete working condition yet. More details regarding the method and tests carried out are included in the term report submitted for the class, “Hydrodynamics of Propulsors and Dynamic Positioning System”.

## **7.2 Recommendations**

This thesis is a first step in predicting the effects of viscosity via coupling of MPUF3A with FLUENT. Some recommendations for improvement and furthering this work are listed below:

- The coupling between 3D FLUENT and MPUF3A should be completed to solve the pod, strut and propeller problem iteratively. The solution to the

problem using the 3D body forces in FLUENT (via source terms) requires prohibitively large run times and efforts should be made to reduce it. This happens because the source terms are incorporated in FLUENT via UDF, and they have to be evaluated at every iteration. A change in the FLUENT source code maybe required to overcome this problem. Once this is done, the effects of viscosity can be estimated in the 3-dimensional case.

- A better grid for GBFLOW-3D should be developed to provide more accurate flow field results, especially near the strut region.
- The coupling between BEM and MPUF3A should be completed in order to assess the accuracy of the image model used in MPUF-3A when coupled with GBFLOW. Although individual modules of the coupling seem to work well, the overall solution does not. The reason for this has to be investigated.
- More validation with measurements are needed, especially in the case of push type podded propellers. In particular the flow field just upstream of the propeller should be measured and compared with our predictions.

## **Appendix A**

### Pod geometry used for 3-X and 3-D runs

X	R		X	R
-2.265	0.0E+0		-0.0853889	0.40468
-2.0800001	0.16028973		0.2492491	0.4024901
-1.8950001	0.22174709		0.39291653	0.39880943
-1.71	0.26552885		0.50475215	0.3947888
-1.5250001	0.29938104		0.5756959	0.391669
-1.34	0.32648843		0.6	0.3904801
-1.155	0.34837907		0.785	0.37985682
-0.97	0.36596354		0.97	0.36596357
-0.78499996	0.37985682		1.1550001	0.34837904
-0.6	0.3904801		1.3400002	0.3264884
-0.57569575	0.39166897		1.5250001	0.29938104
-0.50475215	0.39478877		1.7100002	0.26552876
-0.39291644	0.39880946		1.8950001	0.22174709
-0.24924898	0.40249016		2.0800001	0.16029005
2.265	0.0E+0			

Table 1: The pod geometry used by [Szantyr 2001a]

### Geometry of the strut used in GBFLOW-3D

X	Y	Z
-0.6	1.54	0.0E+0
-0.5795556	1.54	-0.0080384
-0.51961523	1.54	-0.03
-0.36525687	1.54	-0.07552915
-0.22961012	1.54	-0.1024264
-0.078315734	1.54	-0.11795556
0.078315734	1.54	-0.11795556
0.22961012	1.54	-0.1024264
0.36525687	1.54	-0.07552915
0.51961523	1.54	-0.03
0.5795556	1.54	-0.0080384
0.6	1.54	0.0E+0

Table 2: The parabolic section strut used for GBFLOW-3D runs with leading edge at the location  $X=-0.6$  on the pod, and trailing edge at  $X=+0.6$

### Geometry of the strut used by [Szantyr 2001a]

X	Y	Z
-0.6	1.54	0.0E+0
-0.5756959	1.54	-0.068673864
-0.50475215	1.54	-0.13486163
-0.39291653	1.54	-0.19476245
-0.2492491	1.54	-0.23895688
-0.08538896	1.54	-0.2590484
0.0853889	1.54	-0.2476123
0.24924898	1.54	-0.20349935
0.39291644	1.54	-0.13812754
0.50475215	1.54	-0.070037215
0.57569575	1.54	-0.018887708
0.6	1.54	0.0E+0

Table 3: The strut used by [Szantyr 2001a] for the experimental measurements. It is a NACA066 section, and has the leading edge at the location  $X=-0.6$  on the pod, and trailing edge at  $X=+0.6$

### Front Propeller Geometry used in [Szantyr 2001a]

r/R	P/D	Rk/D	Skew	C/D	F/C	T/D
0.3027	0.8	0.00	0.00	0.3252	0.0621	0.0404
0.3463	0.8	0.00	0.00	0.3794	0.0506	0.0384
0.4552	0.8	0.00	0.00	0.5148	0.0314	0.0323
0.5642	0.8	0.00	0.00	0.6291	0.0207	0.0261
0.6731	0.8	0.00	0.00	0.7179	0.0139	0.0200
0.7821	0.8	0.00	0.00	0.7616	0.0090	0.0138
0.8910	0.8	0.00	0.00	0.7165	0.0053	0.0076
0.9455	0.8	0.00	0.00	0.5938	0.0038	0.0045
1.000	0.8	0.00	0.00	0.2000	0.0000	0.0000

Table 4: Front propeller geometry. The front propeller placed at the location -1.1899 on the pod

**Station No. and % c**

1	1.0
2	2.5
3	5.0
4	10.0
5	20.0
6	30.0
7	40.0
8	50.0
9	60.0
10	70.0
11	80.0
12	90.0
13	95.0
14	97.5
15	99.0
16	100.0

Table 5: The specific stations along the chord where the propeller blade thickness and camber distributions are specified, at the given radii locations.

### Camber Distribution, f/C

Radii	0.3027	0.3463	0.4552	0.5642	0.6731	0.7821	0.8910	0.9455	1.000
station1	0.0041	0.0029	0.0014	0.0009	0.0006	0.0005	0.0003	0.0003	0.0000
station2	0.0099	0.0071	0.0034	0.0023	0.0016	0.0011	0.0007	0.0007	0.0000
station3	0.0183	0.0132	0.0065	0.0044	0.0030	0.0021	0.0014	0.0012	0.0000
station4	0.0314	0.0232	0.0120	0.0080	0.0055	0.0037	0.0024	0.0020	0.0000
station5	0.0466	0.0362	0.0206	0.0137	0.0093	0.0061	0.0038	0.0029	0.0000
station6	0.0547	0.0439	0.0265	0.0176	0.0118	0.0077	0.0046	0.0034	0.0000
station7	0.0605	0.0491	0.0301	0.0199	0.0134	0.0087	0.0051	0.0037	0.0000
station8	0.0621	0.0506	0.0314	0.0207	0.0139	0.0090	0.0053	0.0038	0.0000
station9	0.0605	0.0491	0.0301	0.0199	0.0134	0.0087	0.0051	0.0037	0.0000
station10	0.0547	0.0439	0.0265	0.0176	0.0118	0.0077	0.0046	0.0034	0.0000
station11	0.0466	0.0362	0.0206	0.0137	0.0093	0.0061	0.0038	0.0029	0.0000
station12	0.0313	0.0232	0.0120	0.0080	0.0055	0.0037	0.0024	0.0020	0.0000
station13	0.0180	0.0131	0.0065	0.0044	0.0030	0.0021	0.0014	0.0012	0.0000
station14	0.0096	0.0069	0.0033	0.0023	0.0016	0.0011	0.0007	0.0006	0.0000
station15	0.0040	0.0028	0.0014	0.0009	0.0006	0.0005	0.0003	0.0003	0.0000

Table 6: The camber distribution specified at the nine radii locations specified in the geometry file and at specific stations along the chord.

### Thickness Distribution, t/C

Radii	0.3027	0.3463	0.4552	0.5642	0.6731	0.7821	0.8910	0.9455	1.000
station1	0.0086	0.0060	0.0027	0.0019	0.0013	0.0009	0.0006	0.0005	0.0000
station2	0.0205	0.0144	0.0067	0.0045	0.0031	0.0022	0.0015	0.0013	0.0000
station3	0.0378	0.0269	0.0128	0.0087	0.0060	0.0042	0.0028	0.0024	0.0000
station4	0.0641	0.0470	0.0239	0.0160	0.0110	0.0075	0.0049	0.0040	0.0000
station5	0.0938	0.0727	0.0412	0.0274	0.0185	0.0123	0.0076	0.0058	0.0000
station6	0.1098	0.0880	0.0530	0.0352	0.0236	0.0154	0.0092	0.0067	0.0000
station7	0.1209	0.0981	0.0603	0.0399	0.0267	0.0174	0.0102	0.0074	0.0000
station8	0.1241	0.1013	0.0627	0.0415	0.0278	0.0181	0.0106	0.0076	0.0000
station9	0.1209	0.0981	0.0603	0.0399	0.0267	0.0174	0.0102	0.0074	0.0000
station10	0.1098	0.0880	0.0530	0.0352	0.0236	0.0154	0.0092	0.0067	0.0000
station11	0.0939	0.0727	0.0412	0.0274	0.0185	0.0123	0.0076	0.0058	0.0000
station12	0.0642	0.0471	0.0239	0.0160	0.0110	0.0075	0.0049	0.0040	0.0000
station13	0.0375	0.0268	0.0128	0.0087	0.0060	0.0042	0.0028	0.0024	0.0000
station14	0.0202	0.0143	0.0066	0.0045	0.0031	0.0022	0.0015	0.0013	0.0000
station15	0.0084	0.0059	0.0027	0.0018	0.0013	0.0009	0.0006	0.0005	0.0000
station16	0.0	0.0	0.0	0.0	0.0	0.0	0.0	0.0	0.0

Table 7: The thickness distribution specified at the nine radii locations specified in the geometry file and at specific stations along the chord.

## Aft Propeller Geometry

r/R	P/D	Rk/D	Skew	C/D	F/C	T/D
0.3027	1.108	0.00	0.00	0.3252	0.0621	0.0404
0.3463	1.108	0.00	0.00	0.3794	0.0506	0.0384
0.4552	1.108	0.00	0.00	0.5148	0.0314	0.0323
0.5642	1.108	0.00	0.00	0.6291	0.0207	0.0261
0.6731	1.108	0.00	0.00	0.7179	0.0139	0.0200
0.7821	1.108	0.00	0.00	0.7616	0.0090	0.0138
0.8910	1.108	0.00	0.00	0.7165	0.0053	0.0076
0.9455	1.108	0.00	0.00	0.5938	0.0038	0.0045
1.000	1.108	0.00	0.00	0.2000	0.0000	0.0000

Table 8: Geometry of the aft propeller. The aft propeller placed at the location 1.1899 on the pod. The thickness and camber distributions are the same as for the fore propeller.

## Bibliography

- Achkinadze, A., Berg, A., Krasilnikov, V. and Stepanov, I. [2003], ‘Numerical analysis of podded and steering systems using a velocity based source boundary element method with modified trailing edge’.
- Blenkey, N. [1997], ‘Getting twin propeller efficiency from a pod’, *Marine Log* .
- Breslin, J., Van Houten, R., Kerwin, J. and Johnsson, C.-A. [1982], ‘Theoretical and experimental propeller-induced hull pressures arising from intermittent blade cavitation, loading, and thickness’, *Trans. SNAME* **90**.
- Chicherin, I., A., Lobatchev, M., Pustoshny, A., V. and Sanchez-Caja, A. [2004], ‘On a propulsion prediction procedure for ships with podded propulsors using rans-code analysis’, *Proceedings of the First International Conference on Technological Advances in Podded Propulsion* pp. pp. 223–236.
- Choi, J.-K. [2000], Vortical Inflow – Propeller Interaction Using an Unsteady Three-Dimensional Euler Solver, PhD thesis, Department of Civil Engineering, The University of Texas at Austin.
- Choi, J.-K. and Kinnas, S. [1998], A 3-D Euler solver and its application on the analysis of cavitating propellers, in ‘Proceedings of the 25th ATTC’, American Towing Tank Conference, Iowa City, Iowa.

- Choi, J.-K. and Kinnas, S. [2000a], Non-axisymmetric effective wake prediction by using an unsteady three-dimensional Euler solver, *in* 'Propellers/Shafting '00 Symposium', Soc. Naval Arch. & Marine Engrs., Virginia Beach, VA.
- Choi, J.-K. and Kinnas, S. [2000b], An unsteady 3-D Euler solver coupled with a cavitating propeller analysis method, *in* '23rd Symposium on Naval Hydrodynamics', Val de Reuil, France.
- Choi, J.-K. and Kinnas, S. [2001], 'Prediction of Non-axisymmetric Effective Wake by a Three-Dimensional Euler Solver', *Journal of Ship Research* **45**(1), pp. 13–33.
- Choi, J.-K. and Kinnas, S. [2003], 'Prediction of unsteady effective wake by an euler solver/vortex-lattice coupled method', *Journal of Ship Research*, Vol. 47, pp.131-144 .
- Choi, J. and Kinnas, S. [2000c], An unsteady three-dimensional euler solver coupled with a cavitating propeller analysis method, *in* 'The 23rd Symposium on Naval Hydrodynamics', Val de Reuil, France.
- Chorin, A. J. [1967], 'A numerical method for solving incompressible viscous flow problems', *Journal of Computational Physics* **2**, pp.12–26.
- Dai, C., Gorski, J. and Haussling, H. [1991], Computation of an integrated ducted propulsor/stern performance in axisymmetric flow, *in* 'Propellers/Shafting '91 Symposium', Soc. Naval Arch. & Marine Engrs., Virginia Beach, VA.
- FLUENT [2003], Fluent 6.1 user's guide, User's manual, FLUENT.
- Gawn, R. and Burrill, L. [1957], 'Effect of cavitation on the performance of a series of 16 in. model propellers', *Transactions INA* **99**, pp. 690–728.

- Ghassemi, H. and Allievi, A. [1999], 'A Computational Method for the Analysis of Fluid Flow and Hydrodynamic Performance of Conventional and Podded Propulsion Systems', *Oceanic Engineering International* **3**(1), pp. 101–115.
- Greeley, D. and Kerwin, J. [1982], 'Numerical methods for propeller design and analysis in steady flow', *Trans. SNAME* **vol 90**.
- Griffin, P. [1998], Computational techniques for the design and analysis of cavitating propeller blades, Master's thesis, UT Austin, Dept. of Civil Engineering.
- Gu, H. and Kinnas, S. A. [2003], Modeling of contra-rotating and ducted propellers via coupling of a vortex-lattice with a finite volume method, *in* 'Propellers/Shafting 2003'.
- Gu, H., Natarajan, S., Gupta, A. and Kinnas, S. [2003], GBFLOW (version 1.1) user's manual, Ocean Engineering Report 03-3, Ocean Engineering Group, UT Austin, Austin, TX.
- Gupta, A. [2004], Numerical prediction of flows around podded propulsors, Master's thesis, Department of Civil Engineering, The University of Texas at Austin.
- Hsin, C.-Y., Chou, S.-K. and Chen, W.-C. [2002], A new propeller design method for the pod propulsion system, *in* 'Proceedings of Twenty-Fourth Symposium on Naval Hydrodynamics', Fukuoka, Japan.
- Huang, T. and Cox, B. [1977], Interaction of afterbody boundary layer and propeller, *in* 'Symposium on Hydrodynamics of Ship and Offshore Propulsion System', Høvik outside Oslo.

- Huang, T. and Groves, N. [1980], Effective wake : Theory and experiment, *in* '13th Symposium on Naval Hydrodynamics', Tokyo.
- Huang, T., Wang, H., Santelli, N. and Groves, N. [1976], Propeller/stern boundary layer interaction on axisymmetric bodies : Theory and experiment, Technical Report DTNSRDC 76-0113, DTNSRDC.
- Hughes, M. [1993], Analysis of Multi-component Ducted Propulsors in Unsteady Flow, PhD thesis, M.I.T., Department of Ocean Engineering.
- Hughes, M. and Kinnas, S. [1991], A analysis method for a ducted propeller with pre-swirl stator blades, *in* 'Propellers/Shafting '91 Symposium', Soc. Naval Arch. & Marine Engrs., Virginia Beach, VA, pp. 1–8 (paper No. 15).
- Hughes, M. and Kinnas, S. [1993], Unsteady flows around multi-component integrated propulsors, *in* 'Forum on Unsteady Flows, (FED-Vol. 157)', Fluids Engineering Division, ASME, pp. 21–31.
- HYDROCOMP, I. [1999], Modeling tractor-style azimuthing podded drives, Technical Report 127, HYDROCOMP Inc.
- Islam, M., Taylor, R., Quinton, J., Veitch, B. and Bose, N. [2004], 'Numerical investigation on hydrodynamic performance of podded propeller', *Proceedings of the First International Conference on Technological Advances in Podded Propulsion* pp. 513–526.
- Kakar, K. [2002], Computational Modeling of FPSO Hull Roll Motions and Two-component Marine Propulsion Systems, Master's thesis, Department of Civil Engineering, The University of Texas at Austin.

- Kerwin, J. E., Coney, W. B. and Hsin, C.-Y. [1988], Hydrodynamic aspects of propeller/stator design, *in* 'Proceedings of the Propellers '88 Symposium', number 3, SNAME, Virginia Beach, VA.
- Kerwin, J., Keenan, D., Black, S. and Diggs, J. [1994], 'A coupled viscous/potential flow design method for wake adapted multi-stage, ducted propulsors using generalized geometry', *Trans. SNAME* **102**.
- Kerwin, J., Kinnas, S., Lee, J. and Shih, W. Z. [1987], *in* 'A surface panel method for the hydrodynamic analysis of ducted propellers', Vol. 95.
- Kerwin, J., Kinnas, S., Wilson, M. and McHugh, J. [1986], Experimental and analytical techniques for the study of unsteady propeller sheet cavitation, *in* 'Proceedings of the Sixteenth Symposium on Naval Hydrodynamics', Berkeley, California, pp. 387–414.
- Kerwin, J. and Lee, C.-S. [1978], 'Prediction of steady and unsteady marine propeller performance by numerical lifting-surface theory', *Trans. SNAME* **vol 86**.
- Kerwin, J., Taylor, T., Black, S. and McHugh, G. [1997*a*], A coupled lifting-surface analysis technique for marine propulsors in steady flow, *in* 'Propellers/Shafting '97 Symposium', Soc. Naval Arch. & Marine Engrs., Virginia Beach, VA, pp. 1–15 (Paper No. 20).
- Kerwin, J., Taylor, T., Black, S. and McHugh, G. [1997*b*], 'A coupled lifting-surface analysis technique or marine propellers in steady flow', *Proceedings of the Propellers/Shafting Symposium* pp. pp. 20/1–15.
- Kinnas, S. [1991], 'Leading-edge corrections to the linear theory of partially cavitating hydrofoils', *Journal of Ship Research* **35**(1), pp. 15–27.

- Kinnas, S. [1992], 'A general theory for the coupling between thickness and loading for wings and propellers', *Journal of Ship Research* **36**(1), pp. 59–68.
- Kinnas, S., Choi, J., Lee, H. and Young, J. [2000], Numerical cavitation tunnel, in 'NCT50, International Conference on Propeller Cavitation', Newcastle upon Tyne, England.
- Kinnas, S., Choi, J., Lee, H., Young, Y., Gu, H., Kakar, K. and Natarajan, S. [2002], 'Prediction of cavitation performance of single/multi-component propulsors and their interaction with the hull', *Trans. SNAME* .
- Kinnas, S. and Fine, N. [1989], Theoretical prediction of the midchord and face unsteady propeller sheet cavitation, in 'Proceedings of the Fifth International Conference on Numerical Ship Hydrodynamics', Hiroshima, Japan.
- Kinnas, S., Griffin, P., Choi, J.-K. and Kosal, E. [1998a], 'Automated design of propulsor blades for high-speed ocean vehicle applications', *Trans. SNAME* **106**.
- Kinnas, S., Griffin, P., Choi, J.-K. and Kosal, E. [1998b], 'Automated design of propulsor blades for high-speed ocean vehicle applications', *Trans. SNAME* **106**.
- Kinnas, S., Gu, H., Gupta, A. and Lee, H. [2004], Numerical prediction of the performance of podded propulsors and ducted propellers, in 'Proceedings of the 13th Offshore Symposium on The Application of Emerging Technologies', Houston, Texas, pp. 19–34.
- Kinnas, S., Lee, H., Gu, H. and Gupta, A. [2004], Prediction of performance of ducted and podded propellers, in '25th Symposium on Naval Hydrodynamics', St. John's, Newfoundland and Labrador, Canada.

- Kinnas, S., Lee, H., Gu, H., Yu, Y., Sun, H., Vinayan, V., Kacham, B., Mishra, B. and Deng, Y. [2004], 'University/navy/industry consortium on cavitation performance of high speed propulsors - presentations and progress reports - 22nd steering committee meeting'.
- Kinnas, S. and Pyo, S. [1999], 'Cavitating propeller analysis including the effects of wake alignment', *Journal of Ship Research* **43**(1), pp. 38–47.
- Kosal, E. [1999], Improvements and enhancements in the numerical analysis and design of cavitating propeller blades, Master's thesis, UT Austin, Dept. of Civil Engineering.
- Kudo, T. and Kinnas, S. [1995], Application of vortex/source lattice method on supercavitating propellers, in '24th American Towing Tank Conference', College Station, TX.
- Lee, C.-S. [1979], Prediction of Steady and Unsteady Performance of Marine Propellers with or without Cavitation by Numerical Lifting Surface Theory, PhD thesis, M.I.T., Department of Ocean Engineering.
- Lewis, E. [1988], *Principles of Naval Architecture*, Society of Naval Architects and Marine Engineers.
- Maskew, B. [1990], USAERO, A Time-stepping Analysis Method for the Flow About Multiple Bodies in General Motions, User's Manual , Technical report, Analytical Methods, Inc., Redmond, WA.
- Morino, L. and Kuo, C.-C. [1974], 'Subsonic Potential Aerodynamic for Complex Configurations : A General Theory', *AIAA Journal* **vol 12**(no 2), pp 191–197.

- Natarajan, S. [2003], Computational Modeling of Marine Rudders and Multi-component Marine Propulsion Systems, Master's thesis, Department of Civil Engineering, The University of Texas at Austin.
- Ni, R.-H. [1982], 'A multiple-grid scheme for solving the Euler equations', *AIAA Journal* **20**(11), pp.1565–1571.
- Ohashi, K. and Hino, T. [2004], 'Numerical simulations of the flows around a ship with podded propulsor', *Proceedings of the First International Conference on Technological Advances in Podded Propulsion* pp. pp. 211–222.
- Ohkusu, M., ed. [1996], *Advances in Marine Hydrodynamics*, Computational Mechanics Publications, Southampton, UK.
- Sanchez-Caja, A., Rautaheimo, P. and Siikonen, T. [1999], Computation of the incompressible viscous flow around a tractor thruster using a sliding-mesh technique, in 'Proceedings of Seventh International Conference on Numerical Ship Hydrodynamics', France.
- Shih, W.-Z. [1988], A Combined Euler Equation/Surface Panel Solution to The Shear Interaction Problem of An Open or Ducted Propeller, PhD thesis, Department of Ocean Engineering, M.I.T.
- Stern, F., Kim, H., Patel, V. and Chen, H. [1988a], 'Computation of viscous flow around propeller-shaft configurations', *Journal of Ship Research* **32**(4), pp.263–284.
- Stern, F., Kim, H., Patel, V. and Chen, H. [1988b], 'A viscous-flow approach to the computation of propeller- hull interaction', *Journal of Ship Research* **32**(4), pp. 246–262.

- Stern, F., Kim, H., Zhang, D., Kerwin, J. and Jessup, S. [1994], 'Computation of viscous flow around propeller-body configurations: Series 60  $cb=0.6$  ship model', *Journal of Ship Research* **38**(2), pp. 137–157.
- Szantyr, J. [2001a], 'Hydrodynamic model experiments with pod propulsors', *Oceanic Engineering International* **5**(2), pp. 95–103.
- Szantyr, J. [2001b], 'Hydrodynamic model experiments with pod propulsors', *Ocean Engineering International* **5-2**, pp. 95–103.
- Tsakonas, S., Jacobs, W. and Liao, P. [1983], 'Prediction of steady and unsteady loads and hydrodynamic forces on counterrotating propellers', *Journal of Ship Research* **27**(3), pp. 197–214.
- Vartdal, L. and Bloch, F. [2001], Ferrycat 120 propulsion aspects and manoeuvring capabilities, in 'Proceedings of First International Conference on Double-ended Ferries', Molde, Norway.
- Vartdal, L., Gjerde, K. M., Bloch, F. and Sittanggang, P. [1999], Application of various cfd methods in the development of the azipull podded propulsion system, in 'The International CFD Conference in Ship Hydrodynamics', Ulsteinvik, Norway.
- Warren, C., Taylor, T. and Kerwin, J. [2000], A coupled viscous/potential-flow method for the prediction of propulsor-induced maneuvering forces, in 'Propellers/Shafting '00 Symposium', Soc. Naval Arch. & Marine Engrs., Virginia Beach, VA.

Yang, C.-J., Wang, G., Tamashima, M., Yamazaki, R. and Koizuka, H. [1992], 'Prediction of the unsteady performance of contra-rotating propellers by lifting surface theory', *Trans. of the West-Japan Society of Naval Architects* (No. 83), pp. 47–65.

## Vita

Bikash Mishra was born in Balasore, India on September 22, 1981. He is the son of Basanta Kumar Mishra and Pushpamitra Mishra. He obtained his Bachelor of Technology in Naval Architecture and Ocean Engineering from the Indian Institute of Technology at Madras in July, 2003. He started his Masters program in civil engineering at The University of Texas at Austin in September, 2003.

Permanent address: 2907 Rio Grande, Austin Texas

This thesis was typeset with  $\text{\LaTeX}^\ddagger$  by the author.

---

<sup>‡</sup> $\text{\LaTeX}$  is a document preparation system developed by Leslie Lamport as a special version of Donald Knuth's  $\text{\TeX}$  Program.